DYNAMICS AND CONTROL OF GYROSCOPICALLY ACTUATED SPACE-ROBOTIC SYSTEMS

A Dissertation

Presented to the Faculty of the Graduate School

of Cornell University

in Partial Fulfillment of the Requirements for the Degree of

Doctor of Philosophy

by

Michele Deanne Carpenter

January 2009

DYNAMICS AND CONTROL OF GYROSCOPICALLY ACTUATED SPACE-ROBOTIC SYSTEMS

Michele Deanne Carpenter, Ph.D.

Cornell University 2009

Control-moment gyroscopes (CMGs) are power-efficient, internal momentum actuators that produce high torque for the attitude control of spacecraft. CMGs are proposed for actuating joint degrees of freedom in a spacecraft-mounted, agile robotic payload. A kinematics and dynamics analysis is performed for a general open-chain, N-link, N-degree-of-freedom robotic system actuated by CMGs. For an example open-loop maneuver, a CMG system is compared to a system driven by reaction-wheel assemblies (RWAs), which are alternative internal momentum actuators. Numerical simulations demonstrate that a CMG system offers the same agility while using less than 1% of the power of a RWA system with identical dynamics and mass properties. A statistical study demonstrates that only CMGs can provide the output torque necessary to meet the agility requirements of the slew.

With the established kinematics and dynamics for a CMG robotic system, numerical simulations are performed for a general CMG system manipulating a payload. The analysis of an added payload's effects on otherwise reactionless CMG systems motivates the exploration of possible operations concepts for reducing base reactions and power consumption. Simulation results for an example closed-loop maneuver show that base reactions can be significantly reduced, or even eliminated, with CMG actuation while using the same amount of power as a robotic system driven by conventional joint motors.

Power-optimal steering is investigated for a CMG telescope application. A

real-time optimization method is presented that includes null motion in a closed-loop end-effector tracking problem. For a redundant robotic system, there are an infinite number of joint-angle solutions corresponding to a given end-effector attitude. In this optimization algorithm, the joint-angle command corresponding to a commanded end-effector attitude is adjusted with a null-angle component to minimize power while the tracking accuracy remains unchanged. Calculation of the null-angle component is based on a quadratic cost function, which is the sum of the squares of power for each CMG gimbal. Simulation results for an example maneuver demonstrate that the power consumption of the system is reduced by up to 38% when null motion is included in the feedback loop.

BIOGRAPHICAL SKETCH

Michele Deanne Carpenter was born on June 6, 1980 in Westminster, California. She grew up in Lake Forest, California, and graduated from Santa Margarita Catholic High School in June 1998. In October 1998, Michele entered the Astrophysics program at UCLA. In her final year as an undergraduate, she performed research with her freshman physics professor, Dr. Andrea Ghez, reducing observational data to help determine the characteristic properties of the supermassive black-hole candidate, Sagittarius A*, at the galactic center. After receiving the Bachelor of Science degree in June 2002, she traveled to Peru for a month before moving to Boston in September 2002.

While living in Boston, Michele worked as an assistant staff member at MIT Lincoln Laboratory where her work involved the development of discrimination algorithms for the Ballistic Missile Defense division. Her professional experience in challenging engineering projects over the course of two years inspired Michele to apply to various Mechanical and Aerospace Engineering graduate programs.

In August 2004, Michele began graduate study in the Department of Theoretical and Applied Mechanics at Cornell University. She began research with Dr. Mason Peck in January 2005 and received her Ph.D. in January 2009, with a minor concentration in Aerospace Engineering.

ACKNOWLEDGEMENTS

Thank you to everyone who helped and encouraged me through this Ph.D program. There were many times when finishing this dissertation seemed impossible and I would not have kept my sanity without your support.

I would first like to thank my graduate advisor, Dr. Mason Peck, whose influence extended well beyond research. Mason, I am so glad that you were willing to take me under your wing as one of your first graduate students even though I was not officially in your department. You originally proposed the idea of CMG robotics and exploring this problem for the past four years has been a tremendous learning experience. Through all my ups and downs at Cornell, you've been so understanding and supportive and I'm very grateful for having had the opportunity to work with you.

I would also like to thank my other committee members, Dr. Joseph Burns and Dr. Francis Moon, for their support during my time here. Joe, I genuinely appreciate your willingness to serve as my temporary committee chair over these last few years. Without you, I would not have been able to pursue this specific area of research. Frank, I enjoyed our lively conversations about dynamics topics and learned a lot from your many stories.

I am deeply grateful to my peers in the T&AM department who provided vital moral support during the initial years of graduate school. Without your help during the first year, I probably wouldn't have gotten through the Q-Exam. Of course, I need to thank the members of Team Peck who have always been there to share ideas about research. You have all been so supportive and have made my research experience truly enjoyable. I would especially like to thank Daniel Brown, who has been very helpful and patient in our many discussions about CMG topics, and Brett Streetman, who has been my primary source of motivation in the final

push to finish this dissertation. You always listened when I would rant about being stuck on research and knew exactly what to say when I felt discouraged. I can't thank you enough for that.

To my family and friends, I thank you so much for your continuing love and support. I only hope that I can be as supportive in your endeavors as you have been in mine. Obviously, I couldn't have done any of this work without my parents, who made it possible for me to eventually pursue this area of research by supporting my education until the end of my undergraduate career. Finally, I'd like to specifically acknowledge my brother, Scott, who was probably the single person most responsible for my early interest in science. When he gave me my first book about outer space at the age of six, I started telling everyone that I wanted to be an astronaut when I grew up and I haven't stopped since.

TABLE OF CONTENTS

LIST OF TABLES

LIST OF FIGURES

CHAPTER 1

INTRODUCTION

1.1 Overview

External and internal torque actuation are two fundamentally different approaches to orienting a spacecraft payload. External torque is torque imparted to a system, or system component, by an object outside the system while internal torque is torque exerted by one part of a system on another part of the same system. Traditionally, external torques are applied with devices such as jet thrusters, magnetic torque rods, or joint motors. For jointed payloads, external actuation of the joints imparts reaction forces and/or torques onto the spacecraft base while internal actuation offers the possibility of a reactionless system. In addition, electrically-powered internal torque actuators provide propellantless attitude control and have the ability to store electromechanical energy. An internal actuator imparts torque to a system by changing the angular-momentum vector of a spinning rotor. This exchange of angular momentum causes the total angular momentum to be simply redistributed within the system, rather than changed.

The idea of internal actuation leads to the use of momentum actuators for maneuvering rigid-body spacecraft and jointed space-robotic systems. Control-moment gyroscopes (CMGs) are proposed for actuating the space-robotic systems of interest here. CMGs produce torque by changing the direction of its rotor's constant-magnitude angular-momentum vector. Figure 1.1 illustrates the concept of a single-gimbal CMG (SGCMG), which includes a gimbal supporting a rotor that spins with angular velocity, $\boldsymbol{\omega}_{\mathrm{r}} = \omega_{\mathrm{r}} \hat{\boldsymbol{a}}$. The rotor angular-momentum vector, $\mathbf{h}_{\mathrm{r}}$, is also parallel to the spin axis, $\hat{\boldsymbol{a}}$. When the gimbal rotates about the axis,

$\hat{\mathbf{g}}$, the direction of $\mathbf{h}_\mathrm{r}$ is changed, reacting an output torque on the arm segment, $\boldsymbol{\tau}_\mathrm{out}$:

$$\boldsymbol{\tau}_\mathrm{out} = -\boldsymbol{\omega}_\mathrm{g} \times \mathbf{h}_\mathrm{r} \tag{1.1}$$

Since this system conserves angular momentum, the base body experiences a torque that is equal in magnitude and opposite in direction to $\boldsymbol{\tau}_\mathrm{out}$. However, since $\boldsymbol{\tau}_\mathrm{out}$ is orthogonal to the gimbal axis, it is purely a constraint torque that does no work. The associated power is therefore

$$P_\mathrm{CMG} \;=\; \boldsymbol{\tau}_\mathrm{g} \cdot \boldsymbol{\omega}_\mathrm{r}, \tag{1.2}$$

where $\boldsymbol{\tau}_\mathrm{g} = \tau_\mathrm{g}\hat{\mathbf{g}}$ is the gimbal torque vector and $\boldsymbol{\omega}_\mathrm{r} = \omega_\mathrm{r}\hat{\boldsymbol{a}}$ is the rotor angular-velocity vector. Since $\boldsymbol{\tau}_\mathrm{g}$ is orthogonal to $\boldsymbol{\omega}_\mathrm{r}$, the CMG would require no input power if it were fixed and lossless and if the gimbaled inertia were zero.

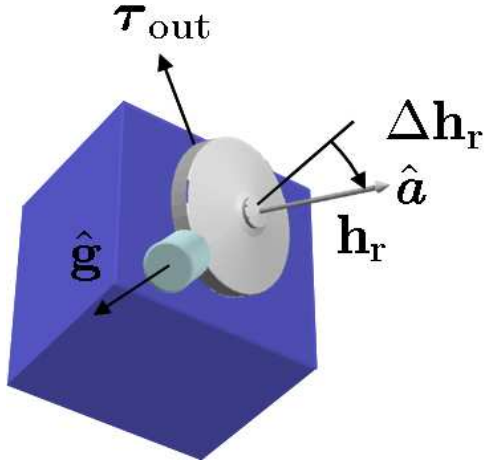

Figure 1.1: A single-gimbal CMG and its associated vectors.

According to Eq. (1.1), the angular velocity of the CMG gimbal, $\boldsymbol{\omega}_{\mathrm{g}}$, governs the torque imparted to the base body, $\boldsymbol{\tau}_{\mathrm{out}}$, and therefore its acceleration. In fact, the kinematics of a CMG are always one derivative lower than those of the body it actuates; i.e., gimbal angle determines base-body rate, gimbal rate determines base-body acceleration, and gimbal acceleration determines base-body jerk.

This dissertation focuses on agile space-robotic systems actuated by CMGs, where "agile" refers to body rates on the order of 1 rad/s. Relevant applications include high-speed target tracking, Earth imaging, and in-orbit servicing. The need for agility can be seen in standard tracking problems. For example, a typical Earth-imaging spacecraft at an altitude of 500 km with an orbital velocity of 7700 m/s must slew at approximately 0.01 rad/s to keep its camera's boresight vector fixed on an object on the Earth's surface. This approximation assumes that the Earth's surface is flat and that the angular distance traveled while tracking the object is small. For a spacecraft tracking spaceborne objects, slew rates must be significantly higher, on the order of 1 rad/s. Agile systems have the additional capability of slewing among multiple simultaneous events. Since an agile system can maneuver without significant delay, more of its resources can be devoted to specific mission tasks.

Analysis is restricted to robotic systems with an open-chain topology, as shown in Fig. 1.2, since 1) this joint structure is the most common for industrial applications, and 2) it is relevant to the Coudé path telescope application examined in later chapters, where the telescope arm segments contain mirrors to reflect light from an end-effector camera onto the focal plane. Closed-chain mechanisms may also prove useful in space-robotics applications, but they are not considered in this work. We investigate an open-chain system containing an arbitrary number of arm

segments interconnected with single-degree-of-freedom revolute joints. There are no joint motors in the system. Each joint is actuated by a CMG scissored pair, which is detailed in Section 2.2.

This dissertation describes the fundamental kinematics and dynamics for a CMG-actuated robotic payload and derives the equations of motion for these mechanisms. With these equations of motion, open-loop and closed-loop control strategies are used to maneuver the CMGs and the robotic arm segments, facilitating analysis of the resulting power consumption and base reactions. While gyroscopic rigid-body control and multi-body dynamics are independently well understood, the use of CMGs for actuating robotic arm segments is a new contribution to the field of space robotics that addresses the central issues of base-reaction disturbances and limited power resources in a space environment. Solutions to these issues enable improved in-orbit construction and repair, which are highly relevant to NASA's Vision for Space Exploration.

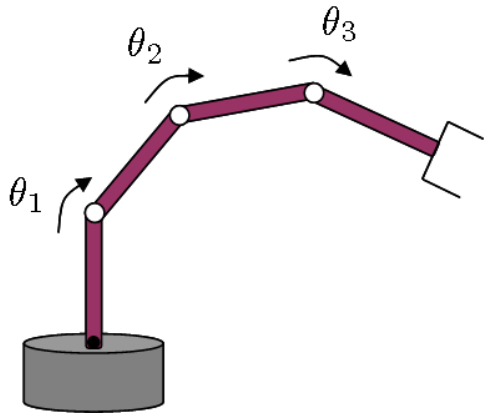

Figure 1.2: Open kinematic chain robot arm.

This chapter continues with a literature review of previous work investigating 1) the mitigation of base reactions caused by maneuvering a robotic system, 2) methods for reducing power consumption in spacecraft actuation, and 3) methods

for dealing with issues specific to CMGs, e.g., singular CMG gimbal configurations. This chapter concludes with a summary of key contributions and an overview of the remaining content of the dissertation.

1.2 Literature Review

The concept of gyroscopically actuated space-robotic systems was initially proposed by Billing-Ross and Wilson in 1988 [1] for the dynamic isolation of a payload from the spacecraft base. CMGs were independently proposed by Peck in 2005 [2, 3] for low-power actuation of agile robotic systems with the potential for a reactionless design. This concept was expanded to produce the material described in Chapter 2, which was also published in 2008 [4]. Subsequent work in reducing power and base reactions for a robotic system with CMG actuation is described in Chapters 3 and 4, and draws from material in [5, 6] and [7, 8], respectively.

1.2.1 Base-Reaction Mitigation

Steering a gimbaled spacecraft payload independently of the spacecraft bus can be accomplished in many ways, including the obvious application of torque to each joint by a motor [9]. However, for space-robotic systems mounted on free-flying satellites, the common robotics-centric assumption of an inertially fixed base during arm motions cannot be applied. The commanded motion of the robot arm imparts reaction forces and torques onto the spacecraft base, contributing to end-effector trajectory tracking errors. Such disturbances can also adversely affect the spacecraft bus, which may feature a precision optical payload or sensitive micro-

gravity experiment. Finally, these disturbances are likely to result in the consumption of additional fuel by compensating reaction jets in the attitude-control system (ACS), which can greatly limit mission lifetime. These difficult challenges, unique to space-robotic systems, among others, are reviewed by Dubowsky and Papadopoulos in their survey paper [10]. Researchers have investigated a variety of methods for reactionless steering to address these important issues. Wu and Gosselin [11, 12] consider methods for dynamic balancing of multi-degree-of-freedom mechanisms, which include the addition of counterweights and counter-rotations to balance reaction forces and torques. However, eliminating base reactions through the dynamic balancing of spatial (non-planar) multi-degree-of-freedom mechanisms is a complex problem and has consequently received very little treatment. Even successful dynamic balancing of the robotic manipulator comes at the expense of a substantial increase in system mass and complexity. Adding counterweights to the joints and actuators can also reduce the agility of the system. After computing the kinematics for a general robotic system and the resulting attitude disturbances on the spacecraft, Longman *et al.* [13] demonstrate that three orthogonally-mounted reaction wheels in the ACS can be commanded to compensate for the robot motion so that the total moment about the system mass center is zero. They further show that induced translational motion of the base can be counteracted by using a set of augmented inverse-kinematic relations when calculating the commanded joint variables. Along the same lines, Oda and Ohkami [14] describe a feed-forward compensation technique in the attitude control of a satellite, which includes the use of reaction wheels and gas jet thrusters to cancel the base reactions produced by the motion of an attached robotic manipulator. Path-planning algorithms have also been proposed to reduce dynamic disturbances on the spacecraft. Quinn *et al.* [15] develop trajectory-planning strategies for kinematically-redundant robots

by minimizing a weighted, quadratic cost function that incorporates the forces and torques transmitted to the base.

In addition to these methods that achieve reactionlessness by compensating for robot motions, researchers have also investigated actuation solutions. Unlike external actuators, such as reaction jets or direct-drive motors, internal momentum actuators can provide reactionless actuation of the robotic arm segments. Momentum-exchange devices include reaction-wheel assemblies (RWAs) and CMGs. These devices apply torque by exchanging their angular momentum with the payload, maintaining a constant system angular momentum. An RWA consists of a rotor that accelerates about a constant axis in a body-fixed frame. RWAs have less design complexity than other momentum-exchange devices due to their simpler assembly and balancing, resulting in reduced manufacturing cost. There are also straightforward control laws associated with using RWAs in spacecraft attitude control. However, these actuators use a prohibitive amount of power for very limited torque capability, with a maximum output torque typically on the order of 1 N-m [16]. The electromechanical power required for the RWA to generate a torque is

$$P_{\mathrm{RWA}} = \boldsymbol{\tau}_{\mathrm{r}} \cdot \boldsymbol{\omega}_{\mathrm{r}}, \tag{1.3}$$

where P_{RWA} is the shaft power imparted by the wheel and $\boldsymbol{\tau}_{\mathrm{r}}$ represents the vector torque applied when the rotor speed $\boldsymbol{\omega}_{\mathrm{r}}$ is changed. It is evident from Eq. (1.3) that excessive amounts of power are required even for systems with low agility since power scales with the RWA spin speed, which is typically 5000-6000 rpm [17].

For agile robotic systems, where high torques are needed to achieve body angular rates on the order of a radian per second, alternative actuation methods must be considered. CMGs are considered in this dissertation for such applications. When using momentum-exchange devices for actuation, the robotic system has the potential for a completely reactionless design. Among the reactionless actuation methods for space robots, Pathak *et al.* [18] present a continuously variable transmission (CVT) torque-generation device to broaden the control strategies that are possible for attitude control of a reactionless space robot. Osuka *et al.* [19, 20] and Yoshida *et al.* [21] propose using RWAs to drive a robotic manipulator with a SCARA-like joint structure. The authors assert that a significant merit of their architecture is its ability to serve as a redundant actuator system by allowing an arbitrary number of "torque units" in arbitrary locations on each arm segment. This dissertation examines the use of CMG actuation as an alternative to RWAs for reactionlessness and high agility while consuming very little power.

1.2.2 Power Reduction for Agile Spacecraft

Power is in short supply on any spacecraft, but in the case of attitude control for small, agile spacecraft, power consumption is a primary design driver. As stated in Section 1.2.1, the use of thrusters as an alternative to solar-powered electrical actuators is undesirable for small spacecraft because propellant cannot be replaced after the spacecraft is launched, and launch-vehicle fairing size ultimately limits the capacity of propellant tanks. For an agile system, limited propellant motivates the use of electrically-powered actuators.

Flywheels have been proposed for the attitude control of spacecraft, as well as for storing the energy needed by the spacecraft to perform its tasks. Evidence

has been presented to support the idea that flywheels can serve as both attitude-control actuators as well as energy-storage mechanisms, thus eliminating the need for propellant or chemical batteries. Most spacecraft use chemical batteries to store the energy produced by solar panels during times of exposure to the sun [22]. However, besides having a limited cycle life, batteries comprise a power system that is separate from the attitude-control system, incurring additional mass. Roes first proposed the concept of flywheel energy storage in 1961 [23]. Subsequent feasibility studies performed by Adams [24] and Notti *et al.* [25, 26, 27] show that the use of flywheels in an integrated power and attitude control system (IPACS) can significantly reduce spacecraft weight and cost. Different flywheels are investigated to perform these dual functions. Since CMGs operate at constant rotor speeds, they are not free to store or drain energy. RWAs provide the capability to store and drain electrical energy, but are limited in the amount of torque they can produce. Momentum wheels are typically used to contribute a momentum bias to a gyrostat [28] and operate around a high nominal spin speed, but have the same torque limitation as RWAs. Tsiotras *et al.* [29] examine a system of four momentum wheels that integrates the attitude-control and energy-storage functions. Variable-speed control-moment gyroscopes (VSCMGs), or single-gimbal CMGs with a variable rotor spin speed, have also been proposed for small satellites as a means to combine these functions while maintaining a high torque capability [30, 31, 32, 33].

Researchers have investigated a variety of methods to reduce power consumption for a rigid-body spacecraft that use momentum-exchange devices for attitude control. Zhang *et al.* [34] and Ma *et al.* [35] propose the use of superconducting magnetic bearings for RWAs on a small satellite to reduce the power dissipation associated with standard mechanical bearings. References [36, 37, 38] alternatively investigate the use of small-scale CMGs to reduce power on a small spacecraft. Lap-

pas *et al.* [36] reports results from an experiment comparing the power required by a CMG cluster to that required by an RWA cluster. While the comparison is not ideal - no existing RWA can produce torque comparable to that of a CMG - the experimental results confirm that CMGs are more power-efficient actuators than RWAs.

In addition to these power-reduction methods, researchers have also examined techniques for minimizing a power cost. Bayard [39, 40] develops an algorithm for orienting three RWAs on a small spacecraft such that a weighted cost function based on torque, momentum storage, and power consumption is optimized. Skaar and Kraige [41, 42] discuss optimal maneuvers of an RWA-driven spacecraft, which minimize RWA power. Vadali and Junkins [43] discuss optimal large-angle rotational maneuvers of an RWA-driven spacecraft, which minimize the time integral of the sum of RWA motor torques. Yang and Wu [44] develop an algorithm to maneuver a rigid-body spacecraft with three momentum wheels while minimizing a cost consisting of the control torques and slew duration. However, each of these studies present solutions resulting from optimal control strategies that require the initial and final attitude states to be specified *a priori*. Rather than using optimal control techniques, Schaub [45] demonstrates locally power-optimal feedback control for the attitude of a rigid-body spacecraft with a redundant RWA cluster.

1.2.3 Singularity-Avoidance Methods

Sections 1.2.1 and 1.2.2 have presented CMG actuation as an attractive solution for base-reaction and power consumption issues that arise in space robotics; however, a well-known disadvantage of using CMGs is the presence of singular configurations, which occur when there are one or more directions in which the CMG arrangement

cannot produce a torque. Even approaching such a configuration can result in the command of impossibly high gimbal rates. Existing singularity-avoidance methods include a variety of steering algorithms and CMG array geometries.

Steering laws for singularity avoidance have been developed for three-degree-of-freedom spacecraft attitude control. Kurokawa [46] reviews the major classes of CMG steering laws with a qualitative evaluation of their ability to perform attitude control. However, he concludes that there is no perfect steering law, since effectiveness depends on the specific mission requirements. The CMG steering problem involves determining the gimbal rates that achieve a commanded output torque while satisfying certain constraints, particularly avoiding singular gimbal configurations. Also possible are external (saturation) singularities, in which the CMGs are oriented such that they store the maximum possible angular momentum, but these configurations cannot be avoided. The pseudoinverse method is typically used in the development of CMG steering laws, but the resulting gimbal-rate commands do not avoid singular CMG configurations. Singularity-avoidance algorithms are based on the singularity-robust (SR) inverse method, which was originally developed to solve the inverse-kinematics problem for robotic manipulators by Nakamura and Hanafusa [47]. Oh and Vadali [48] derive the equations of motion for a body with multiple CMGs and develop a singularity-robust control law for the gimbal accelerations based on Lyapunov stability theory [49]. Ford and Hall [50] modify the control law of Oh and Vadali by manipulating the transformation relating gimbal rates to output torques. The singularity-avoidance parameter in the control law is based on the smallest singular value of the pseudoinverse of this transformation, which indicates the closeness of the CMG gimbal configuration to a kinematic singularity. This modified control law, sometimes called the Singular Direction Avoidance (SDA) steering law, more accurately produces the

commanded torque near singular configurations, allowing smoother reorientation of the spacecraft.

Null-motion algorithms are considered in numerous singularity-avoidance studies for a rigid-body spacecraft with a redundant CMG array. To address the singularity-avoidance problem, [48, 50, 51, 52, 53, 54, 55, 56, 57, 58, 59] exploit the null space of the Jacobian relating commanded torques to gimbal rates. In these studies, steering laws are developed that incorporate null motion into the pseudoinverse of the transformation relating CMG gimbal rates to output torques. Actuator redundancy is required for the implementation of any null-motion algorithm. The gimbal-rate outputs from the pseudoinverse approach are multiplied by a scaled null vector, whose scaling is governed by the proximity of the configuration to an internal singularity. Cornick [51] presents two steering laws for a pyramid cluster of six CMGs: One steering law uses the "direct method" of adding null motion to steer in the direction opposite to the most rapidly approaching singularity and the other uses the "indirect method," which adds null motion to steer the gimbal angles toward the saturation singularity while indirectly avoiding the remaining singularities. Cornick also considers gimbal-rate limits of the CMG hardware in the performance analysis of these methods. Vadali *et al.* [53] use null motion for positioning gimbals in a standard 4-CMG pyramid configuration into an initial configuration guaranteed to avoid internal singularities for a given maneuver. This initial configuration is computed off-line before executing the maneuver. Wie *et al.* [56, 60, 58] explore mathematical variations on the singularity-robust inverse method for singularity avoidance. In [60, 58], Wie presents a singularity-avoidance approach suitable in cases where precision tracking is not required during reorientation slews. The approach, sometimes called the Off-Diagonal Singularity Robust (o-DSR) method, modifies the more standard SR method [47, 48] with a weight-

ing matrix containing nonzero off-diagonal elements instead of a diagonal matrix. The o-DSR steering law causes the gimbal angles to rapidly approach and move through internal singularities when needed. Jung and Tsiotras experimentally compare three of the most commonly-studied, pseudoinverse-based steering laws, including the o-DSR method, the SR method, and the SDA method [61]. Their experimental results suggest that the o-DSR method has the best overall performance with the smallest torque error when singularities are present. Lee and Rhee also present experimental results for the SR method and the o-DSR method, verifying the predicted advantages of the steering laws in the presence of singularities [62].

An alternative to implementing steering algorithms for singularity avoidance is the consideration of different classes of CMGs. Other types of CMGs that may be considered in a trade study for reactionless devices include the double-gimbal CMG (DGCMG) and the hybrid VSCMG. A DGCMG consists of a single rotor supported by two gimbals, providing two degrees of freedom. Cook *et al.* [63] investigate the advantages of DGCMGs over SGCMGs in particular applications, such as very large spacecraft (e.g. the International Space Station) that do not have rapid maneuvering requirements. VSCMGs were briefly described in Section 1.2.2 as a means to combine the attitude-control and energy-storage functions on a spacecraft. References [64, 55, 65] also claim that VSCMGs can eliminate redundant batteries, reduce spacecraft mass, and provide the ability to steer through singular gimbal configurations. However, combining CMG and RWA capabilities in a single architecture leads to a more massive and complex actuator with the same poor power performance as an RWA. Therefore, this dissertation treats only single-gimbal CMGs as space-robotics actuators.

The final method of singularity avoidance involves exploiting certain CMG array geometries. A pyramid configuration of four SGCMGs is the standard architecture used in the development of singularity-avoidance steering laws. Margulies and Aubrun [66] and Kurokawa [67] present the geometric theory of SGCMG systems in this configuration and classify the internal singularities. This dissertation eliminates internal singularities by arranging the CMGs into scissored-pair configurations. Research on CMG scissored-pair configurations for three-axis attitude control dates to the 1960s. Havill and Ratcliff [68] and Crenshaw [69] were the first to perform detailed analyses on scissored pairs, demonstrating that the singularity problem for a CMG-actuated spacecraft can be greatly improved by considering different architectures rather than complicated steering laws. Liska [70] examines the mechanical synchronization of DGCMG pairs to achieve high torque capability with desirable system size, weight, and power properties. Aubrun and Margulies [71] study scissored-pair arrays of gyrodampers for the amplified damping of rigid-body rotations. Cunningham and Driskill [72] describe the three-scissored-pair architecture of CMGs that were used for attitude control of the Astronaut Maneuvering Research Vehicle during the 1970s. References [68, 69, 73, 74, 75] explain that the full momentum range of an array of scissored pairs is reduced, but nonsingular. Only saturation singularities are present, which is no different from any other physically realizable actuator. When considering alternative actuation methods, there are other clear trade-offs among these saturation singularity issues, weight, manufacturing cost, and complexity. These design considerations are explored in [1, 76, 77].

1.3 Dissertation Contributions and Overview

The primary objectives of this dissertation are to establish the fundamental theoretical background for a CMG robotic system and to validate this theory via simulation of relevant examples motivated by current needs in space robotics. The key contributions include:

- Fusion of gyroscopic rigid-body control with multi-body dynamics to address major issues in space robotics, including base-reaction disturbances and power efficiency.
- Novel dynamics and control architectures for low-power, high-agility, and potentially reactionless robots.
  - Development of kinematic equations for a general CMG robotic system.
  - Development of equations of motion for a general CMG robotic system.
  - Synthesis of a control algorithm with a general CMG robotic system.
- Comparison studies of robotic actuation methods.
  - Power-consumption comparison of CMG systems to RWA systems with identical mass properties
  - Base-reaction comparison of CMG systems to conventional systems actuated by simple joint motors
- Comparison studies of operations concepts for CMG and conventional systems.
  - Power-consumption and base-reaction comparison of simultaneously driven arm segments to sequentially driven arm segments in a simple step maneuver for general CMG systems.

- On-line, power-optimal steering strategy for a CMG robotic system performing end-effector trajectory tracking without future path knowledge.

A kinematics, dynamics, and control architecture is developed for a general CMG robotic system, which refers to an open-chain system with N arm segments, N degrees of freedom, arbitrary mass properties, and arbitrary joint axes. For the numerical simulations in this dissertation, the equations of motion are simplified with an orthogonal joint-axis structure. System behavior is analyzed for large-angle, high-speed motions.

This dissertation comprises five chapters. This chapter contains the introductory material, including the problem overview, basic CMG dynamics, and a literature review covering techniques for base-reaction mitigation, power reduction in agile spacecraft, and singularity-avoidance methods unique to CMG clusters. Chapter 2 establishes the fundamental kinematics and dynamics for a general CMG robotic system and evaluates the feasibility of using CMGs and RWAs to actuate an agile robotic imaging payload. This work compares the power consumption of a CMG system to an RWA system with identical dynamics and mass properties, demonstrating that only CMGs are capable of producing the required torque for the agile system. Chapter 3 investigates how the choice of actuation method and operations concept affect base-reaction disturbances and power consumption while manipulating a payload in an arbitrary, closed-loop, pick-and-place maneuver. A feedback-control law is developed for the closed-loop maneuvers. The kinematics and dynamics theory from Chapter 2 are used to 1) compare the base reactions of a CMG system to a conventional system with direct-drive joint motors, 2) compare the power consumption and base reactions of a CMG system using different operations concepts, and 3) compare the power consumption for general and mass-

balanced systems using both actuation methods. Chapter 4 develops an algorithm for real-time, power-optimal control of a redundant robotic system performing end-effector trajectory tracking. The kinematic relationships between the joint and end-effector coordinates are determined. The development of a cost function related to system power is discussed. A null-motion algorithm for minimization of this power cost is presented and implementation issues are reviewed. Finally, Chapter 5 summarizes the conclusions from this work and discusses possible future directions for CMG-based robotics.

CHAPTER 2

DYNAMICS OF A CMG ROBOTIC SYSTEM[1]

2.1 Introduction

This chapter evaluates the use of CMGs in a spacecraft-mounted, agile imaging payload, whose tasks include slewing to acquire and track a high-speed target. However, the results from this analysis apply equally well to other applications, such as robotic arms for in-orbit construction and repair. In a system required to perform fast slews, CMG actuation is especially desirable because it provides much higher torque for input power than RWAs [78]. On the other hand, a well-known disadvantage of using CMGs for spacecraft attitude control is the existence of singular gimbal configurations, which occur when there are one or more directions in which the CMG arrangement cannot produce a net torque on the spacecraft. Even approaching such a configuration can result in the command of impossibly high gimbal rates [50, 79, 80]. In this study, internal singularities are eliminated with scissored-pair configurations of CMGs. Section 2.2 discusses the scissored-pair architecture in more detail.

Figure 2.1 illustrates an example of the proposed system for the numerical analysis, which includes three connected, CMG-actuated arm segments with an inertia dyadic that is approximately constant during slews. While the theoretical analysis in this chapter considers the general case in which the CMG robotic payload has

a time-varying inertia dyadic in an inertial frame, this general system is simulated only in Chapter 3. The complexity added to the dynamics with a time-varying payload inertia dyadic does not change the fundamental results of the study in this chapter. Section 2.2 describes the key features of the system of interest and defines the kinematics for the general CMG robotic payload with an arbitrary number of arm segments. Section 2.3 discusses the dynamics of this system and derives the full nonlinear equations of motion. This theoretical analysis accounts for the case in which the spacecraft bus is moving relative to an inertial frame and the case in which the bus is inertially fixed. Section 2.4 presents simulation results comparing a three-link, reactionless CMG system to an identical system driven by RWAs in an open-loop maneuver, demonstrating that a CMG system can outperform an RWA system by orders of magnitude in power usage.

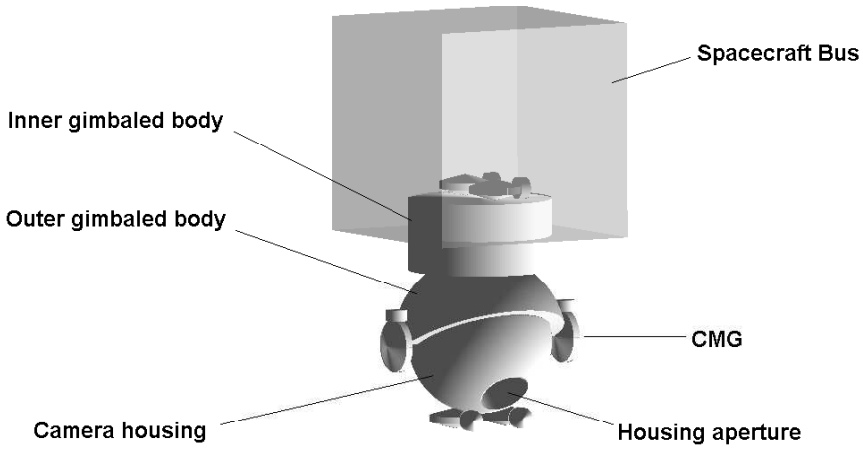

Figure 2.1: Example spacecraft concept with body-fixed CMGs where the system inertia dyadic is approximately constant.

2.2 System Description and Kinematics

This study begins with the description of a general CMG robotic payload containing an arbitrary number of bodies interconnected with single-degree-of-freedom revolute joints. The joint axis of a given body is orthogonal to those of its adjacent neighbors. Each body carries a single scissored pair of CMGs [4, 2, 3]. The scissored-pair concept is depicted in Fig. 2.2(a) along with its associated vectors. A scissored pair consists of two identical single-gimbal CMGs that share a gimbal axis. The CMGs rotate with equal-magnitude gimbal angles in opposite directions. In this configuration, the rotor angular-momentum vectors $\mathbf{h}_1$ and $\mathbf{h}_2$ rotate in a plane orthogonal to the gimbal axis such that their vector sum lies along the joint axis. The off-axis momentum canceled by the scissored pair would not activate a joint axis directly, but it can couple into the motion of the other joints. As a design convenience, we consider only the case of scissored pairs rather than the more general case of arbitrary CMG configurations. Since the scissored-pair configuration constrains the output torque to always act along the joint axis, the output torque is singular only at saturation, when the CMG rotor angular-momentum vectors are parallel to the joint axis and the maximum amount of angular momentum is stored in the scissored pair. Figure 2.2(b) shows how the scissored pair would actuate an arm segment.

The prospect of saturation represents a possible disadvantage in using this architecture, namely that the CMGs cannot provide constant torque for arbitrary maneuvers of arbitrary duration. However, that disadvantage may be irrelevant for space-based applications. Other possible disadvantages include added mass in the system and a restricted momentum envelope due to the mechanical constraint on the CMGs. However, these issues are introduced for the purpose of eliminating

internal singularities, in which the total angular momentum of the CMGs actuating a joint is minimally projected onto the joint axis. For precision maneuvers, any disadvantage associated with using scissored pairs is a favorable alternative to dealing with these singularities that occur with alternate CMG configurations. Elgersma *et al.* [81] discuss errors that arise due to some CMG singularity-avoidance methods.

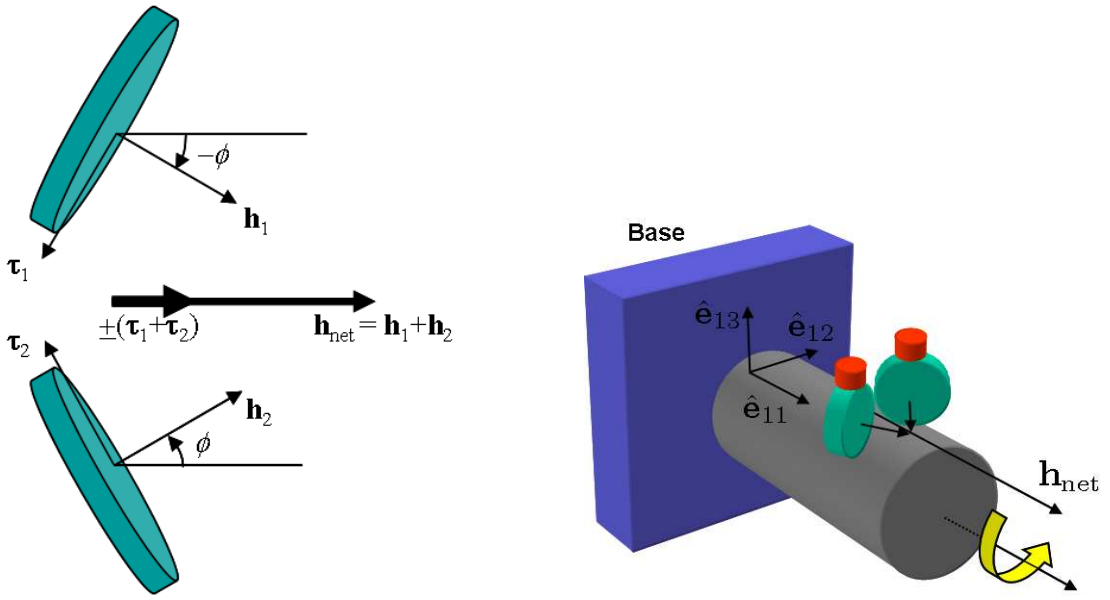

(a) Top-view schematic of scissored pair with its associated vectors.

(b) Scissored-pair implementation on a single-degree-of-freedom jointed body.

Figure 2.2: CMG scissored-pair configuration.

In addition to its simple, singularity-robust arrangement, the mechanical linkage between the two gimbals can save power [75]. This feature helps to motivate the choice of a scissored-pair architecture, even though it is not exploited in this study. Appendix A includes figures of prototype CMG robotic arms, demonstrating examples of how the CMG scissored pairs might be mounted in a space-robotic system.

Expressing the kinematics of this system first requires a choice of reference configuration. The clockwise-spiral configuration illustrated in the three-body example of Fig. 2.3 yields the simplest generalization of rotation matrices. $\hat{\mathbf{e}}_{ij}$ represents the basis vector along the j direction in the coordinate system fixed to body i. The body-i-fixed coordinate system is centered at the intersection of the body i and body $i-1$ joint axes. For the innermost body, the local coordinate system is centered at the intersection of the joint axis and the base body. An arbitrary number of robotic arm segments may be included in this model. It is unimportant that this reference configuration may be physically unrealizable for a system with arbitrary geometry.

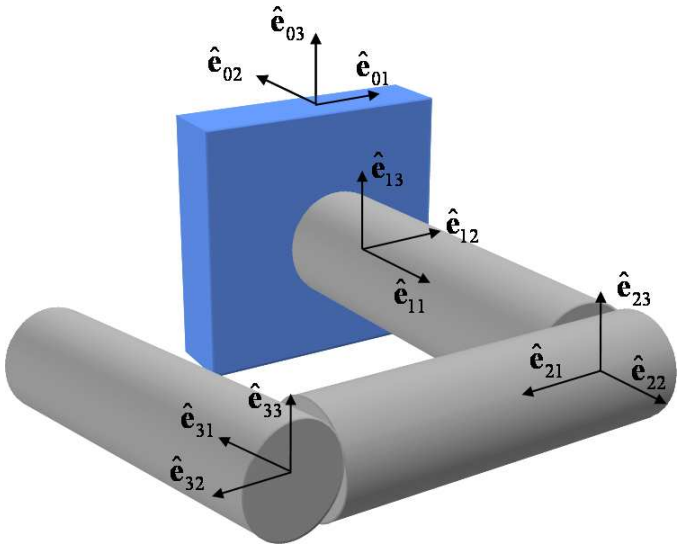

Figure 2.3: Clockwise-spiral reference configuration for the robotic payload with sets of body-fixed basis vectors.

In this reference configuration, each body-fixed set of basis vectors can be expressed via a linear transformation on the body-fixed basis vectors of its neighboring inboard body. The basis vectors of any frame can be organized more compactly into a vectrix [28], or matrix of vectors, $\mathbf{e}_i = [\hat{\mathbf{e}}_{i1}, \hat{\mathbf{e}}_{i2}, \hat{\mathbf{e}}_{i3}]^{\mathrm{T}}$. The coordinate trans-

formation is achieved with

$$\mathbf{e}_i = {}^iQ^j\mathbf{e}_j, \tag{2.1}$$

where ${}^iQ^j$ is the direction-cosine matrix from body j to body i coordinates. Using Euler angles leads to matrices that are difficult to generalize, so we use axis-angle parameters for this purpose. Since adjacent coordinate systems are not aligned in this reference configuration, we perform a linear transformation L on the rotation matrix R

$${}^{i-1}Q^i = LR = \begin{bmatrix} 0 & 1 & 0 \\ -1 & 0 & 0 \\ 0 & 0 & 1 \end{bmatrix} \cdot [\cos\theta_i \mathbf{1} + (1-\cos\theta_i)\ {}^ia\ {}^ia^{\mathrm{T}} + \sin\theta_i\ {}^ia^{\times}], \tag{2.2}$$

where

$$L = \begin{bmatrix} 0 & 1 & 0 \\ -1 & 0 & 0 \\ 0 & 0 & 1 \end{bmatrix}, \tag{2.3}$$

${}^ia$ refers to the spin axis of body i expressed in body i coordinates, and ${}^ia^{\times} \in \mathbb{R}^{3\times3}$ is the skew-symmetric matrix representation of a cross product involving ${}^ia$. To clarify the notation, the variable $\boldsymbol{a}$ is a vector representing a body's spin axis that is independent of the choice of basis. The column matrix $a \in \mathbb{R}^3$ results from projecting $\boldsymbol{a}$ onto a particular choice of basis vectors. The superscript i indicates which set of basis vectors has been used. Also in Eq. (2.2), $\mathbf{1} \in \mathbb{R}^{3\times3}$ is the identity matrix and θ_i is the angular position of body i relative to body $i-1$. Figure 2.4 illustrates the relative joint angles for the system of interest where $N = 3$.

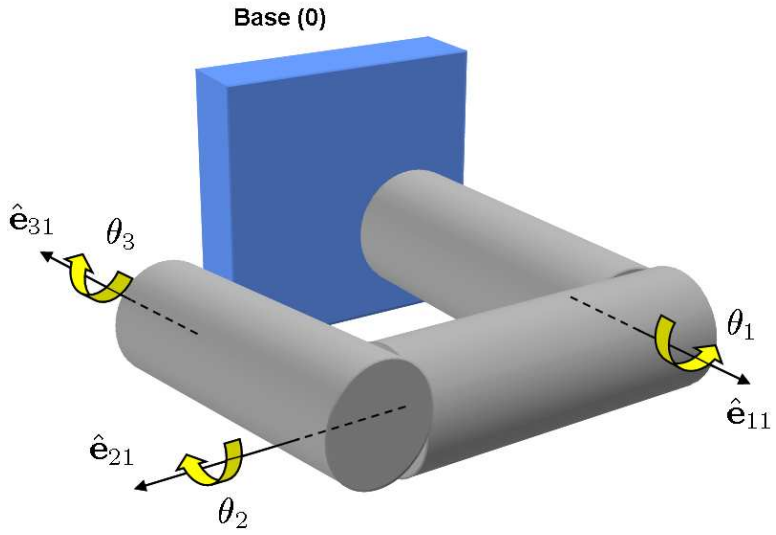

Figure 2.4: Relative joint angles, θ_i, for system of interest with $N = 3$.

The general expression for the orientation of body j relative to body i in terms of the relative body angles is

$$ {}^{i}Q^{j} = {}^{i}Q^{i+1}\ {}^{i+1}Q^{i+2} \ldots {}^{j-1}Q^{j} = \prod_{k=i}^{j-1} {}^{k}Q^{k+1}. \tag{2.4} $$

A body in this robotic payload can only rotate about its 1-axis, so $\boldsymbol{a} = \hat{\mathbf{e}}_{i1}$ for any body i and the component matrix a is $[1\ 0\ 0]^{\mathrm{T}}$. With this fact, we substitute Eq. (2.2) into Eq. (2.4) and find the following direction-cosine matrix for the multi-body payload:

$$ {}^{i}Q^{j} = \prod_{k=i}^{j-1} L \cdot \left\{ \cos\theta_{k+1}\mathbf{1} + (1-\cos\theta_{k+1}) \begin{bmatrix} 1 & 0 & 0 \\ 0 & 0 & 0 \\ 0 & 0 & 0 \end{bmatrix} + \sin\theta_{k+1} \begin{bmatrix} 0 & 0 & 0 \\ 0 & 0 & -1 \\ 0 & 1 & 0 \end{bmatrix} \right\}. \tag{2.5} $$

Figure 2.5 illustrates a three-body robotic payload attached to a free-flying

spacecraft base in which the attitude and position of the base are time-varying in an inertial frame. This concept can be extended for payloads with an arbitrary number of bodies. A free-flying space-robotic system, which includes an N-degree-of-freedom robotic arm and a six-degree-of-freedom base, has $N + 6$ degrees of freedom. With the reference configuration in Fig. 2.5, expressions are developed for the motion of the body mass centers. Let $\mathbf{L}_i$ represent the constant-length position vector from the reference point O_i fixed in the frame of body i to the reference point O_{i+1} fixed in the frame of body $i+1$. The vector $\mathbf{r}_i$ is the constant-length position vector of body i's mass center measured from O_i. The vector $\mathbf{R}_i$ is the position vector of body i's mass center measured from the fixed point $\mathrm{O}_{\mathcal{N}}$, which is the origin of the inertial coordinate system. The base contact O_1 is the origin of both the 0 frame and the 1 frame, and is also the location of the base mass center. The position, velocity, and acceleration vectors for the mass center of an arbitrary body i on the payload ($i > 0$), when measured from $\mathrm{O}_{\mathcal{N}}$, are

$$\mathbf{R}_i = \mathbf{R}_0 + \sum_{j=1}^{i-1}(\mathbf{L}_j) + \mathbf{r}_i \ , \tag{2.6}$$

$$\mathbf{V}_i = \mathbf{V}_0 + \sum_{j=1}^{i-1}(\boldsymbol{\omega}^{j/\mathcal{N}} \times \mathbf{L}_j) + \boldsymbol{\omega}^{i/\mathcal{N}} \times \mathbf{r}_i \ , \tag{2.7}$$

$$\begin{aligned} \mathbf{A}_i = \mathbf{A}_0 &+ \sum_{j=1}^{i-1}\left[{}^j\frac{d}{dt}\boldsymbol{\omega}^{j/\mathcal{N}} \times \mathbf{L}_j + \boldsymbol{\omega}^{j/\mathcal{N}} \times (\boldsymbol{\omega}^{j/\mathcal{N}} \times \mathbf{L}_j)\right] \\ &+ {}^i\frac{d}{dt}\boldsymbol{\omega}^{i/\mathcal{N}} \times \mathbf{r}_i + \boldsymbol{\omega}^{i/\mathcal{N}} \times (\boldsymbol{\omega}^{i/\mathcal{N}} \times \mathbf{r}_i) \ . \end{aligned} \tag{2.8}$$

$\mathbf{R}_0$, $\mathbf{V}_0$, and $\mathbf{A}_0$ are the position, velocity, and acceleration vectors for the mass center of the spacecraft base when measured from $\mathrm{O}_{\mathcal{N}}$. Equations (2.6)-(2.8) introduce notation that will be used for the remainder of this dissertation. $\boldsymbol{\omega}^{i/j}$ is the angular velocity of frame i relative to frame j. $\mathcal{N}$ denotes the inertial frame.

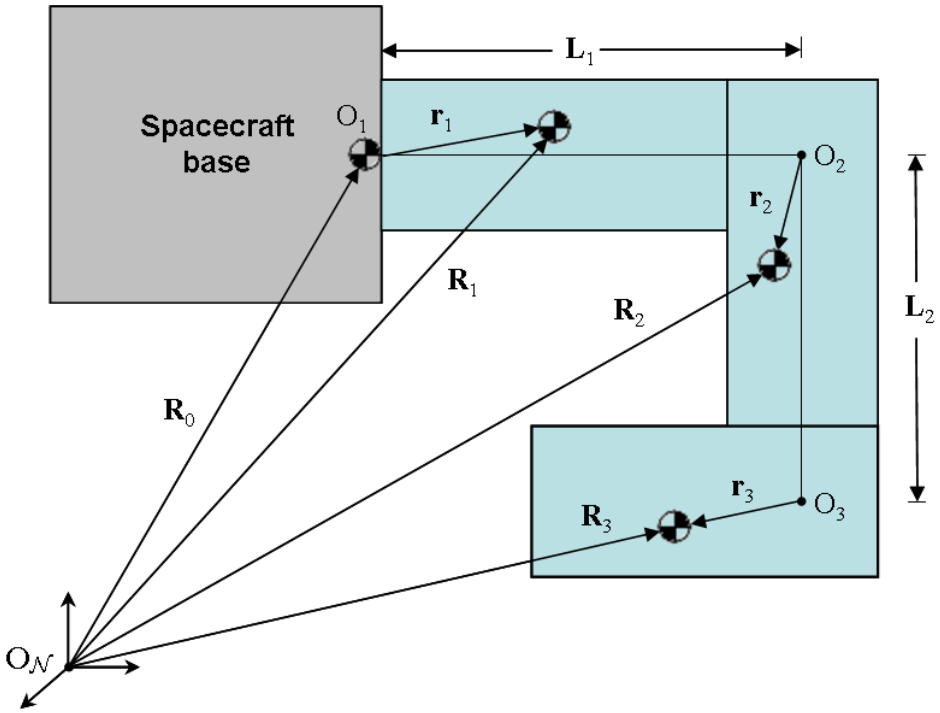

Figure 2.5: Reference configuration for the general three-body robotic payload attached to a free-flying spacecraft base.

Rotating reference frames are numbered, with 0 corresponding to the frame fixed in the spacecraft base and $1, 2, \ldots, N$ corresponding to the frames fixed in each arm segment from innermost to outermost. ${}^{i}d/dt$ is the time derivative in the i frame.

2.3 Dynamics and Equations of Motion

Our dynamical analysis begins with the simple case of a single body actuated by a CMG scissored pair. For this exercise, we consider a system in which the spacecraft base is stationary. Figure 2.6 illustrates the reference configuration for this system, which consists of the payload attached to a stationary base. However,

this initial exercise considers only a single-body payload. A dotted line encircles a control volume that isolates the payload from the rest of the spacecraft. In the single-body system, which includes only the arm segment and its CMG scissored pair, the 0 frame corresponds to the inertial frame and $\boldsymbol{\omega}^{0/\mathcal{N}}$, $\mathbf{R}_0$, $\mathbf{V}_0$, $\mathbf{A}_0$ are each equal to $\mathbf{0}$ in Eqs. (2.6)-(2.8). With a sufficiently high-bandwidth motor, the rotor angular velocity is taken to be constant in the rotor frame. It is also constant in the gimbal frame. The system is rotating about an arbitrary axis that does not pass through its mass center, but we assume that the motion of the CMGs is such that the system mass center is constant in the 1 frame. A convenient reference point for this system is the intersection of the body's joint axis with the stationary base, or O_1, in Fig. 2.6. The system angular momentum relative to this fixed point is

$$\begin{aligned}\mathbf{H}_1 &= \mathbf{I}_{1\mathrm{C}} \cdot \boldsymbol{\omega}^{1/0} + \mathbf{R}_1 \times m_{1\mathrm{C}} \left(\boldsymbol{\omega}^{1/0} \times \mathbf{R}_1\right) \\ &\quad + (\mathbf{I}_{\mathrm{G}_1} + \mathbf{I}_{\mathrm{R}_1}) \cdot \boldsymbol{\omega}^{\mathrm{G}_1/1} + (\mathbf{I}_{\mathrm{G}_2} + \mathbf{I}_{\mathrm{R}_2}) \cdot \boldsymbol{\omega}^{\mathrm{G}_2/1} \\ &\quad + \mathbf{I}_{\mathrm{R}_1} \cdot \boldsymbol{\omega}^{\mathrm{R}_1/1} + \mathbf{I}_{\mathrm{R}_2} \cdot \boldsymbol{\omega}^{\mathrm{R}_2/1}. \end{aligned} \tag{2.9}$$

$\mathbf{I}_{1\mathrm{C}}$ is the composite inertia dyadic for the arm segment and the CMGs with total mass, $m_{1\mathrm{C}}$. $\mathbf{I}_{\mathrm{G}_1}$ and $\mathbf{I}_{\mathrm{G}_2}$ are the inertia dyadics for the CMG gimbals while $\mathbf{I}_{\mathrm{R}_1}$ and $\mathbf{I}_{\mathrm{R}_2}$ are the inertia dyadics for the CMG rotors. The inertia dyadic for each component is taken relative to that component's mass center. In addition, G_i and R_i also represent the ith gimbal-fixed frame and the ith rotor-fixed frame, respectively. The rotor angular velocities relative to body 1 are expressed as a sum of rotor and gimbal angular velocities, and Eq. (2.9) becomes

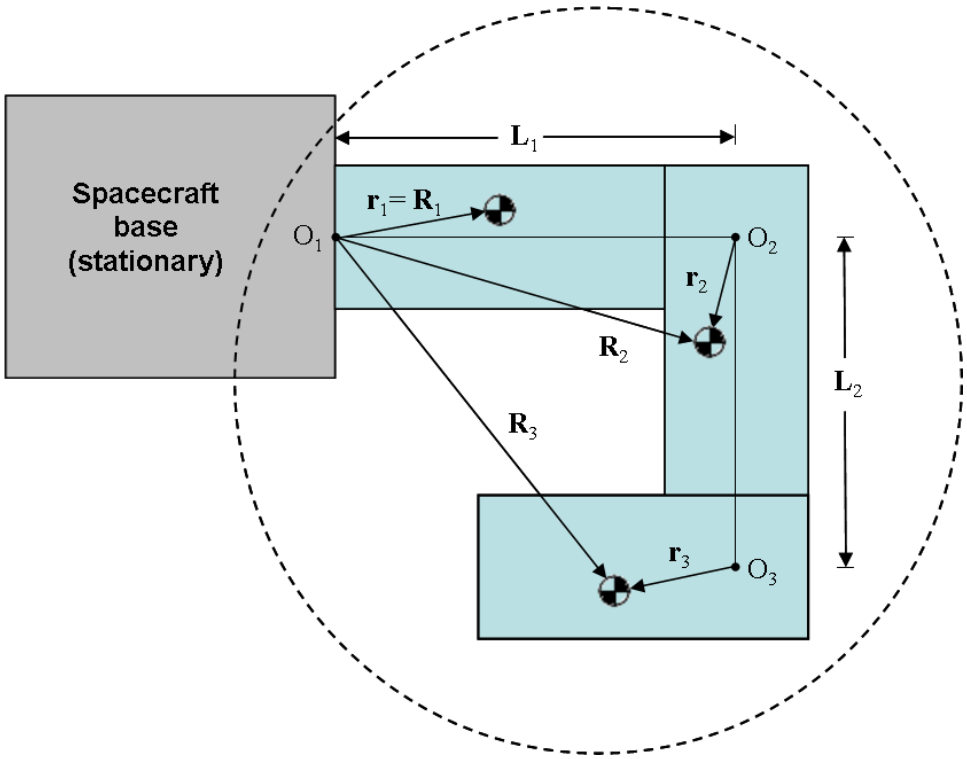

Figure 2.6: Reference configuration for the general three-body robotic payload attached to a stationary spacecraft base.

$$\begin{aligned}\mathbf{H}_1 \;=\; & \mathbf{I}_{1\mathrm{C}} \cdot \boldsymbol{\omega}^{1/0} + \mathbf{R}_1 \times m_{1\mathrm{C}} \left(\boldsymbol{\omega}^{1/0} \times \mathbf{R}_1\right) \\ & + \left(\mathbf{I}_{\mathrm{G}_1} + \mathbf{I}_{\mathrm{R}_1}\right) \cdot \boldsymbol{\omega}^{\mathrm{G}_1/1} + \left(\mathbf{I}_{\mathrm{G}_2} + \mathbf{I}_{\mathrm{R}_2}\right) \cdot \boldsymbol{\omega}^{\mathrm{G}_2/1} \\ & + \mathbf{I}_{\mathrm{R}_1} \cdot \left(\boldsymbol{\omega}^{\mathrm{R}_1/\mathrm{G}_1} + \boldsymbol{\omega}^{\mathrm{G}_1/1}\right) + \mathbf{I}_{\mathrm{R}_2} \cdot \left(\boldsymbol{\omega}^{\mathrm{R}_2/\mathrm{G}_2} + \boldsymbol{\omega}^{\mathrm{G}_2/1}\right). \end{aligned} \tag{2.10}$$

Since the CMGs in a scissored pair are identical, we let $\mathbf{I}_{\mathrm{R}_1} = \mathbf{I}_{\mathrm{R}_2} = \mathbf{I}_{\mathrm{R}}$ and $\mathbf{I}_{\mathrm{G}_1} = \mathbf{I}_{\mathrm{G}_2} = \mathbf{I}_{\mathrm{G}}$. Also, the gimbal angular velocities of these CMGs are equal in magnitude but opposite in direction, i.e., $\boldsymbol{\omega}^{\mathrm{G}_1/1} = -\boldsymbol{\omega}^{\mathrm{G}_2/1}$. Therefore, Eq. (2.10) simplifies to

$$\mathbf{H}_1 = \mathbf{I}_{1\mathrm{C}} \cdot \boldsymbol{\omega}^{1/0} + \mathbf{R}_1 \times m_{1\mathrm{C}} \left(\boldsymbol{\omega}^{1/0} \times \mathbf{R}_1\right) + \mathbf{I}_{\mathrm{R}} \cdot \boldsymbol{\omega}^{\mathrm{R}_1/\mathrm{G}_1} + \mathbf{I}_{\mathrm{R}} \cdot \boldsymbol{\omega}^{\mathrm{R}_2/\mathrm{G}_2}. \tag{2.11}$$

The angular momentum of the scissored pair is given by the last two terms. The rotor angular-momentum vectors are defined, $\mathbf{h}_1 = \mathbf{I}_{\mathrm{R}} \cdot \boldsymbol{\omega}^{\mathrm{R}_1/\mathrm{G}_1}$ and $\mathbf{h}_2 = \mathbf{I}_{\mathrm{R}} \cdot \boldsymbol{\omega}^{\mathrm{R}_2/\mathrm{G}_2}$, and Fig. 2.2 suggests that the rotor angular momentum for a CMG can be rewritten in terms of a scalar magnitude and some simple trigonometric expressions. Also, noting that the rotor angular-momentum vectors are equal in magnitude, or $|\mathbf{h}_1| = |\mathbf{h}_2| = h_1$, the system angular momentum simplifies to

$$\mathbf{H}_1 = \mathbf{I}_{1\mathrm{C}} \cdot \boldsymbol{\omega}^{1/0} + \mathbf{R}_1 \times m_{1\mathrm{C}} \left(\boldsymbol{\omega}^{1/0} \times \mathbf{R}_1 \right) + 2h_1 \cos\phi_1 \hat{\mathbf{e}}_{11}. \tag{2.12}$$

where ϕ_1 is the angular distance of $\mathbf{h}_1$ and $\mathbf{h}_2$ from the joint axis. The torque on the system is the derivative of the system angular momentum in an inertial frame, 0:

$$\begin{aligned} \frac{{}^0d}{dt}\mathbf{H}_1 \;=\; & \mathbf{I}_{1\mathrm{C}} \cdot \frac{{}^1d}{dt}\boldsymbol{\omega}^{1/0} + \boldsymbol{\omega}^{1/0} \times \left(\mathbf{I}_{1\mathrm{C}} \cdot \boldsymbol{\omega}^{1/0} \right) + \mathbf{R}_1 \times m_{1\mathrm{C}} \frac{{}^0d}{dt} \left(\boldsymbol{\omega}^{1/0} \times \mathbf{R}_1 \right) \\ & -2h_1\dot{\phi}_1 \sin\phi_1 \hat{\mathbf{e}}_{11}. \end{aligned} \tag{2.13}$$

The negative sign before the last term in Eq. (2.13) reflects the fact that the torque exerted on the body is a reaction to the gimbal torque imparted by the CMG.

Our analysis thus far can be generalized to a payload consisting of N linked bodies. If all bodies are assumed to conform to the assumptions in the single-body analysis, the torque and angular-momentum expressions for each link in the N-body system are similar to Eq. (2.12). The angular momentum of the N-body system about the base contact O_1 is

$$\mathbf{H} = \sum_{i=1}^{N} \mathbf{H}_i = \sum_{i=1}^{N} \Big(\mathbf{I}_{i\mathrm{C}} \cdot \boldsymbol{\omega}^{i/0} + \mathbf{R}_i \times m_{i\mathrm{C}} \mathbf{V}_i + 2h_i \cos\phi_i \hat{\mathbf{e}}_{i1} \Big), \tag{2.14}$$

where $\mathbf{H}_i$ is the angular momentum of the composite body i about the fixed point O_1 in Fig. 2.6. $\mathbf{I}_{i\mathrm{C}}$ is the composite inertia dyadic about the mass center for the ith arm segment-CMG scissored pair combination with total mass, $m_{i\mathrm{C}}$. The time derivative of Eq. (2.14) yields the total torque on a system with N rotational joints

$$\begin{aligned} \frac{{}^0d}{dt}\mathbf{H} \;=\; \sum_{i=1}^{N} \frac{{}^0d}{dt}\mathbf{H}_i = \sum_{i=1}^{N} \Big[& \mathbf{I}_{i\mathrm{C}} \cdot \frac{{}^id}{dt}\boldsymbol{\omega}^{i/0} + \boldsymbol{\omega}^{i/0} \times \big(\mathbf{I}_{i\mathrm{C}} \cdot \boldsymbol{\omega}^{i/0} \big) + \mathbf{R}_i \times m_{i\mathrm{C}} \mathbf{A}_i \\ & + 2h_i \big(-\dot{\phi}_i \sin\phi_i \hat{\mathbf{e}}_{i1} + \boldsymbol{\omega}^{i/0} \times \cos\phi_i \hat{\mathbf{e}}_{i1} \big) \Big]. \end{aligned} \tag{2.15}$$

The first term in Eq. (2.15) is the torque on the composite body due to the angular acceleration of the ith arm segment about O_1. The second term is the gyroscopic torque due to the change in direction of the composite body angular-momentum vector in an inertial frame. The third term represents the torque due to the force on body i's mass center acting at a distance from O_1. The last two terms in Eq. (2.15) are the torques on the system due to the change in direction of the ith scissored pair's rotor angular-momentum vectors. The first of these terms represents the torque that results from changing the direction of the rotor angular-momentum vectors with the CMG gimbals. The second of these terms results from changing the direction of these vectors with the motion of the inboard bodies.

For the more general case in which the spacecraft base is free-flying, $\mathcal{N}$ refers to the inertial frame, 0 refers to the frame fixed in the moving base, and the system torque about $\mathrm{O}_{\mathcal{N}}$ is

$$
\begin{aligned}
\frac{^{\mathcal{N}}d}{dt}\mathbf{H} &= \mathbf{H}_0 + \sum_{i=1}^{N} \frac{^{\mathcal{N}}d}{dt}\mathbf{H}_i \\
&= \mathbf{I}_0 \cdot \frac{^{0}d}{dt}\boldsymbol{\omega}^{0/\mathcal{N}} + \boldsymbol{\omega}^{0/\mathcal{N}} \times \left(\mathbf{I}_0 \cdot \boldsymbol{\omega}^{0/\mathcal{N}}\right) + \mathbf{R}_0 \times m_0 \mathbf{A}_0 \\
&\quad + \sum_{i=1}^{N} \Bigg[\mathbf{I}_{i\mathrm{C}} \cdot \frac{^{i}d}{dt}\boldsymbol{\omega}^{i/\mathcal{N}} + \boldsymbol{\omega}^{i/\mathcal{N}} \times \left(\mathbf{I}_{i\mathrm{C}} \cdot \boldsymbol{\omega}^{i/\mathcal{N}}\right) + \mathbf{R}_i \times m_{i\mathrm{C}} \mathbf{A}_i \\
&\quad + 2h_i\big(-\dot{\phi}_i \sin\phi_i \hat{\mathbf{e}}_{i1} + \boldsymbol{\omega}^{i/\mathcal{N}} \times \cos\phi_i \hat{\mathbf{e}}_{i1}\big) \Bigg], \qquad (2.16)
\end{aligned}
$$

where the system includes the spacecraft base and the N-link robotic payload. In Eq. (2.16), $\mathbf{H}_0$ is the angular momentum of the base about $\mathrm{O}_{\mathcal{N}}$, m_0 is the mass of the base, and $\mathbf{I}_0$ is the inertia dyadic of the base about its mass center. However, since our objective is to design a low-jitter spacecraft with a precision optical payload, we consider only the case in which the base is fixed in an inertial frame. This assumption is also reasonable for the likely case in which the base is much more massive than the robotic payload, as well as the case in which attitude and position control systems maintain six-degree-of-freedom fixity of the base. For these reasons, all further analysis in this dissertation considers N-link, N-degree-of-freedom systems in which the spacecraft base is inertially fixed, as shown in Figure 2.6.

With Eq. (2.15) and the general kinematics in Eqs. (2.6)-(2.8) where $\boldsymbol{\omega}^{0/\mathcal{N}}$, $\mathbf{R}_0$, $\mathbf{V}_0$, $\mathbf{A}_0$ are each equal to $\mathbf{0}$, the method of virtual power is used to extract the equations of motion. The principle of virtual power states that the sum of all generalized inertia torques and generalized active, or applied, torques in a system must be equal to zero in an inertial frame. This principle is a specific case of Kane's method, where the generalized speeds, u_j, described in [82, 83] are equal to the generalized velocities, $\dot{q}_j$. This method is used to derive a compact, vector-dyadic formulation of the equations of motion that is independent of basis. The

method of virtual power avoids the tedious computations associated with the Lagrangian approach [84], including the development and subsequent differentiation of the system energy. This method also circumvents the computation and subsequent elimination of internal forces and torques associated with the Newton-Euler approach [85]. The general equations of motion, as presented by Moon in [86], are

$$\sum_{i=1}^{N}\left[\left(m_{i\mathrm{C}}\mathbf{A}_i-\mathbf{F}_i^a\right)\cdot\frac{\partial\mathbf{V}_i}{\partial\dot{q}_j}+\left(\frac{{}^0d}{dt}\mathbf{H}_{ci}-\mathbf{M}_{ci}^a\right)\cdot\frac{\partial\boldsymbol{\omega}_i}{\partial\dot{q}_j}\right]=0, \tag{2.17}$$

where $\mathbf{H}_{ci}$ is the angular momentum of the ith composite body about its mass center, $\mathbf{F}_i^a$ is the total active force on composite body i, and $\mathbf{M}_{ci}^a$ is the total active moment about the ith composite body's mass center. To find the partial velocity and partial angular-velocity Jacobians in Eq. (2.17), we first choose the generalized coordinates and generalized velocities for this problem. Each generalized coordinate is the angular position of a body relative to its neighboring inboard body, $q_j=\theta_j$, and the generalized velocities are the time derivatives of the generalized coordinates, $\dot{q}_j=\dot{\theta}_j$. In a general system, the number of masses does not necessarily equal the number of degrees of freedom. However, in this case, there is a degree of freedom for each body. The angular velocity of each body relative to an inertial frame is written in terms of the generalized velocities,

$$\boldsymbol{\omega}_i=\boldsymbol{\omega}^{i/0}=\sum_{i=1}^{N}\dot{q}_i\hat{\mathbf{e}}_{i1}. \tag{2.18}$$

The inertial velocity of each body is given by Eq. (3.2). Differentiating $\mathbf{V}_i$ and $\boldsymbol{\omega}_i$ with respect to the generalized velocities, we find the partial velocity and partial angular-velocity Jacobians, respectively. With the reference configuration in Fig. 2.6, these Jacobians are

$$\frac{\partial \mathbf{V}_i}{\partial \dot{q}_j} = \begin{cases} \hat{\mathbf{e}}_{j1} \times \left[\sum_{k=j}^{i-1} (\mathbf{L}_k) + \mathbf{r}_i \right] & i > j \\ \hat{\mathbf{e}}_{j1} \times \mathbf{r}_i & i = j \\ 0 & i < j \end{cases} \tag{2.19}$$

$$\frac{\partial \boldsymbol{\omega}_i}{\partial \dot{q}_j} = \begin{cases} \hat{\mathbf{e}}_{j1} & i \geq j \\ 0 & i < j \end{cases} \tag{2.20}$$

Although the system of interest in this dissertation has an inertially fixed base, Kane's method can also be used to derive dynamical equations for the system with a free-flying base. For the moving-base system shown in Fig. 2.5, there are six additional generalized speeds associated with the base degrees of freedom. While this system is not modeled for our work, Roithmayr *et al.* [87] discuss the approach for incorporating base dynamics into the equations of motion using Kane's method.

Since minimizing base reactions is an important design goal for an imaging payload, we consider a special case where the base is stationary and where the total inertia dyadic of the payload is constant in an inertial frame. A stationary base implies that 1) attitude dynamics of the spacecraft do not enter into the equations of motion, and 2) that the payload mass center does not translate during body rotations. If the payload mass center translates during a maneuver, there would be a force acting between the innermost body and the base. This reaction force may then cause an additional moment if its line of action is at a distance from the system mass center. With a total inertia dyadic that is constant in 0 during body rotations, the reaction torque on the base is also avoided. Finally, there are constraint forces and torques acting between each body, but they do not contribute to the generalized active torques and forces, and therefore do not appear in the equations of motion. If there is a frictionless contact between the base and payload,

then there are only internal torques acting on the system. Equation (2.17) then becomes

$$\sum_{i=1}^{N}\left(\frac{{}^{0}d}{dt}\mathbf{H}_{ci}\cdot\frac{\partial\boldsymbol{\omega}_i}{\partial\dot{q}_j}\right)=0. \tag{2.21}$$

In the case where the total inertia dyadic of the payload about its mass center is not constant in 0, there would be a gyroscopic torque imparted to the base due to the motion of each composite body whose inertia dyadic varies in 0. Implementing the proposed reactionless configuration places some straightforward constraints on the bodies. First, to eliminate reaction forces, the center of mass of the ith body and its outboard neighbors must be located on the ith joint axis. Such a goal would be readily achieved with proper placement of components or, in the worst case, with ballast. A payload inertia dyadic that is constant in 0 requires merely that no admissible motion of the linked bodies causes a change in their composite inertia dyadic. Furthermore, the joint axis of each body must be one of its principal axes. A simple example is a solid cylinder to which a spherical outer body is mounted. Certain combinations of nested solid spheres and cylinders also meet this requirement. In practice, the bodies would not be solid. It is only the inertia dyadic of the bodies that would have to exhibit this sort of symmetry. Again, ballast might be used as a last resort to enforce this condition. While these assumptions may not be perfectly realized in a real-world spacecraft, they are sensible objectives in the design of a precise, agile imaging payload. A constant-inertia, reactionless system is studied here because the previously-described complexities that arise from having a time-varying inertia dyadic obscure insight into the problem and will not change the fundamental results of the CMG/RWA comparison.

In order to examine the power consumption of this N-body CMG system, its

total energy is first derived:

$$E = = \frac{1}{2}\sum_{i=1}^{N}\Bigg\{(\boldsymbol{\omega}^{i/0}\cdot\mathbf{I}_i\cdot\boldsymbol{\omega}^{i/0}) + \sum_{j=1}^{S}\Big[(\boldsymbol{\omega}^{\mathrm{G}_{ij}/0}\cdot\mathbf{I}_{\mathrm{G}_{ij}}\cdot\boldsymbol{\omega}^{\mathrm{G}_{ij}/0}) + (\boldsymbol{\omega}^{\mathrm{R}_{ij}/0}\cdot\mathbf{I}_{\mathrm{R}_{ij}}\cdot\boldsymbol{\omega}^{\mathrm{R}_{ij}/0})\Big]\Bigg\}, \tag{2.22}$$

where S is the number of CMGs on each body and $\mathbf{I}_i$ is the central inertia dyadic of the ith arm segment without the CMGs. $\mathbf{I}_{\mathrm{G}_{ij}}$ is the central inertia dyadic of the jth CMG gimbal on body i and $\mathbf{I}_{\mathrm{R}_{ij}}$ is the central inertia dyadic of the jth CMG rotor on body i. As before, G_{ij} and R_{ij} represent the jth gimbal-fixed frame on body i and the jth rotor-fixed frame on body i, respectively.

With a symmetric inertia dyadic for each system component, the time derivative of Eq. (2.22) yields the system power:

$$P = \sum_{i=1}^{N}\Bigg\{\left(\frac{^{i}d}{dt}\boldsymbol{\omega}^{i/0}\cdot\mathbf{I}_i\cdot\boldsymbol{\omega}^{i/0}\right) + \sum_{j=1}^{S}\Bigg[\left(\frac{^{\mathrm{G}_{ij}}d}{dt}\boldsymbol{\omega}^{\mathrm{G}_{ij}/0}\cdot\mathbf{I}_{\mathrm{G}_{ij}}\cdot\boldsymbol{\omega}^{\mathrm{G}_{ij}/0}\right) + \left(\frac{^{\mathrm{R}_{ij}}d}{dt}\boldsymbol{\omega}^{\mathrm{R}_{ij}/0}\cdot\mathbf{I}_{\mathrm{R}_{ij}}\cdot\boldsymbol{\omega}^{\mathrm{R}_{ij}/0}\right)\Bigg]\Bigg\}. \tag{2.23}$$

Again, since the CMGs in a scissored pair are identical, Eq. (2.22) and Eq. (2.23) can be further simplified by letting $\mathbf{I}_{\mathrm{R}_{i1}} = \mathbf{I}_{\mathrm{R}_{i2}} = \mathbf{I}_{\mathrm{R}}$ and $\mathbf{I}_{\mathrm{G}_{i1}} = \mathbf{I}_{\mathrm{G}_{i2}} = \mathbf{I}_{\mathrm{G}}$. Also, since negative values of power indicate energy extracted from the motion of the connected components, we compute the absolute value of power for each component

to reflect the fact that energy is probably not regeneratively recovered through back-electromotive force (EMF) in the gimbal motors. This loss represents friction in the motors and I^2R dissipation due to heat created by current and resistance.

It has been shown in [88] that there is a significant amount of power devoted to maintaining a constant CMG rotor speed in a control loop. However, with low-bandwidth control of the rotor motors that allows very small changes in the rotor speed, the rotor accelerations have negligible effects on the system power. In this chapter, as well as in Chapter 3, we consider the case in which a high-bandwidth controller keeps each rotor spinning at a constant speed. The conclusions in these chapters remain valid, however, since implementing low-bandwidth rotor control would merely offset the power consumption results by the amount associated with enforcing the constant-speed constraint on the rotors. Chapter 4 examines the alternative case in which the power due to maintaining constant-speed rotors is negligible.

2.4 Simulation Results

Numerical results in this section demonstrate the advantages of the proposed system over an analogous system that uses RWAs for momentum exchange. The objective is to show that the power required to steer the CMG-based system is significantly less than that required for the RWA-based system. We focus on a system that includes only three bodies. In addition, we consider a particular case in which the mass centers of the three bodies coincide and where the diagonal inertia matrix of each segment has three identical moments of inertia. Again, while this system is not the most general, it leads to relevant conclusions without obscuring

the results with a large number of complicated terms.

2.4.1 CMG-Based System

For the particular case under consideration that was detailed in the previous section, Eq. (2.21) is expanded into equations of motion for a three-body, CMG-based system:

$$\begin{bmatrix} I_{1\mathrm{C}} + I_{2\mathrm{C}} + I_{3\mathrm{C}} & 0 & -I_{3\mathrm{C}}\cos\theta_2 \\ 0 & I_{2\mathrm{C}} + I_{3\mathrm{C}} & 0 \\ -I_{3\mathrm{C}}\cos\theta_2 & 0 & I_{3\mathrm{C}} \end{bmatrix} \begin{bmatrix} \ddot{\theta}_1 \\ \ddot{\theta}_2 \\ \ddot{\theta}_3 \end{bmatrix} = \\ \begin{bmatrix} 2h_1\dot{\phi}_1\sin\phi_1 - 2h_3\dot{\phi}_3\sin\phi_3\cos\theta_2 - 2h_3\dot{\theta}_2\cos\phi_3\sin\theta_2 - I_{3\mathrm{C}}\dot{\theta}_2\dot{\theta}_3\sin\theta_2 \\ 2h_2\dot{\phi}_2\sin\phi_2 + 2h_3\dot{\theta}_1\cos\phi_3\sin\theta_2 + I_{3\mathrm{C}}\dot{\theta}_1\dot{\theta}_3\sin\theta_2 \\ 2h_3\dot{\phi}_3\sin\phi_3 - I_{3\mathrm{C}}\dot{\theta}_1\dot{\theta}_2\sin\theta_2 \end{bmatrix}. \quad (2.24)$$

In Eq. (2.24), $I_{i\mathrm{C}}$ is one of the three identical, diagonal elements of the inertia matrix, $\mathbf{I}_{i\mathrm{C}}$. Representing the CMG as a uniform, i.e., spherical, mass distribution is a good approximation, both because CMGs resemble spheres by design [89] and because asymmetries and products of inertia would be avoided in an application where such disturbances could degrade performance. In these simulations, the initial body angles are arbitrary but equal for each body and the initial body rates are zero. Also, the CMG gimbal kinematics are prescribed and used as open-loop control inputs. These kinematics are chosen such that the arm segments rotate at speeds up to several radians per second, which is orders of magnitude more agile than bus-steered spacecraft payloads [90]. Consistent with the definition of a scissored pair, each CMG in a pair has equal-magnitude gimbal angles, rates, and

accelerations. It is also assumed that for this maneuver, the gimbals begin and end their motion at gimbal angles where the net angular momentum of each scissored pair is zero: the rotor angular-momentum vectors are π radians apart from each other and are both perpendicular to the joint axis. Therefore, the system begins and ends this motion at rest. Gimbal angles are measured from the joint axis, as shown in Fig. 2.2. The gimbal histories implemented in this simulation depend on an initial time given by t_0 and a final time given by $t_f = t_0 + T$, where T is the duration of the slew maneuver. These gimbal histories are prescribed according to

$$\phi_i(t) = \begin{cases} -\frac{\pi}{2} & t < t_0 \\ -\frac{\pi}{2} + \frac{\alpha_i}{2}\left[1 - \cos\left(\frac{2\pi(t-t_0)}{T}\right)\right] & t_0 < t < t_f \\ -\frac{\pi}{2} & t > t_f \end{cases} \tag{2.25}$$

In Eq. (2.25), the coefficients α_i set the allowed range of gimbal motion. Prescribing this motion to the CMG scissored pairs results in a smooth motion of the bodies to which they are attached. An example of the CMG gimbal motion is illustrated in Fig. 2.7 with $\alpha_i = \pi/2$. This setting demands the maximum torque out of the scissored pair since the gimbal rotates from $\phi_i = -\pi/2$ to an intermediate gimbal angle $\phi_i = 0$ (maximum angular momentum transferred to the body), and then back to $\phi_i = -\pi/2$.

2.4.2 RWA-Based System

To facilitate comparisons, the RWA-based system has identical mass properties to the CMG system. Therefore, there are two RWAs fixed to each body with their rotor angular-momentum vectors on the body's joint axis. With the same analysis

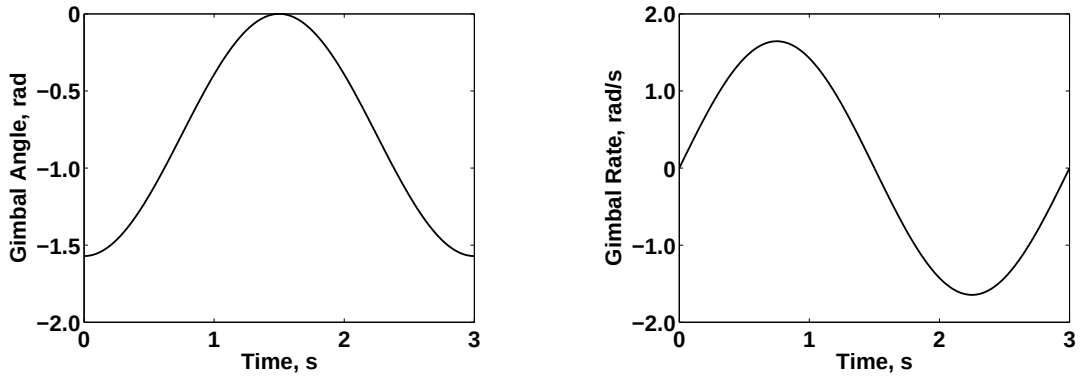

(a) Gimbal angle vs. time.

(b) Gimbal rate vs. time.

Figure 2.7: Example of prescribed gimbal kinematics.

methods that were used in the CMG case, the equations of motion are derived for the RWA system:

$$\begin{bmatrix} I_{1\mathrm{C}} + I_{2\mathrm{C}} + I_{3\mathrm{C}} & 0 & -I_{3\mathrm{C}} \cos\theta_2 \\ 0 & I_{2\mathrm{C}} + I_{3\mathrm{C}} & 0 \\ -I_{3\mathrm{C}} \cos\theta_2 & 0 & I_{3\mathrm{C}} \end{bmatrix} \begin{bmatrix} \ddot{\theta}_1 \\ \ddot{\theta}_2 \\ \ddot{\theta}_3 \end{bmatrix} = \begin{bmatrix} -2I_{\mathrm{R}}\dot{\Omega}_1 + 2I_{\mathrm{R}}\dot{\Omega}_3 \cos\theta_2 - 2I_{\mathrm{R}}\dot{\theta}_2\Omega_3 \sin\theta_2 - I_{3\mathrm{C}}\dot{\theta}_2\dot{\theta}_3 \sin\theta_2 \\ -2I_{\mathrm{R}}\dot{\Omega}_2 + 2I_{\mathrm{R}}\dot{\theta}_1\Omega_3 \sin\theta_2 + I_{3\mathrm{C}}\dot{\theta}_1\dot{\theta}_3 \sin\theta_2 \\ -2I_{\mathrm{R}}\dot{\Omega}_3 + I_{3\mathrm{C}}\dot{\theta}_1\dot{\theta}_2 \sin\theta_2 \end{bmatrix}. \quad (2.26)$$

In Eq. (2.26), the scalar I_{R} refers to the identical, diagonal elements of the inertia matrix, $\mathbf{I}_{\mathrm{R}}$ [91]. In the CMG system, the gimbal motion is prescribed with smooth sinusoidal curves. To construct an RWA system with the same kinematics, the rotor spin rate is prescribed such that the angular momentum of the RWA rotors is identical to that of the CMGs. The magnitude of the RWA angular-momentum vector is

$$h_{\mathrm{RWA}_i} = I_{\mathrm{R}}\Omega_i, \tag{2.27}$$

where Ω_i is the rotor spin rate of either RWA on body i. Equating the net angular-momentum magnitudes for the two systems yields RWA spin rates that are zero at t_0 and t_f.

With these modifications, the expressions for energy and power of the RWA system are derived in exactly the same manner as the CMG system. In the following section, these expressions will be used to compare the power consumption of both systems for prescribed open-loop behavior of the actuators.

2.4.3 CMG and RWA System Comparison

Monte-Carlo simulations are used to determine how the random variation of certain parameters affects system performance [92]. Besides the duration of the slew, several parameters greatly influence the system's power consumption including the composite body inertia, range of gimbal motion, and the initial relative body angles. A Monte-Carlo simulation over these parameters helps to determine regimes in which a CMG system offers the greatest benefits over its RWA counterpart. All simulation results in this section, as well as in the rest of this dissertation, are obtained with MATLAB®. A set of random numbers for each parameter is generated from a uniform probability distribution over the intervals in Table 2.1 using the function **rand.m**. These random parameter values are assumed to be equal for each body. Other constants of the motion are listed in Table 2.2. The angular-momentum magnitude of each CMG rotor is based on that of an existing device, the Honeywell M50 CMG [17]. In this dissertation, we consider only cases

in which the joint, gimbal, and rotor bearings are frictionless, since the effects due to friction are never well known and are consequently difficult to model. The function **ode45.m** is used to integrate the equations of motion in Eqs. (2.24) and (2.26) from initial time $t_0 = 0$ s to final time $t_f = 3$ s for 1000 runs.

Table 2.1: Intervals for Uncertain Parameters in the CMG/RWA Comparison Study.

Parameter	Interval
Composite Body Inertia, $I_{i\mathrm{C}}$	[10, 200] kg-m^2
Motion coefficient, α_i	$[\frac{\pi}{4}, \pi]$ rad
Initial relative body angle, $\theta_i(t_0)$	$[0, \pi]$ rad

Table 2.2: Open-Loop Simulation Parameters in the CMG/RWA Comparison Study.

Parameter	Interval
Initial relative body rates, $\dot{\theta}_i(t_0)$	(0, 0, 0) rad/s
CMG rotor angular momentum, h_i	50 N-m-s
CMG rotor spin speed	200 rad/s
Rotor inertia, I_{R}	0.25 kg-m^2
Gimbal inertia, I_{G}	0.125 kg-m^2

Finding regimes in which the CMG system maximally outperforms the RWA system requires choosing a performance metric. This analysis uses the ratio of maximum power magnitude of the RWA system to that of the CMG system, with larger values corresponding to greater benefits provided by the CMG system. To find the magnitude of the system's power consumption, we differentiate the energy

of each system component, compute the absolute value for each component, and sum these terms. For a given slew duration, an optimal combination of system parameters is the one that maximizes the aforementioned ratio within the previously specified intervals. This optimal combination of parameters for a three-second maneuver is reported in Table 2.3 below. The time-domain dynamics are shown in the plots of Fig. 2.8. Since the CMG and RWA systems undergo identical motions, only one set of plots for the relative body angles and rates is shown. Figure 2.8 shows that the maximum power needed to operate the RWA system exceeds that of the CMG system by at least two orders of magnitude. In fact, the peak power input of the CMG system is about 245 W while the RWA system demands an astonishing 53 kW. This vast difference is attributed to the fact that the power required by the RWA system scales with the high RWA rotor speeds while the CMG system requires power only for torquing the gimbal motors.

Table 2.3: Simulation Parameters That Maximize the Performance Metric in the CMG/RWA Comparison Study.

Parameter	Value
Composite Body Inertia, $I_{i\mathrm{C}}$	199.72 kg-m^2
Motion coefficient, α_i	1.38 rad
Initial relative body angle, $\theta_i(t_0)$	1.69 rad

Table 2.3 suggests that the composite body inertia dominates the comparative performance of the two systems. In another set of simulations, we perform 1000 runs of a three-second slew from $t_0 = 0$ s to $t_f = 3$ s with the composite body inertia randomly drawn from a uniform distribution on the interval [10, 200] kg-m^2. In each realization of this maneuver, the composite body inertia is the same

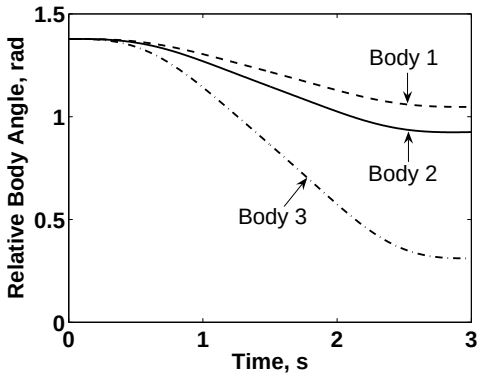

(a) Relative body angle vs. time.

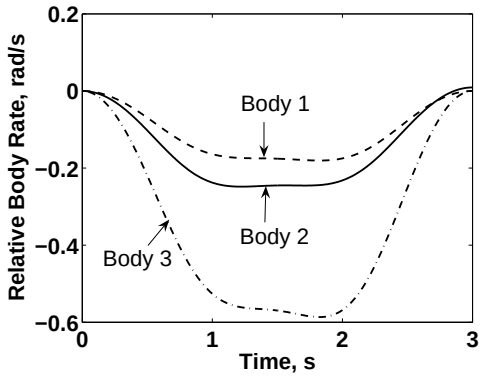

(b) Relative body rate vs. time.

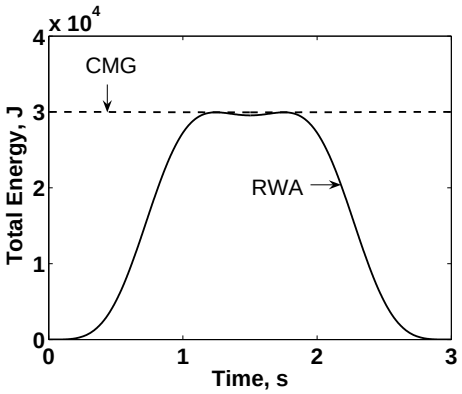

(c) Total energy vs. time.

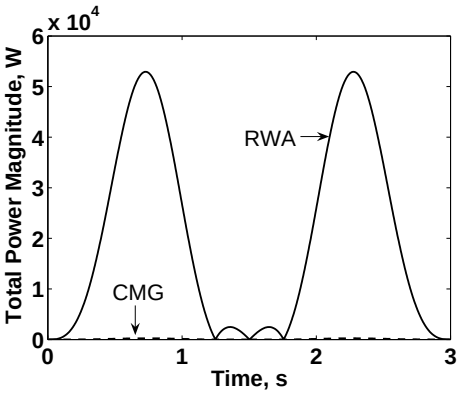

(d) Total power magnitude vs. time.

Figure 2.8: Time-domain dynamics of the realization maximizing the performance metric.

for each of the three bodies. The initial relative body angles are each set to 0 rad and the motion coefficients, α_i, are each set to $\pi/2$ rad. The same constants from Table 2.2 are used in this simulation. The relationship between the maximum power input and joint kinematics is shown in Figs. 2.9 - 2.11. For the same set of simulations, the plots in Fig. 2.12 demonstrate the effect of varying composite body inertia on the power input required for the maneuver.

This Monte-Carlo analysis shows that the low-power benefits of a CMG system

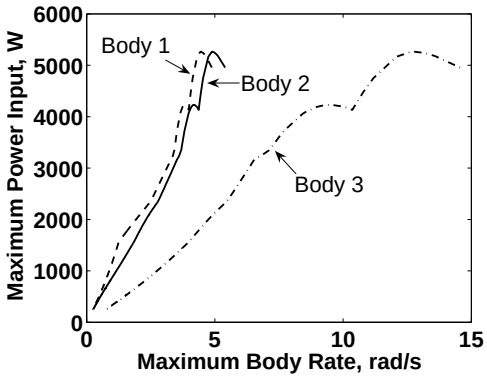

(a) CMG system.

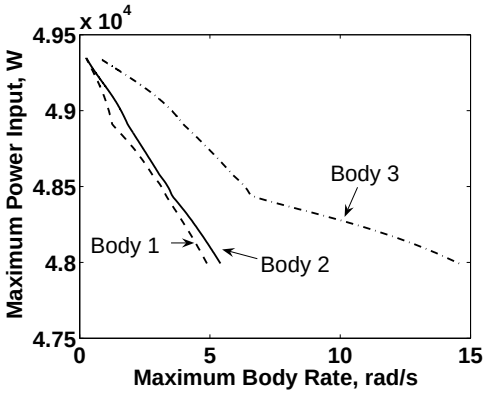

(b) RWA system.

Figure 2.9: Maximum power input vs. maximum body rate.

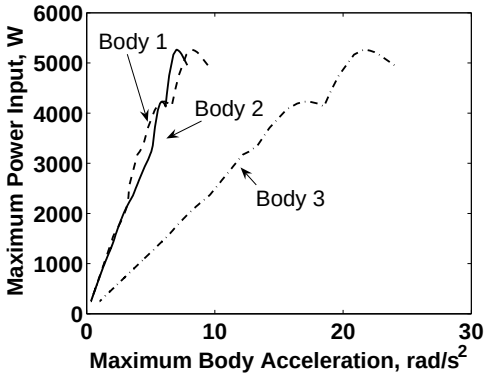

(a) CMG system.

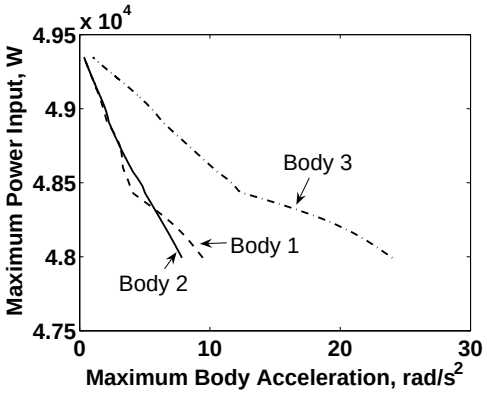

(b) RWA system.

Figure 2.10: Maximum power input vs. maximum body acceleration.

are increasingly pronounced with increasing composite body inertia. In fact, Fig. 2.12 shows that the maximum power ratio (RWA to CMG) is in approximately direct proportion to the composite body inertia. In the upper limit of inertia values, the arm segments are nearly stationary during the simulation. In that case, for the CMG system, the torque on the gimbal motors includes only the

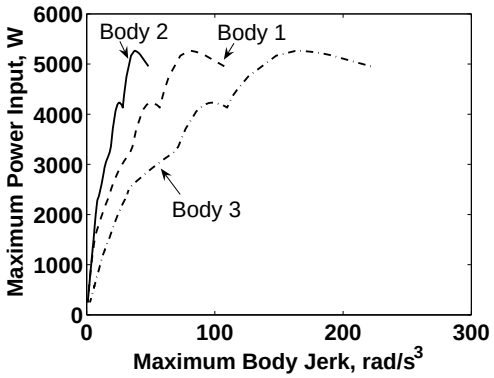

(a) CMG system.

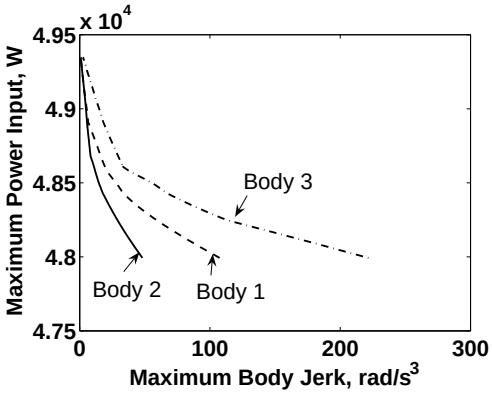

(b) RWA system.

Figure 2.11: Maximum power input vs. maximum body jerk.

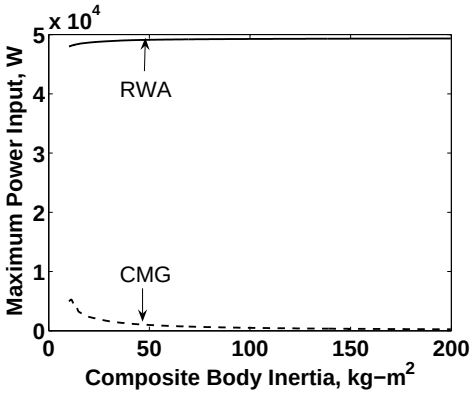

(a) Maximum power input vs. composite body inertia.

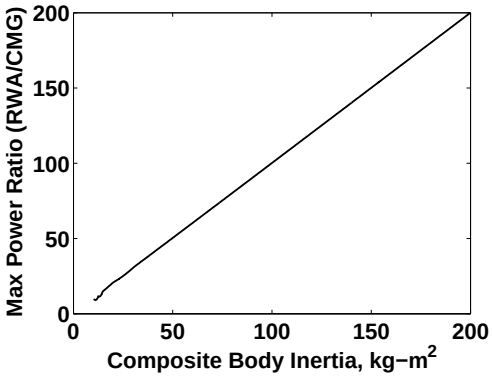

(b) Maximum power ratio (RWA/CMG) vs. composite body inertia.

Figure 2.12: Monte-Carlo results relating the system power to composite body inertia.

torque needed to accelerate the CMG. For the RWA system, the angular rates of the arm segments have little influence over the torque on the wheels because those rates are generally much lower than the wheel rates. In the lower limit of inertia values, the peak power of the CMG system is at a maximum. Since we

are using the same open-loop input for each simulation, bodies with lower inertia rotate faster. For the smallest inertia values, the high rotation rates of the arm segments can impart large gyroscopic torques back onto the gimbal motors. Since the gimbals must overcome this reaction torque in addition to completing their prescribed motion, more electrical power is required.

For our system, the gimbal torque magnitude of the jth CMG on body i is

$$\tau_{\mathrm{G}_{ij}} = \left[(\mathbf{I}_{\mathrm{R}} + \mathbf{I}_{\mathrm{G}}) \cdot \frac{^{\mathrm{G}_{ij}}d}{dt} \boldsymbol{\omega}^{\mathrm{G}_{ij}/0} \right] \cdot \hat{\mathbf{e}}_{i3}. \tag{2.28}$$

Figure 2.13 relates the maximum power input to the maximum value of the gimbal torque magnitude for every realization of the maneuver. The results show that the maximum gimbal torque magnitude for body 1 remains constant at a small value. The reason is evident in the total reaction torque on the body given by the last term in Eq. (2.13). Since the reaction torque due to the net change in angular momentum has a component only along the joint axis, there is no reaction generated in the gimbal axis direction, $\hat{\mathbf{e}}_{13}$. Therefore, the small value of maximum gimbal torque that remains constant for all values of maximum power input is only the torque needed to accelerate the gimbal.

To investigate the feasibility of RWA actuation in this agile system, the torque imparted by each RWA is

$$\tau_{\mathrm{R}_{ij}} = \left(\mathbf{I}_{\mathrm{R}} \cdot \frac{^{\mathrm{R}_{ij}}d}{dt} \boldsymbol{\omega}^{\mathrm{R}_{ij}/0} \right) \cdot \hat{\mathbf{e}}_{i1}. \tag{2.29}$$

The maximum torque applied to each body by one of its fixed wheels is shown in Fig. 2.14. For the candidate set of composite body inertia values and the chosen

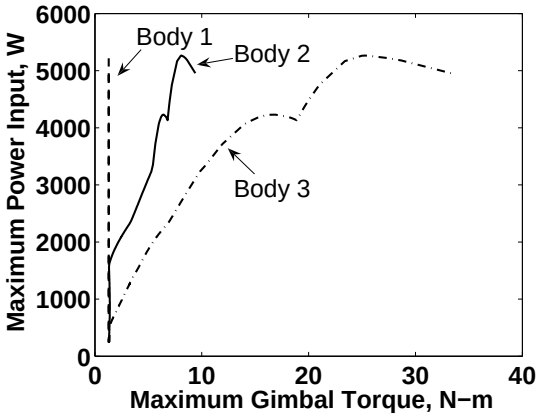

Figure 2.13: Maximum power input vs. maximum gimbal torque.

simulation parameters, each simulation calls for a peak RWA torque of around 65 N-m. However, the maximum output torque for the most powerful existing RWAs is 2 N-m [16]. To meet the agility requirements for this system, one could use much larger RWAs or fix more RWAs to each arm segment, but the added mass and resulting power requirement for such a system would be prohibitive and impractical.

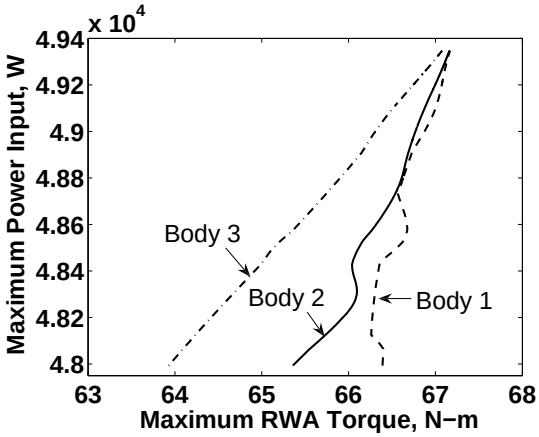

Figure 2.14: Maximum power input vs. maximum RWA torque.

2.5 Chapter Conclusions

This study demonstrates effective and relatively simple reactionless methods for actuating a multi-body system. Based on first-principles derivations, simulations have predicted that a CMG-actuated system is far more power-efficient for the payload's high-agility and low-power requirements. When compared to an RWA system executing an identical maneuver, the CMG system was shown to consume less than 1% of the power required to slew the RWA system. By varying the parameters that most greatly influence power consumption of the two systems, we found that CMGs maximally benefit the system in high-inertia regimes, where the torque imparted to the gimbal motors by the rotating arm segments is minimized. The relationship between the maximum power input and the system kinematics substantiates this claim and further demonstrates that achieving the same agility in both systems leads to very different power consumption. However, even in the best-case simulation for the RWA system, the output torque necessary to move the arm segments is not feasible with existing RWAs. With the fundamental dynamics established in this study, the remaining chapters will involve the study of closed-loop maneuvers, which will allow the estimation of energy expended given arbitrary system kinematics.

CHAPTER 3

REDUCING BASE REACTIONS OF A ROBOTIC SYSTEM WITH CMG ACTUATION

3.1 Introduction

Actuation solutions have been investigated as a means to achieve a reactionless system. Unlike external actuators such as reaction jets or direct-drive motors, internal momentum actuators can provide reactionless actuation of the robotic arm segments with a mass-balanced system design. Momentum-exchange devices include RWAs and CMGs. These devices apply torque by exchanging their angular momentum with the payload, maintaining a constant system angular momentum. It was shown in Chapter 2 that a CMG system can outperform an identical RWA system by orders of magnitude in power usage when the open-loop CMG gimbal kinematics are prescribed. The results also show that for arbitrary slews, the output torque needed for actuating an agile system is feasible only with CMGs.

This chapter investigates how the choice of operations concept and actuation method influences base reactions and power consumption when manipulating a payload in an arbitrary pick-and-place maneuver. We investigate how base reactions and power might be reduced for closed-loop motion of the joints. Section 3.2 defines the system kinematics. Section 3.3 provides a detailed dynamics analysis for single- and multi-body systems driven by CMGs, and Section 3.4 presents a feedback-linearization control design. A comparison study of actuation methods and operations concepts is performed in Section 3.5 for an example maneuver in which each joint angle tracks a step input. Base reactions for the CMG system are compared to an identical system driven by standard joint motors. Both base

reactions and power are compared for the CMG system using different operations concepts. The mass-balanced case is also examined in this comparison study. A Monte-Carlo analysis is performed to statistically evaluate the results for the general CMG and conventionally actuated systems. Reference [5] provides preliminary results for this work, specifically for power consumption.

3.2 System Description and Kinematics

To perform a general pick-and-place maneuver, the system must offer at least three degrees of freedom. As in Chapter 2, we consider a three-segment robotic arm interconnected with single-degree-of-freedom revolute joints where the joint axis of a given body is orthogonal to that of its inboard neighbor. Each arm segment is actuated by a single scissored pair of CMGs. This architecture is detailed in Section 2.2. Closed-chain parallel mechanisms may also be useful in this payload problem because of their high structural stiffness [93], but they are not considered here.

The same reference configuration corresponding to a stationary spacecraft base from Section 2.2 is used again for this study, but the system is shown to include an added payload. The general transformation from the body j-fixed coordinate system to the body-i-fixed coordinate system is given by Eq. (2.5). Reference frames are numbered, with 0 corresponding to the inertial frame and $1, 2, \ldots, N$ corresponding to the frames fixed in each arm segment from innermost to outermost. N is the number of degrees of freedom, which corresponds to the number of arm segments in the proposed system.

A representation of the end-effector kinematics provides the basis for controlling

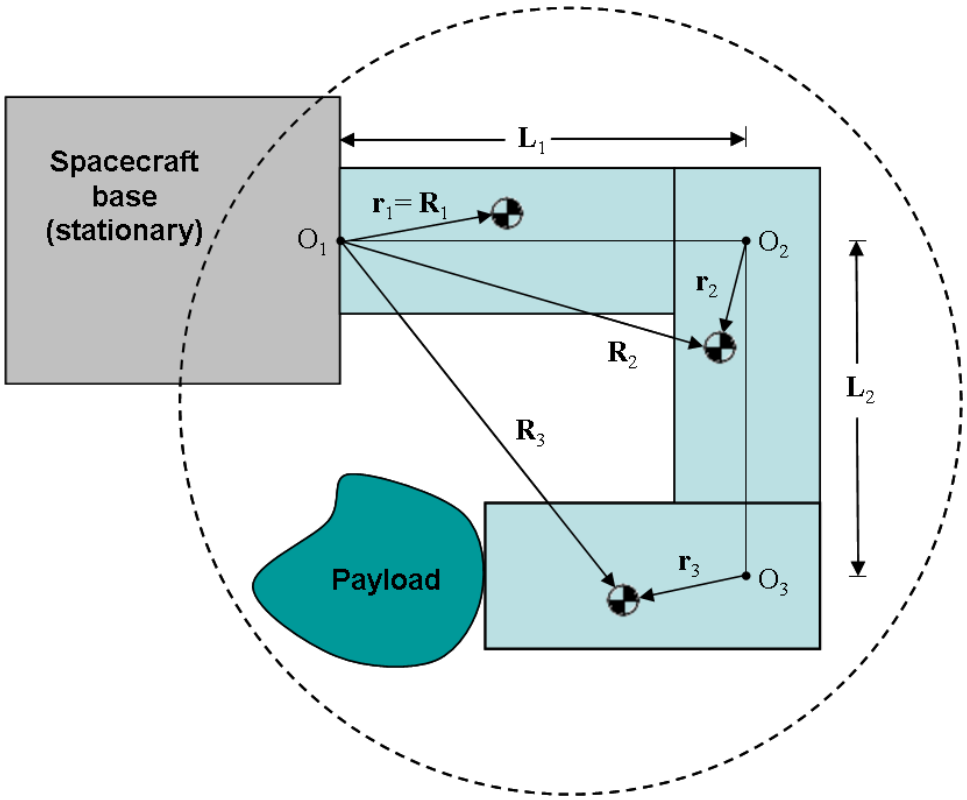

Figure 3.1: Reference configuration for a general three-body system with an added payload.

the end effector's motion along an arbitrary path. To establish this representation, Fig. 3.1 illustrates a three-body architecture for the robotic system that can be extended to an arbitrary number of bodies. With the exception of the added payload, this reference configuration is identical to Fig. 2.6 in Chapter 2. The position, velocity, and acceleration vectors for the mass center of an arbitrary body i, when measured from the base contact, O_1, are

$$\mathbf{R}_i = \sum_{j=1}^{i-1} \mathbf{L}_j + \mathbf{r}_i \ , \tag{3.1}$$

$$\mathbf{V}_i = \sum_{j=1}^{i-1} (\boldsymbol{\omega}^{j/0} \times \mathbf{L}_j) + \boldsymbol{\omega}^{i/0} \times \mathbf{r}_i \ , \tag{3.2}$$

$$\begin{aligned} \mathbf{A}_i = & \sum_{j=1}^{i-1} \left[\frac{^j d}{dt} \boldsymbol{\omega}^{j/0} \times \mathbf{L}_j + \boldsymbol{\omega}^{j/0} \times (\boldsymbol{\omega}^{j/0} \times \mathbf{L}_j) \right] \\ & + \frac{^i d}{dt} \boldsymbol{\omega}^{i/0} \times \mathbf{r}_i + \boldsymbol{\omega}^{i/0} \times (\boldsymbol{\omega}^{i/0} \times \mathbf{r}_i) \ , \end{aligned} \tag{3.3}$$

where $\boldsymbol{\omega}^{i/j}$ is the angular velocity of frame i relative to frame j and $^i d/dt$ is the time derivative in the i frame.

With these kinematic relationships, a payload trajectory command can be defined and converted into a corresponding sequence of commanded joint angles by applying the positional inverse kinematics. However, according to Eq. (3.1), an analytical solution certainly does not exist for the proposed system because of the nonlinear relationship between the end-effector and joint coordinates. Rather, the differential relationship between these quantities is used:

$$\delta^0 R_i = K(\theta_i) \delta\Theta, \tag{3.4}$$

where $\delta^0 R_i \in \mathbb{R}^{3\times 1}$ contains the differential end-effector position in inertial (0) coordinates, and $\delta\Theta \in \mathbb{R}^{N\times 1}$ contains the differential joint angles. The differential position Jacobian $K \in \mathbb{R}^{3\times N}$ relates these quantities.

Unlike the positional inverse kinematics problem, the velocity inverse kinematics problem has a straightforward analytical solution. The relation is given by

$$^0V_i = H(\theta_i)\dot{\Theta}, \tag{3.5}$$

where the velocity Jacobian $H \in \mathbb{R}^{3\times N}$ relates the joint rates, $\dot{\Theta} \in \mathbb{R}^{N\times 1}$, to the end-effector velocity in inertial coordinates, $^0V_i \in \mathbb{R}^{3\times 1}$. To find the elements of H, h_{ij}, ^0V_i is simply differentiated with respect to the joint rates:

$$h_{ij} = \frac{\partial^0 V_i}{\partial \dot{\theta}_j} \tag{3.6}$$

The Jacobians K and H can be used to compute the joint-angle and joint-rate errors for a controller that tracks an end-effector trajectory. However, we leave end-effector motion control to be examined in Chapter 4. The following analysis evaluates this system's performance while using direct joint-motion control.

3.3 System Dynamics

It was shown in Section 2.3 that the total angular momentum of N linked bodies with CMG scissored pairs is given by

$$\mathbf{H} = \sum_{i=1}^{N} \mathbf{H}_i = \sum_{i=1}^{N} \Big(\mathbf{I}_{i\mathrm{C}} \cdot \boldsymbol{\omega}^{i/0} + \mathbf{R}_i \times m_{i\mathrm{C}} \mathbf{V}_i + 2h_i \cos\phi_i \hat{\mathbf{e}}_{i1} \Big), \tag{2.14}$$

where $\mathbf{H}_i$ is the angular momentum of the composite body i about the fixed point O_1 in Fig. 3.1. $\mathbf{I}_{i\mathrm{C}}$ is the composite inertia dyadic about the mass center for the ith arm segment-CMG scissored pair combination with total mass, $m_{i\mathrm{C}}$. h_i is the magnitude of either rotor angular-momentum vector for the scissored pair fixed

to body i. ϕ_1 is the angular distance of $\mathbf{h}_1$ and $\mathbf{h}_2$ from the joint axis, and $\hat{\mathbf{e}}_{ij}$ represents the basis vector along the j direction in the coordinate system fixed to body i.

The total torque on this N-body system about O_1 is the derivative of the system angular momentum in an inertial frame:

$$\begin{aligned}\frac{^0d}{dt}\mathbf{H} \;=\; \sum_{i=1}^{N}\frac{^0d}{dt}\mathbf{H}_i = \sum_{i=1}^{N}\Big[&\mathbf{I}_{i\mathrm{C}}\cdot\frac{^id}{dt}\boldsymbol{\omega}^{i/0}+\boldsymbol{\omega}^{i/0}\times\big(\mathbf{I}_{i\mathrm{C}}\cdot\boldsymbol{\omega}^{i/0}\big)+\mathbf{R}_i\times m_{i\mathrm{C}}\mathbf{A}_i\\ &+2h_i\big(-\dot{\phi}_i\sin\phi_i\hat{\mathbf{e}}_{i1}+\boldsymbol{\omega}^{i/0}\times\cos\phi_i\hat{\mathbf{e}}_{i1}\big)\Big].\end{aligned} \tag{2.15}$$

For a completely reactionless system with only internal torques acting on the system, the total angular momentum of the system is conserved about the mass center and Kane's method [83, 86] yields

$$\sum_{i=1}^{N}\left(\frac{^0d}{dt}\mathbf{H}_{\mathrm{c}i}\cdot\frac{\partial\boldsymbol{\omega}_i}{\partial\dot{q}_j}\right)=0, \tag{2.21}$$

where $\mathbf{H}_{\mathrm{c}i}$ is the angular momentum about the mass center of the ith composite body and $\boldsymbol{\omega}_i$ is the angular velocity of body i in an inertial frame. Each generalized coordinate is the angular position of a body relative to its neighboring inboard body, $q_j=\theta_j$, and the generalized velocities are the time derivatives of the generalized coordinates, $\dot{q}_j=\dot{\theta}_j$. The partial angular velocities, shown in Eq. (2.20), are the basis vectors aligned with the joint axes.

After the arm has grasped the payload, the payload-augmented outer body resembles Fig. 3.2, where O_3 is the origin of the body 3-fixed coordinate system,

$\mathbf{r}_{\mathrm{p}}$ is the position vector from O_3 to the payload mass center, $\mathbf{r}_3$ is the position vector from O_3 to the body 3 mass center, and $\mathbf{r}_{3\mathrm{p}}$ is the position vector from O_3 to the combined mass center. If $\mathbf{a} = \mathbf{r}_{3\mathrm{p}} - \mathbf{r}_3$ and $\mathbf{b} = \mathbf{r}_{\mathrm{p}} - \mathbf{r}_{3\mathrm{p}}$, the inertia dyadic $\mathbf{I}_{3\mathrm{p}}$ of the augmented outer body about its mass center is determined by the parallel axis theorem [28]

$$\mathbf{I}_{3\mathrm{tot}} = \mathbf{I}_3 + \mathbf{I}_{\mathrm{p}} - m_3(a^2\mathbf{1} - \mathbf{aa}) - m_{\mathrm{p}}(b^2\mathbf{1} - \mathbf{bb}), \tag{3.7}$$

where $\mathbf{I}_3$ is the central inertia dyadic of the outer arm segment without the CMGs, $\mathbf{I}_{\mathrm{p}}$ is the central inertia dyadic of the payload, and a and b are the magnitudes of $\mathbf{a}$ and $\mathbf{b}$, respectively. Besides the obvious addition of mass to the outer body, a payload introduces products of inertia in the inertia matrix of the outer body and shifts the location of the outer body's mass center. In the general case where this shift causes the system mass center to deviate from the innermost joint axis, the resulting acceleration causes a reaction force on the base. Kane's method is employed, as in the previous example without a payload, to find the equations of motion for this system. In this general case with a mass offset due to an added payload, the equations of motion are

$$\sum_{i=1}^{N}\left[\left(m_{i\mathrm{C}}\mathbf{A}_i - \mathbf{F}_i^a\right)\cdot\frac{\partial\mathbf{V}_i}{\partial\dot{q}_j} + \left(\frac{{}^0d}{dt}\mathbf{H}_{ci} - \mathbf{M}_{\mathrm{c}i}^a\right)\cdot\frac{\partial\boldsymbol{\omega}_i}{\partial\dot{q}_j}\right] = 0, \tag{2.17}$$

where $\mathbf{F}_i^a$ is the total active force that does work on composite body i and $\mathbf{M}_{\mathrm{c}i}^a$ is the total active moment about the ith mass center that does work on composite body i.

An examination of the power consumption of an N-body system begins with the system energy, which is entirely kinetic. The total energy of the general CMG

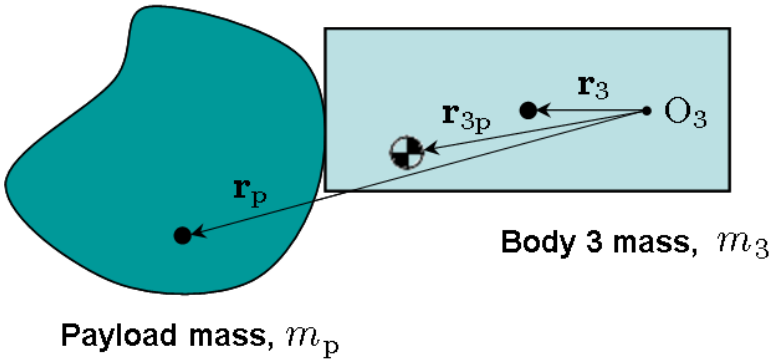

Figure 3.2: Schematic of outer arm segment (body 3) with attached payload.

system with a payload is

$$E = \sum_{i=1}^{N} E_i \; = \frac{1}{2} \sum_{i=1}^{N} \Bigg\{ (\boldsymbol{\omega}^{i/0} \cdot \mathbf{I}_i \cdot \boldsymbol{\omega}^{i/0}) + (m_{i\mathrm{C}} \mathbf{V}_i \cdot \mathbf{V}_i) + \sum_{j=1}^{S} \Big[(\boldsymbol{\omega}^{\mathrm{G}_{ij}/0} \cdot \mathbf{I}_{\mathrm{G}_{ij}} \cdot \boldsymbol{\omega}^{\mathrm{G}_{ij}/0}) + (\boldsymbol{\omega}^{\mathrm{R}_{ij}/0} \cdot \mathbf{I}_{\mathrm{R}_{ij}} \cdot \boldsymbol{\omega}^{\mathrm{R}_{ij}/0}) \Big] \Bigg\}, \tag{3.8}$$

where S is the number of CMGs on each body. $\mathbf{I}_i$ is the central inertia dyadic of the ith arm segment without the CMGs. $\mathbf{I}_{\mathrm{G}_{ij}}$ is the central inertia dyadic of the jth gimbal on body i and $\mathbf{I}_{\mathrm{R}_{ij}}$ is the central inertia dyadic of the jth CMG rotor on body i. G_{ij} and R_{ij} also represent the jth gimbal-fixed frame on body i and the jth rotor-fixed frame on body i, respectively. Equation (3.8) describes the total energy of a general system in which each body rotates about an arbitrary axis that does not pass through its mass center. It is assumed that the motion of the ith pair of CMGs is such that each composite body's mass center is constant in the ith body-fixed frame. Thus, the total translational kinetic energy for each composite body can be expressed in terms of the composite mass-center velocity

as measured from O_1.

The time derivative of Eq. (3.8) yields the total change in kinetic energy, or power, of the system:

$$
\begin{aligned}
P = \sum_{i=1}^{N} \Bigg\{ & \left(\frac{{}^{i}d}{dt} \boldsymbol{\omega}^{i/0} \cdot \mathbf{I}_i \cdot \boldsymbol{\omega}^{i/0} \right) + \left(m_{i\mathrm{C}} \mathbf{V}_i \cdot \mathbf{A}_i \right) \\
& + \sum_{j=1}^{S} \Bigg[\left(\frac{{}^{\mathrm{G}_{ij}}d}{dt} \boldsymbol{\omega}^{\mathrm{G}_{ij}/0} \cdot \mathbf{I}_{\mathrm{G}_{ij}} \cdot \boldsymbol{\omega}^{\mathrm{G}_{ij}/0} \right) \\
& + \left(\frac{{}^{\mathrm{R}_{ij}}d}{dt} \boldsymbol{\omega}^{\mathrm{R}_{ij}/0} \cdot \mathbf{I}_{\mathrm{R}_{ij}} \cdot \boldsymbol{\omega}^{\mathrm{R}_{ij}/0} \right) \Bigg] \Bigg\}. \qquad (3.9)
\end{aligned}
$$

As Section 2.3 discusses, negative values of power indicate energy extracted from the motion of the connected system components. However, this energy-recovery process cannot be perfect, and in practice it is likely inefficient. In the probable case where the robotic arm is not designed to regeneratively recover this energy, the system's power consumption is approximated by the sum of the absolute values of kinetic-energy change computed for each system component. The assumption that each composite body's mass center is constant in its own body-fixed frame implies that the CMGs have only rotational energy associated with their motion. Since each composite body has kinetic energy due to both translation and rotation, the power for each arm segment is given by the sum of the translational and rotational change in kinetic energy.

A general description of the robot's dynamics provides the means to understand the effects of a payload on power consumption. We examine these effects by first considering simple cases, beginning with the single-body system shown in Fig. 3.3. This system consists of a single arm segment with a scissored pair of CMGs

whose combined mass center is offset from the joint axis. This offset causes the mass center to accelerate in an inertial frame as the body rotates. The dynamics of this single-body system is therefore governed by Eq. (2.17) with $N = 1$. A force is transmitted to the stationary base due to the mass center's acceleration, but it vanishes from the equation of motion as a workless constraint force. This reaction force imparts an additional moment to the body about its mass center; however, since this moment is about an axis orthogonal to $\hat{\mathbf{e}}_{11}$, it also vanishes. Another reaction torque at the contact between the base and the arm segment results from the fact that the inertia dyadic of the system about the mass center is time-varying in an inertial frame. However, it also drops out of the equation of motion as a workless constraint torque. Therefore, without active forces and torques on the system, Eq. (2.17) reduces to

$$\left(m_{1\mathrm{C}}\mathbf{A}_1 \cdot \frac{\partial \mathbf{V}_1}{\partial \dot{q}_1}\right) + \left(\frac{{}^0d}{dt}\mathbf{H}_{\mathrm{c}1} \cdot \frac{\partial \boldsymbol{\omega}_1}{\partial \dot{q}_1}\right) = 0. \tag{3.10}$$

When the vectors and dyadics are expressed in body-1 coordinates, Eq. (3.10) can be rewritten in matrix form

$$\begin{bmatrix} 0 \\ -m_{1\mathrm{C}}({}^1R_{1,3}\ddot{\theta}_1 + {}^1R_{1,2}\dot{\theta}_1^2) \\ m_{1\mathrm{C}}({}^1R_{1,2}\ddot{\theta}_1 - {}^1R_{1,3}\dot{\theta}_1^2) \end{bmatrix} \cdot \begin{bmatrix} 0 \\ -{}^1R_{1,3} \\ {}^1R_{1,2} \end{bmatrix} + \begin{bmatrix} {}^1I_{11}\ddot{\theta}_1 - 2h_1\dot{\phi}_1\sin\phi_1 \\ {}^1I_{12}\ddot{\theta}_1 - {}^1I_{13}\dot{\theta}_1^2 \\ {}^1I_{13}\ddot{\theta}_1 + {}^1I_{12}\dot{\theta}_1^2 \end{bmatrix} \cdot \begin{bmatrix} 1 \\ 0 \\ 0 \end{bmatrix} = 0, \tag{3.11}$$

and the equation of motion is

$$\left({}^1I_{11} + m_{1\mathrm{C}}{}^1R_{1,2}^2 + m_{1\mathrm{C}}{}^1R_{1,3}^2\right)\ddot{\theta}_1 - 2h_1\dot{\phi}_1\sin\phi_1 = 0. \tag{3.12}$$

In Eqs. (3.11)-(3.12), ${}^1R_{1,i}$ are the components of the column matrix ${}^1R_1$, which is the vector $\mathbf{R}_1$ expressed in body-1 coordinates. ${}^1I_{ij}$ are the elements of the inertia matrix, ${}^1I_{1C}$, which is the dyadic $\mathbf{I}_{1C}$ expressed in body-1 coordinates. With the exception of the added mR^2 terms in Eq. (3.12), the equation of motion for this system with a mass-center offset is the same as that for a system with a stationary mass center during body rotations. In other words, a mass-center offset that might be caused by the addition of a payload affects only inertia-like terms in the equation of motion for this single-body system.

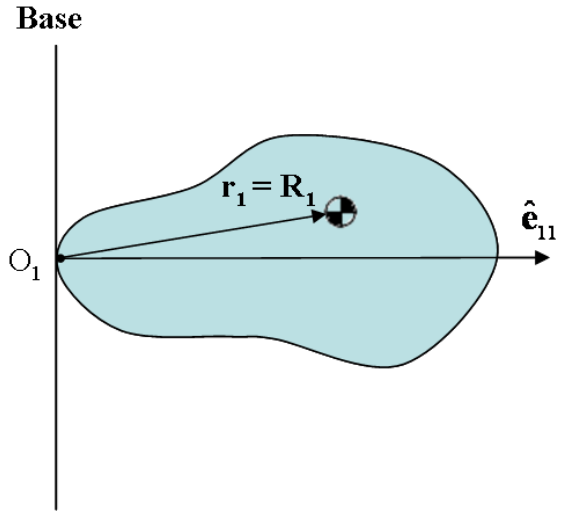

Figure 3.3: Single-body system with mass-center offset from joint axis.

It is also evident from Eq. (3.11) that while the constraint forces and torques at the base contact do not change the energy of the system, they do change its total angular momentum. However, since

$$\frac{{}^0d}{dt}\mathbf{H}_1 \cdot \hat{\mathbf{e}}_{11} = 0, \tag{3.13}$$

and since $\hat{\mathbf{e}}_{11}$ is a unit vector that is constant in an inertial frame, then

$$\mathbf{H}_1 \cdot \hat{\mathbf{e}}_{11} = C, \tag{3.14}$$

where $C \in \mathbb{R}$ is any constant. This momentum integral of the equation of motion in an inertial frame [83] implies that angular momentum is conserved about $\hat{\mathbf{e}}_{11}$ and the associated generalized coordinate, θ_1, is cyclic and does not appear in the system Lagrangian [94]. In other words, since the CMGs impart torque on the body through internal momentum exchange, they act only in the direction along which angular momentum is conserved, i.e., along the joint axis.

We now consider a two-body system consisting of a spherical inboard body with its mass center on the joint axis and an outboard body with an arbitrary mass distribution. Figure 3.4(a) is a sketch of such a configuration. The inner body's mass center is stationary since $\mathbf{R}_1$ has a constant length and is coincident with the joint axis. In the two-body case, a mass-center offset on the outer body contributes additional coupled forces and torques to the equations of motion for the connected bodies. However, like the single-body case, angular momentum is conserved about $\hat{\mathbf{e}}_{11}$, or the joint axis of the inner body. The system Lagrangian for a general two-body system, and for the general N-link system, is independent of θ_1. We explain this result by first stating that the robot arm is connected to the base by a revolute joint at O_1, which can support a torque only about the transverse directions, $\hat{\mathbf{e}}_{12}$ and $\hat{\mathbf{e}}_{13}$. Reaction torques act between each joint and at the contact between the spacecraft base and the inner arm segment. Since the constraint torques at the contacts between each arm segment cancel except at O_1, the reaction torque components at the base are found by projecting the resultant torque about O_1 in Eq. (2.15) onto the transverse directions. The components of reaction torque at the base are $\frac{^0d}{dt}\mathbf{H} \cdot \hat{\mathbf{e}}_{12} = \tau_{r2}$ and $\frac{^0d}{dt}\mathbf{H} \cdot \hat{\mathbf{e}}_{13} = \tau_{r3}$. We conclude that although the

equations of motion for the multi-body system include additional inertial torques and forces, angular momentum is always conserved about the innermost joint axis, $\hat{\mathbf{e}}_{11}$.

Reaction forces also act on the revolute joint at O_1, which is capable of supporting a force in any direction. Since the constraint forces, like the constraint torques, are canceled at the joints between each arm segment, the reaction force at the base is simply the resultant force on the system:

$$\mathbf{F} = \sum_{i=1}^{N} m_{i\mathrm{C}} \mathbf{A}_i. \tag{3.15}$$

While the single- and multi-body analyses demonstrate that the general system is not guaranteed to be reactionless, reaction forces and torques can be eliminated with a mass-balanced system design, as illustrated in Fig. 3.4(b). The general system that produces base reactions certainly applies to the payload problem, where the payload mass properties are arbitrary. However, our analysis also shows that the general system always conserves angular momentum about one axis. Since the single-body CMG system conserves momentum about the active joint axis, one might operate the links sequentially in a planned maneuver to avoid either gimbal saturation or disturbances in a particular direction. Additionally, this operations concept causes the dynamic behavior of the multi-body system to resemble that of the single-body system, possibly reducing base reactions and power consumption.

To show how momentum actuation of a robot affects base reactions on a spacecraft, an identical system is modeled with conventional joint motors. The vector torque at the base contact is given by Eq. (2.15) without the CMG terms. Unlike the CMG system, the reaction torque has components in all three directions: $\hat{\mathbf{e}}_{11}$,

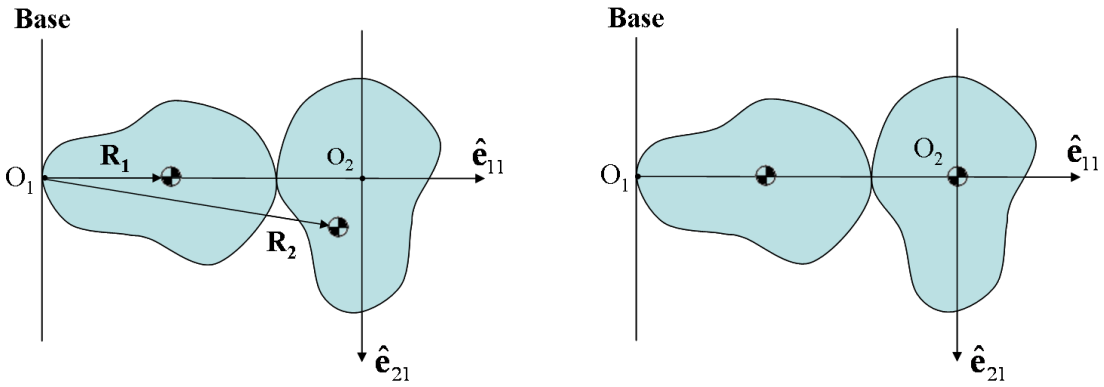

(a) General system.

(b) Mass-balanced system.

Figure 3.4: Two-body system.

$\hat{\mathbf{e}}_{12}$, and $\hat{\mathbf{e}}_{13}$. The reaction force at the base for the conventional system is given by Eq. (3.15). With these expressions, the base reactions for the CMG system are compared to those for an otherwise identical system with direct-drive motors. This analysis complements a detailed power comparison of these two systems presented in concurrent work by Brown [95].

References [19, 20, 21] were among the first studies in momentum actuation of a space-robotic manipulator; however, the base-reaction benefits and power costs for such a system are not investigated in this literature. For the numerical analysis in Section 3.4, we evaluate the simultaneous motion of both general and mass-balanced three-body CMG systems and compare these cases to sequentially rotating CMG systems. The effects of these operations concepts on power consumption are also briefly considered. Our goal in the comparison of these operations concepts is not optimal steering, but to suggest that base reactions can be traded for power. Finally, we demonstrate reduced base reactions with CMG actuation by including additional results for a conventional system with direct-drive motors.

3.4 Feedback-Control Design

The full nonlinear equations of motion for the N-body CMG system are accommodated in a feedback-control design, with the nonlinear terms in the feedforward portion of the control loop. The plant is in the general form

$$\ddot{\Theta} + X\dot{\Phi} + F = 0, \tag{3.16}$$

where $\ddot{\Theta} \in \mathbb{R}^{N\times 1}$ contains the relative body angular accelerations, $\dot{\Phi} \in \mathbb{R}^{N\times 1}$ contains the gimbal rates with the coefficient matrix $X \in \mathbb{R}^{N\times N}$, and $F \in \mathbb{R}^{N\times 1}$ contains the nonlinear Coriolis and centripetal terms of the system's equations of motion.

With the plant in this form, a proportional-derivative (PD) feedback-control law is derived by seeking gimbal rates such that the CMG equations of motion resemble a linear second-order system

$$\ddot{\Theta} + Z\dot{\Theta} + W\Theta = 0. \tag{3.17}$$

In Eq. (3.17), we define matrices $Z = \mathrm{diag}(2\zeta\omega_\mathrm{n}) \in \mathbb{R}^{N\times N}$ and $W = \mathrm{diag}(\omega_\mathrm{n}^2) \in \mathbb{R}^{N\times N}$, where Z represents the generalized damping desired in the feedback law, and W represents the generalized stiffness. The control is based on an error function, $\Theta_\mathrm{e} = \Theta_\mathrm{d} - \Theta$, where $\Theta_\mathrm{d} \in \mathbb{R}^{N\times 1}$ contains each body's desired relative angular position, and $\Theta_\mathrm{e} \in \mathbb{R}^{N\times 1}$ contains the error in each body's relative angular position. The error dynamics for this system are then described by

$$\ddot{\Theta}_{\mathrm{e}} + Z\dot{\Theta}_{\mathrm{e}} + W\Theta_{\mathrm{e}} = 0. \tag{3.18}$$

Solving for $\dot{\Phi}$ from Eq. (3.16) and Eq. (3.17) leads to a feedback-control law for the CMG gimbal rates:

$$\dot{\Phi} = X^{-1}\Big(Z\dot{\Theta}_{\mathrm{e}} + W\Theta_{\mathrm{e}} - F\Big). \tag{3.19}$$

Equation (3.19) is not a linearization, but an exact linear expression resulting from algebraic manipulation. Since subtracting the nonlinear term, F, may be problematic in the case where the state variables are not perfectly known, full state knowledge is assumed.

This system is controllable except in the case where the Jacobian, X, is singular, or when $\det(X) = 0$. Thus, it encounters a singularity when

$$\prod_{i=1}^{N} \sin\phi_i = 0. \tag{3.20}$$

This relationship is satisfied when any gimbal angle, $\phi_i = n\pi$, $n \in \mathbb{Z}$. This condition arises in the robotic system at the gimbal angle where any CMG scissored pair stores its maximum angular momentum. As the scissored pair moves towards this saturation limit, the gimbal rate required to achieve a desired output torque can be impossibly high even if the Jacobian's determinant is finite. Gimbals can only rotate so fast in practice. For this reason, among others, a scissored pair may be best limited to a range of gimbal angles within which a certain maximum torque can be guaranteed for finite gimbal rates.

A more sophisticated control architecture may offer certain performance benefits, but the virtues of this design include its ease of implementation and analysis. Our focus is not this specific architecture but instead devising a means to implement motion profiles that will enable the analysis of base reactions and power usage.

3.5 Simulation Results

In order to explore how the choice of operations concept and actuation method affect base reactions and power, a maneuver is constructed in which each joint angle tracks a step input with the control law in Eq. (3.19). This maneuver is analyzed for CMG and direct-drive systems using both simultaneous and sequential motion of the bodies. In the sequential-rotation method for the proposed three-body system, designated links rotate in three stages. In each of these stages, the resulting dynamics resemble the general single-body system. In a given stage, stationary inboard system components are treated as part of the spacecraft base while stationary outboard components are treated as simply an added payload. The major difference between the three possible stages of the maneuver is the amount of mass and inertia that the active arm segment moves. Bodies that are further inboard carry more mass and inertia, resulting in higher base reactions and power consumption.

In these simulations, the inertia dyadic $\mathbf{I}_{i\mathrm{C}}$ for each arm segment with its CMGs (but without a payload) is identical to all the others. The two inboard bodies are spherical with their mass centers on their respective joint axes while the mass center of the outer body is offset from its joint axis by the added payload. Multiple

spherical bodies may be difficult to realize in practice, but their simplicity makes the results of this study clearer to interpret without sacrificing anything fundamental. A detailed evaluation of an arbitrary system of interest can be carried out with the equations of motion provided in Section 3.3. However, this system with an arbitrary payload is considered a general system for the remainder of this chapter, since it is compared to a mass-balanced case in Section 3.5.1.

3.5.1 Comparison of Operations Concepts and Actuators

To obtain the simulation results in this chapter, the MATLAB® function **ode45.m** is used to integrate the equations of motion in Eq. (2.17) from initial time $t_0 = 0$ s to final time $t_f = 12$ s. The simulation parameters for this comparative study are included in Table 3.1. The CMG parameters are based on the Honeywell M50 CMG [17], but we do not model rotor drag or losses in the gimbal motor, gear train, or drive electronics. The gimbals begin in a configuration for which the net angular momentum of each scissored pair is zero. Since the gimbal angles in this simulation are measured from the joint axis, the initial gimbal angles are $\pm\pi/2$ rad for each scissored pair.

Figures 3.5 - 3.6 include the vector components of reaction force, $\mathbf{F}_r$, and reaction torque, $\boldsymbol{\tau}_r$, at the robot base during a maneuver in which each body tracks a step input with an amplitude of 0.1 rad. Figure 3.7 illustrates the non-recoverable system power for this maneuver. In part (a) of Figs. 3.5 - 3.7, the bodies are moved simultaneously at $t = 1$ s while part (b) of Figs. 3.5 - 3.7 shows results from when the bodies are rotated sequentially, from innermost to outermost, at $t = 1, 4.5$, and 8 s. For each operations concept, we calculate the integral of the reaction-force magnitude, $\int |\mathbf{F}_r| \, dt$, and the integral of the reaction-torque

Table 3.1: Closed-Loop Simulation Parameters for Example Step Maneuver to Compare Operations Concepts and Actuators.

Parameter	Value
Initial relative body angles, $\theta_i(0)$	(0, 0, 0) rad
Initial relative body rates, $\dot{\theta}_i(0)$	(0, 0, 0) rad/s
Damping ratio, ζ	0.707
Natural frequency, ω_{n}	π rad/s
CMG rotor angular momentum, h_i	50 N-m-s
Rotor spin speed, Ω_{R}	200 rad/s
Rotor inertia, I_{R}	0.25 kg-m^2
Gimbal inertia, I_{G}	0.125 kg-m^2
Body inertia, I_i	20 kg-m^2
Payload inertia, I_{p}	2 kg-m^2
Body mass, m_i	10 kg
Payload mass, m_{p}	2 kg
Position of body 3 CM, ${}^3r_{3\mathrm{p}}$	[1.25, 0, 0.25] m

magnitude, $\int |\boldsymbol{\tau}_r|\, dt$. These values provide a measure of the extent that forces and torques are being transmitted to the spacecraft. Peak values of the reaction-force and reaction-torque magnitudes, $|\mathbf{F}_r|_{\max}$ and $|\boldsymbol{\tau}_r|_{\max}$, are also calculated. Since the general CMG and conventional systems have identical mass properties, the reaction forces for these systems are equal. In a comparison of identical systems driven by either CMGs or conventional joint motors, [95] demonstrates that the power expenditures for the two systems are equal. Therefore, all figures for reaction forces and power represent both actuation methods.

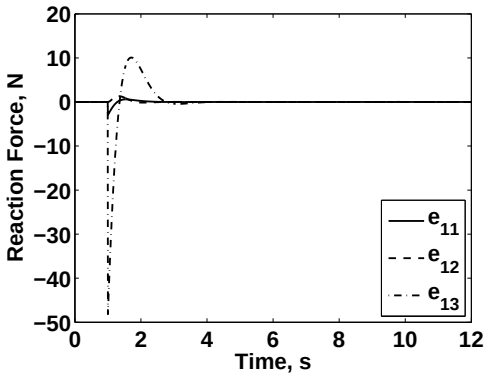

(a) Simultaneous motions.

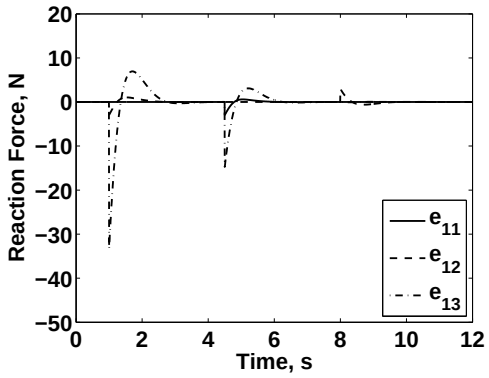

(b) Sequential motions.

Figure 3.5: Vector components of reaction force during step response for the general CMG and conventional systems.

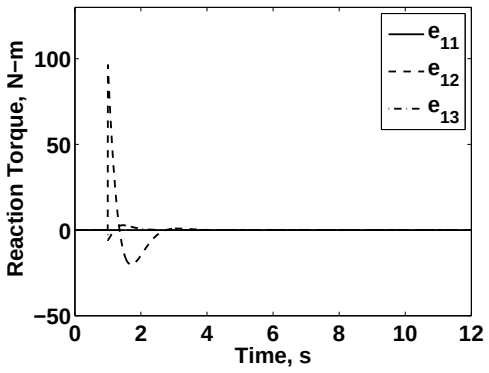

(a) Simultaneous motions.

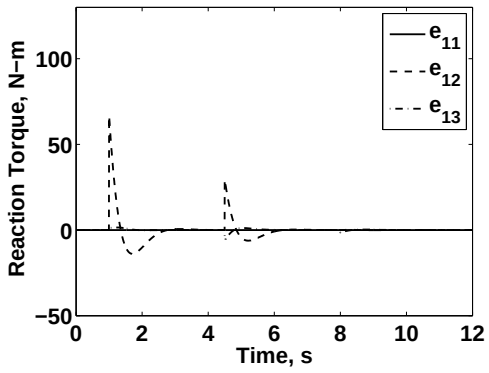

(b) Sequential motions.

Figure 3.6: Vector components of reaction torque during step response for the general CMG system.

According to the results in Table 3.2, $\int |\mathbf{F}_r|\, dt$ and $\int |\boldsymbol{\tau}_r|\, dt$ for the CMG system over the slew duration are roughly the same for both operations concepts; however, the peak values for these quantities are each about 45% higher for simultaneous motions than they are for sequential motions. $\int P\, dt$ is about 5% lower for the

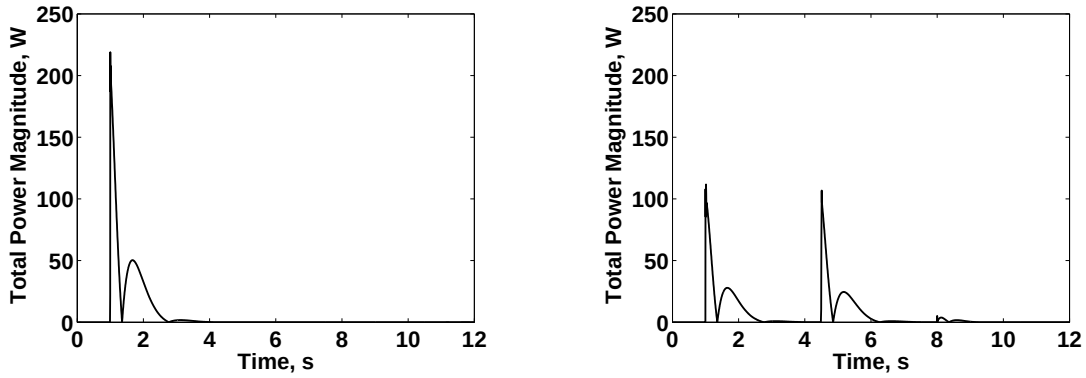

(a) Simultaneous motions.

(b) Sequential motions.

Figure 3.7: Power of the general CMG and conventional systems during step response.

simultaneous method than for the sequential method, but the peak value, $P_{\max}$, is higher for the simultaneous method by nearly a factor of 2.

The system angular momentum about O_1 is shown in Fig. 3.8 for both operations concepts. Section 3.3 stated that the angular momentum of the system about the base contact at O_1 cannot be conserved because of the constraint force and torque acting at that point. The nonzero components of $\mathbf{H}$ at the end of the maneuver demonstrate this principle, indicating reaction torque at the base.

Table 3.2 also includes the simulation results for the general conventional system using both operations concepts. For this system, Fig. 3.9 contains the vector components of reaction torque for the simultaneous and sequential cases. The vector components of reaction force for the conventional system are identical to the CMG case and are shown in Fig. 3.5. The base reactions for the conventional system differ from the CMG system only in the amount of reaction torque imparted to the spacecraft base. For simultaneously rotating links, $\int |\boldsymbol{\tau}_r| \; dt$ and $|\boldsymbol{\tau}_r|_{\max}$

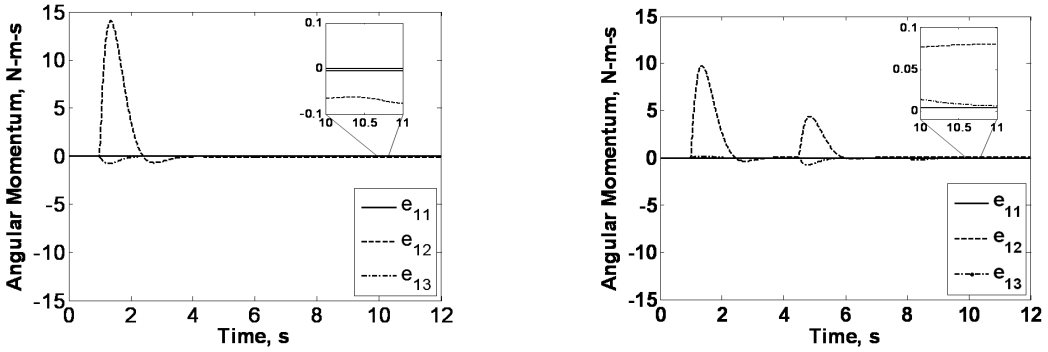

(a) Simultaneous motions.

(b) Sequential motions.

Figure 3.8: Vector components of system angular momentum about O_1 for the general CMG system.

are each about 20% lower for the general CMG system when compared to the conventional system. While there are some changes to the reaction torque in the transverse directions, the increased $|\boldsymbol{\tau}_r|$ for the conventional system results mainly from the additional large joint-axis component from the joint motor.

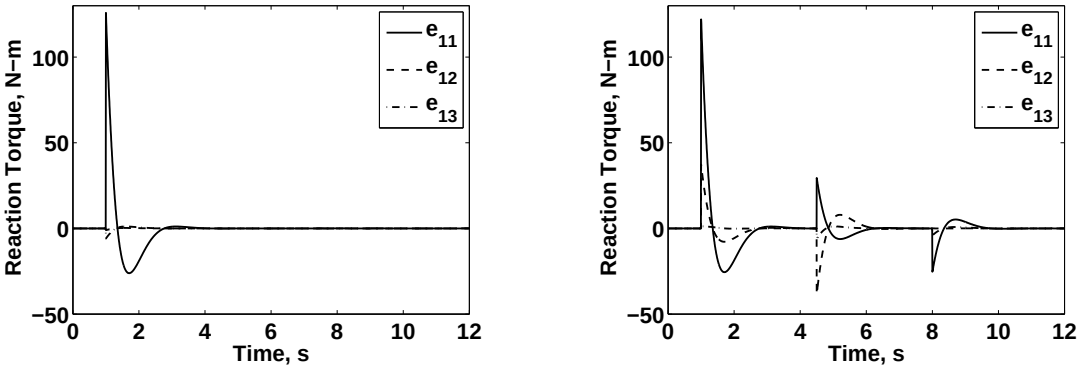

(a) Simultaneous motions.

(b) Sequential motions.

Figure 3.9: Vector components of reaction torque during step response for the general conventional system.

The same set of simulations are performed for a mass-balanced system. The difference between this system and the previously-discussed general system is the mass-center location of body 3, which is ${}^1r_{3\mathrm{p}} = {}^1[1\ 0\ 0]^{\mathrm{T}}$ when expressed in body-1 coordinates. This position is also the location of the system mass center. The mass-balanced system is completely reactionless when using CMG actuation, allowing one to design for reaction torques due solely to the actuation method, not inertial properties. In both the simultaneous- and sequential-rotation methods for each system, the vector components of $\mathbf{F}_r$ are zero since the system mass center is always stationary on $\hat{\mathbf{e}}_{11}$. For the CMG system, the vector components of $\boldsymbol{\tau}_r$ are also zero since the system inertia dyadic is spherical. In the case of direct-drive actuation, a mass-balanced system is obviously not reactionless, as evidenced by the reaction torques in Fig. 3.10 and the results in Table 3.3. Even with a mass-balanced arm design, there is a significant amount of reaction torque at the base. Finally, the mass-balanced CMG and direct-drive systems show the same trends for $\int P\ dt$ and $P_{\max}$ that are observed for the general system with an arbitrary payload. As expected, these values are shifted lower in the mass-balanced case, demonstrating that mass balancing saves power when using either operations concept.

3.5.2 Monte-Carlo Analysis

This section presents a statistical analysis of base reactions and power for the operations concepts and actuation methods discussed in the previous section. A Monte-Carlo simulation is performed for the general CMG and conventional systems over the initial relative body angles, step amplitudes, and mass-center offset of the outboard body while holding the control gains and all other simulation parameters fixed. Each of these parameters is randomly drawn from a uniform

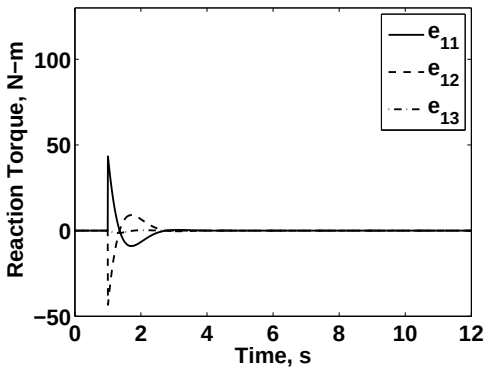

(a) Simultaneous motions.

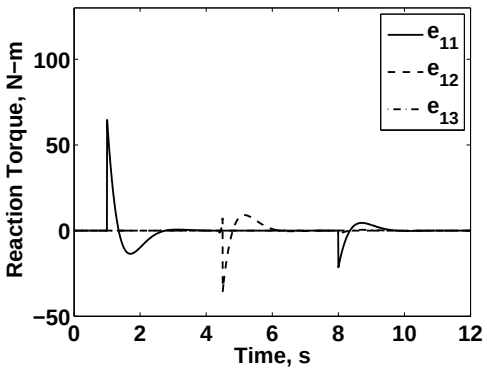

(b) Sequential motions.

Figure 3.10: Nonzero vector components of reaction torque during step response for the mass-balanced conventional system.

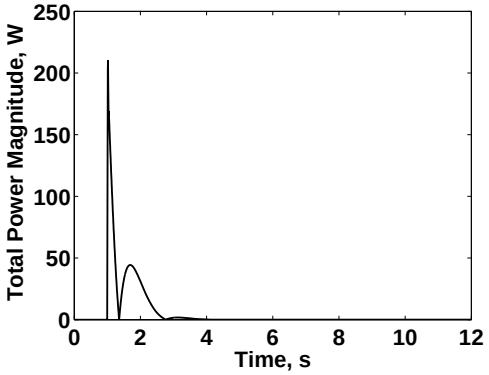

(a) Simultaneous motions.

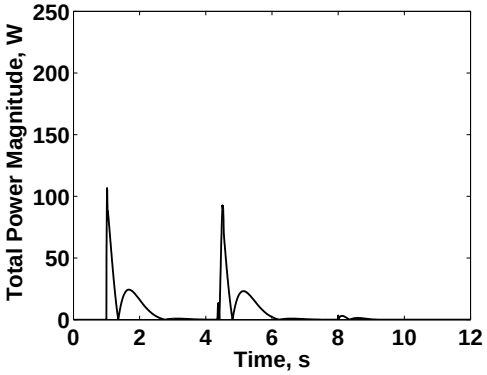

(b) Sequential motions.

Figure 3.11: Power of the mass-balanced CMG and conventional systems during step response.

distribution over the intervals listed in Table 3.4. Besides these varied parameters, the same parameters from Table 3.1 are used for this analysis.

In every realization of the maneuver, each body has a different, randomly-drawn initial relative body angle and step amplitude. Varying the mass-center offset of

the combined outboard body is achieved by varying the location of the payload mass center. Variation of these parameters avoids payload-related biases in the histograms for $\int |\mathbf{F}_r|\ dt$, $|\mathbf{F}_r|_{\max}$, $\int |\boldsymbol{\tau}_r|\ dt$, $|\boldsymbol{\tau}_r|_{\max}$, $\int P\ dt$, and $P_{\max}$. Figures 3.12 - 3.13 contain histograms of $\int |\mathbf{F}_r|\ dt$ and $|\mathbf{F}_r|_{\max}$ for the general CMG and conventional systems using both operations concepts. Figures 3.14 - 3.15 contain the $\int |\boldsymbol{\tau}_r|\ dt$ and $|\boldsymbol{\tau}_r|_{\max}$ histograms for the CMG system and Figs. 3.16 - 3.17 show the same data for the conventional system. Finally, Figs. 3.18 - 3.19 contain histograms for $\int P\ dt$ and $P_{\max}$, which are accurate for both the general CMG and conventional systems. Table 3.5 summarizes these Monte-Carlo simulation results, indicating the mean values for each parameter.

Only the simultaneous-rotation method is considered when comparing actuation methods. Figs. 3.14(a) and 3.15(a) show the histograms of $\int |\boldsymbol{\tau}_r|\ dt$ and $|\boldsymbol{\tau}_r|_{\max}$ for simultaneous rotations. These figures, along with Table 3.5, indicate that the mean values of $\int |\boldsymbol{\tau}_r|\ dt$ and $|\boldsymbol{\tau}_r|_{\max}$ for the CMG system are each lower than the mean values of the conventional system by about a factor of 2.

Section 3.3 proposes sequential rotations for the CMG system so that one may choose the axis about which angular momentum is conserved. Sequentially rotating the direct-drive system offers no advantages over rotating the links of that system simultaneously, but the results are included in Table 3.5 and Figs. 3.16 - 3.17 for completeness. According to Table 3.5 and Fig. 3.12, the mean values of $\int |\mathbf{F}_r|\ dt$ and $\int |\boldsymbol{\tau}_r|\ dt$ for the CMG system are about 25% lower for simultaneous motions than for sequential motions. Table 3.5 also indicates that, on average, $|\mathbf{F}_r|_{\max}$ and $|\boldsymbol{\tau}_r|_{\max}$ are each about 5% higher for simultaneous motions than for sequential motions.

The mean value of $\int P\ dt$ for both actuation methods is 15% lower in the simul-

taneous case while the average $P_{\max}$ is about 5% higher for this operations concept. The lower average $\int P\ dt$ for simultaneous motions is due to a combination of factors. In the sequential case, the controller must not only force the entire motion of the rotating body, but it must also compensate for the consequent motion of the fixed system components. During simultaneous rotations, a body can use energy from the motion of its neighbors to assist its maneuver to the commanded position. To demonstrate this idea, we examine Eq. (3.9) for a two-body system: the simplest system that exhibits coupled motion. For sequential motions, when the outer body is rotating, Eq. (3.9) reduces to the single-body case with the outer body's mass properties. A rotation of the inner body also reduces Eq. (3.9) to the single-body case, where the mass properties of the inner body are augmented by the fixed outer body. However, for simultaneous motions, Eq. (3.9) is a function of the relative rates and accelerations for each system component. Some of these variables may be negative-valued, leading to subtractions in the inertial angular velocities and accelerations before the dot products in the power calculation are performed. The power used by a particular component in a system with simultaneously rotating bodies can thus be decreased in some cases with the direction of travel. However, such a reduction is not possible for sequential motions because all other body and gimbal rates are zero. These findings imply that for simultaneous motions, there likely exist paths where a given arm segment can exploit the motion of its neighbors to reach its end position, thereby using less power. In further exploration of this possibility, Chapter 4 investigates paths in joint space along which power is minimized.

3.6 Chapter Conclusions

Base reactions on a spacecraft due to the motion of an attached robotic system can be reduced or eliminated with CMG actuation. By revisiting the theoretical developments in Chapter 2, a detailed dynamics analysis is provided for general single- and multi-body systems. This analysis demonstrates that the general CMG system always conserves angular momentum about a stationary joint axis. This result motivates numerical studies of sequentially rotating links in addition to simultaneously rotating links.

A comparison of operations concepts and actuation methods is performed for an example maneuver in which each joint tracks a step input. The results from this example are confirmed in a Monte-Carlo statistical analysis. In terms of base reactions, CMG and direct-drive systems differ only in the amount of reaction torque imparted to the spacecraft base. In the general case with an arbitrary payload, the mean values of $\int |\boldsymbol{\tau}_r| \, dt$ and $|\boldsymbol{\tau}_r|_{\max}$ are each lower for the CMG system by a factor of 2. A mass-balanced CMG system is completely reactionless by virtue of internal momentum actuation while the direct-drive system imparts significant torque onto the base. In terms of operations concepts, the peak reaction-force and reaction-torque magnitudes for simultaneous motions of the CMG system are each about 5% higher and the peak power is about 20% higher than for the sequential case. However, the mean values for $\int |\mathbf{F}_r| \, dt$ and $\int |\boldsymbol{\tau}_r| \, dt$ are each about 25% lower in the simultaneous case. In addition, the energy expended for both actuation methods is 15% lower, on average, when the bodies move simultaneously, suggesting the existence of an optimal steering path that minimizes the energy expended by the system. This topic is further investigated in Chapter 4.

Table 3.2: Results Summary for Example Step Maneuver of a General System

	Simultaneous Motion		**Sequential Motion**	
Parameter	CMG	Direct-Drive	CMG	Direct-Drive
$\int \lvert\mathbf{F}_r\rvert \, dt$	14.9 N-s	14.9 N-s	15.8 N-s	15.8 N-s
$\lvert\mathbf{F}_r\rvert_{\max}$	48.2 N	48.2 N	33.4 N	33.4 N
$\int \lvert\boldsymbol{\tau}_r\rvert \, dt$	29.9 N-m-s	38.5 N-m-s	30.2 N-m-s	61.9 N-m-s
$\lvert\boldsymbol{\tau}_r\rvert_{\max}$	96.5 N-m	126.0 N-m	66.6 N-m	127.6 N-m
$\int P \, dt$	71.4 J	71.4 J	74.7 J	74.7 J
$P_{\max}$	218.9 W	218.9 W	111.7 W	111.7 W

Table 3.3: Results Summary for Example Step Maneuver of a Mass-Balanced System

	Simultaneous Motion		**Sequential Motion**	
Parameter	CMG	Direct-Drive	CMG	Direct-Drive
$\int \lvert\mathbf{F}_r\rvert \, dt$	0 N-s	0 N-s	0 N-s	0 N-s
$\lvert\mathbf{F}_r\rvert_{\max}$	0 N	0 N	0 N	0 N
$\int \lvert\boldsymbol{\tau}_r\rvert \, dt$	0 N-m-s	19.0 N-m-s	0 N-m-s	38.1 N-m-s
$\lvert\boldsymbol{\tau}_r\rvert_{\max}$	0 N-m	61.3 N-m	0 N-m	64.6 N-m
$\int P \, dt$	63.7 J	63.7 J	69.3 J	69.3 J
$P_{\max}$	209.9 W	209.9 W	106.7 W	106.7 W

Table 3.4: Intervals for Varied Parameters in Comparison Study.

Parameter	Value
Initial relative body angles, $\theta_i(0)$	$[0, 2\pi]$ rad
Step amplitude, $\Delta\theta_i$	$[-0.3, 0.3]$ rad
Position of body 3 CM, ${}^3\mathrm{r}_{3\mathrm{p}}$	$\{[2, 3], [-1, 1], [-1, 1]\}$ m

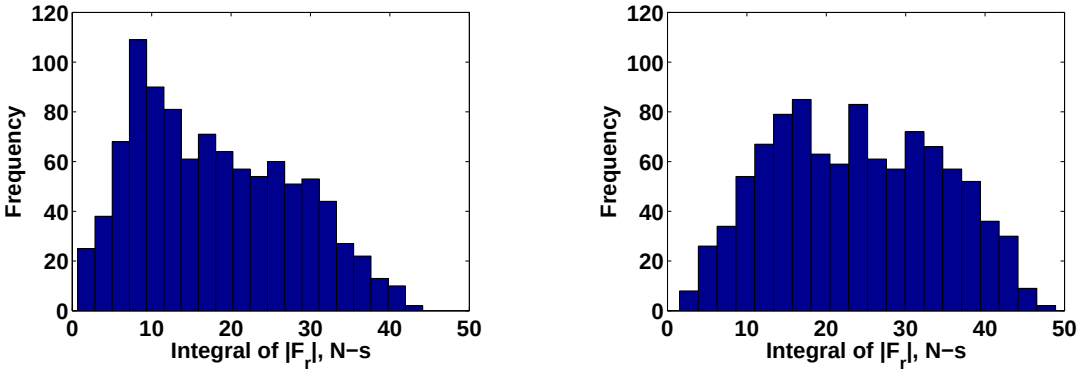

(a) Simultaneous motions.

(b) Sequential motions.

Figure 3.12: Histogram of $\int |\mathbf{F}_r|\ dt$ for the general CMG and conventional systems performing a step maneuver.

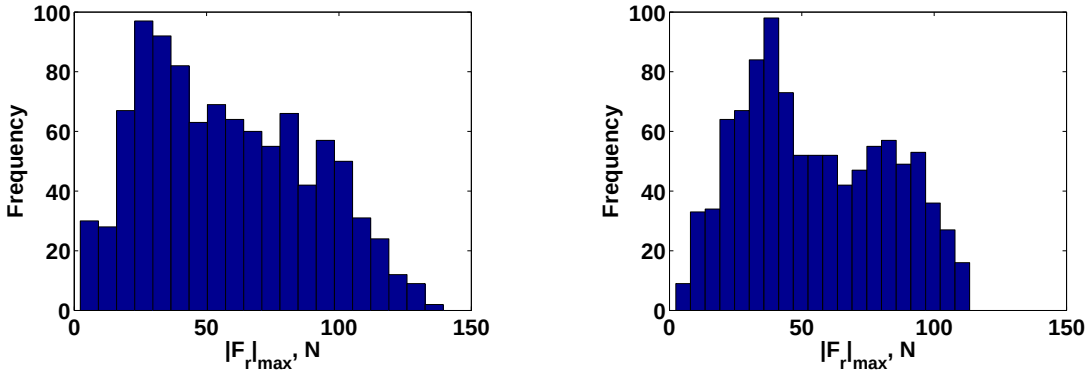

(a) Simultaneous motions.

(b) Sequential motions.

Figure 3.13: Histogram of $|\mathbf{F}_r|_{\max}$ for the general CMG and conventional systems performing a step maneuver.

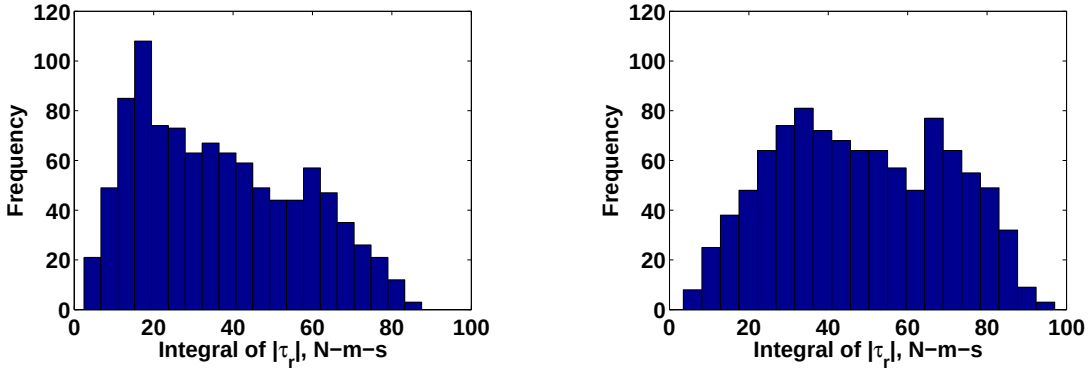

(a) Simultaneous motions.

(b) Sequential motions.

Figure 3.14: Histogram of $\int |\boldsymbol{\tau}_r| \, dt$ for the general CMG system performing a step maneuver.

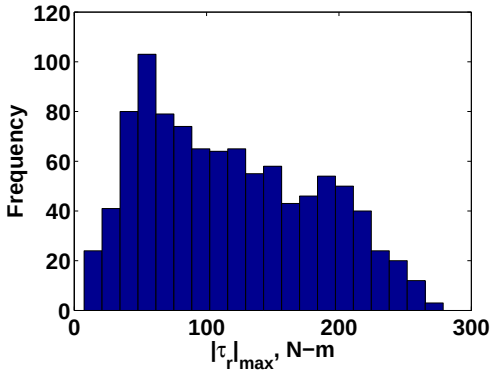

(a) Simultaneous motions.

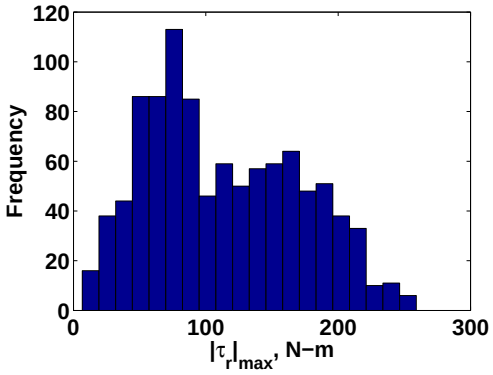

(b) Sequential motions.

Figure 3.15: Histogram of $|\boldsymbol{\tau}_r|_{\max}$ for the general CMG system performing a step maneuver.

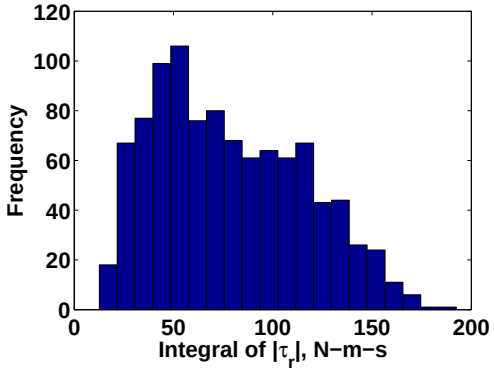

(a) Simultaneous motions.

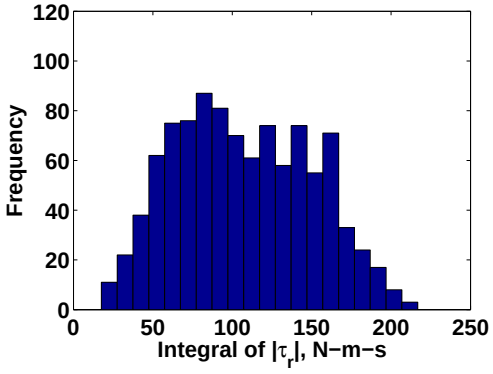

(b) Sequential motions.

Figure 3.16: Histogram of $\int |\boldsymbol{\tau}_r| \, dt$ for the general conventional system performing a step maneuver.

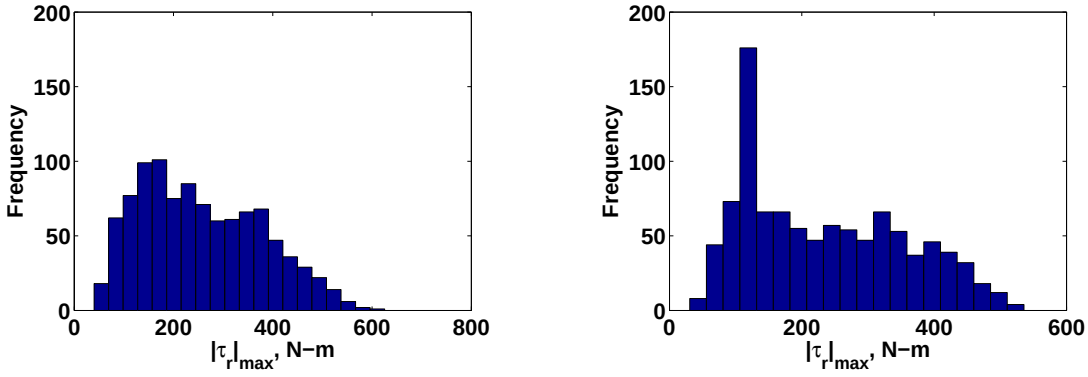

(a) Simultaneous motions.

(b) Sequential motions.

Figure 3.17: Histogram of $|\boldsymbol{\tau}_r|_{\max}$ for the general conventional system performing a step maneuver.

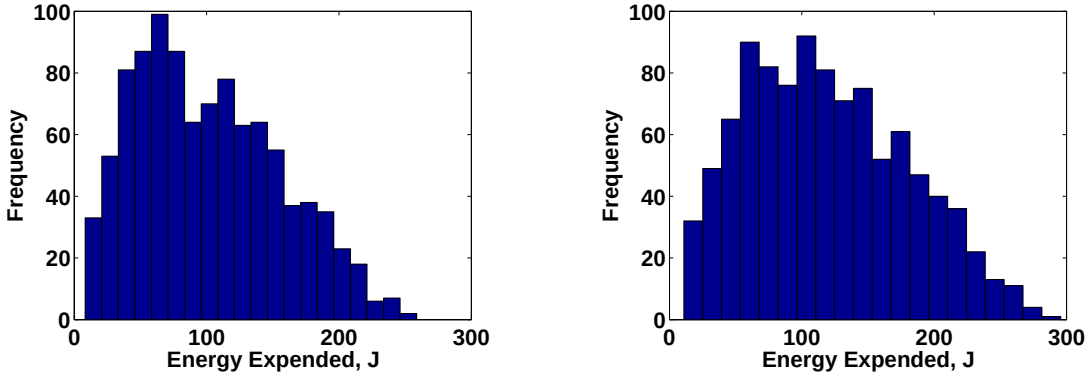

(a) Simultaneous motions.

(b) Sequential motions.

Figure 3.18: Histogram of $\int P\, dt$ for the general CMG and conventional systems performing a step maneuver.

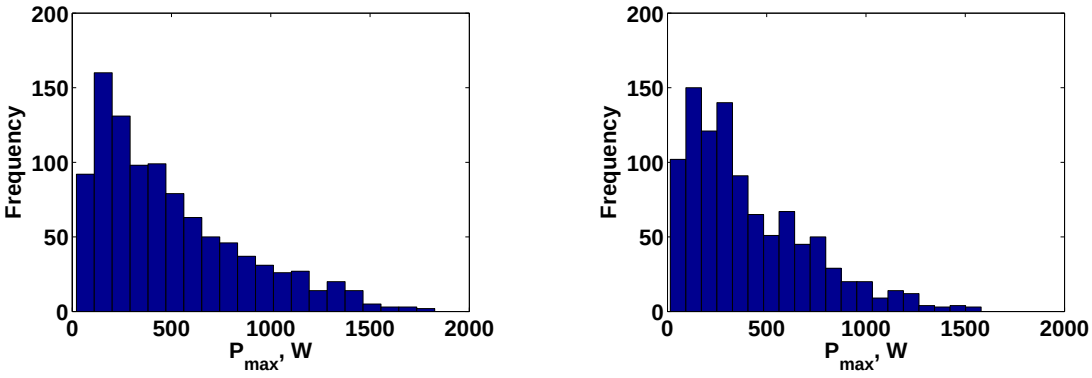

(a) Simultaneous motions.

(b) Sequential motions.

Figure 3.19: Histogram of $P_{\max}$ for the general CMG and conventional systems performing a step maneuver.

Table 3.5: Results Summary for Monte-Carlo Analysis

	Simultaneous Motion		**Sequential Motion**	
Parameter	CMG	Direct-Drive	CMG	Direct-Drive
Mean $\int \lvert\mathbf{F}_r\rvert \, dt$	18.0 N-s	18.0 N-s	23.8 N-s	23.8 N-s
Mean $\lvert\mathbf{F}_r\rvert_{\max}$	57.9 N	57.9 N	55.2 N	55.2 N
Mean $\int \lvert\boldsymbol{\tau}_r\rvert \, dt$	36.7 N-m-s	78.4 N-m-s	48.4 N-m-s	107.2 N-m-s
Mean $\lvert\boldsymbol{\tau}_r\rvert_{\max}$	118.0 N-m	256.2 N-m	113.4 N-m	234.3 N-m
Mean $\int P \, dt$	101.3 J	101.3 J	119.4 J	119.4 J
Mean $P_{\max}$	493.4 W	493.4 W	410.2 W	410.2 W

CHAPTER 4

POWER-OPTIMAL STEERING OF A CMG ROBOTIC SYSTEM

4.1 Introduction

This chapter revisits the agile imaging payload in Chapter 2 designed for high-speed target tracking. In this problem, a camera boresight attitude vector, $\mathbf{b}$, tracks a prescribed trajectory. There are multiple joint-kinematic solutions for a given boresight attitude command in a redundant robotic system, implying that a payload can track a target while simultaneously moving its arm segments and CMG gimbals to achieve some other goal, such as minimizing power consumption. While the boresight vector is tracking the commanded direction, null motion is added to the commanded joint angles in a linear feedback-control law. In this context, null motion refers to joint-angle adjustments that have no effect on the camera boresight attitude. The resulting change in the body and gimbal kinematics from the added null motion reduces the system's power usage. Null motion is added in the direction of maximum decrease in cost per change in joint angle, steering the system through states that locally minimize power. This method differs from optimal design strategies or methods that generate time-optimal trajectories for a planned end-effector path. This study concentrates on a method for real-time, power-optimal control in which the future end-effector path of a robotic system is unknown. Instantaneous control is arguably more relevant for applications with significant uncertainties and moving targets than is path planning.

As mentioned in Section 1.2.3, null-motion algorithms have been studied in the context of CMG singularity avoidance. The CMG steering problem involves determining the gimbal rates that achieve a commanded output torque while sat-

isfying certain constraints, particularly avoiding singular configurations. Here, null-motion algorithms minimize power in the multi-body robotic system rather than steering around internal CMG singularities. The CMG singularity problem is addressed by arranging the CMGs into scissored pairs, as in the previous chapters. Section 4.2 briefly reviews the overall system architecture. Section 4.3 describes the problem and discusses the kinematic relationships between end-effector attitude coordinates and joint coordinates. Sections 4.4 and 4.5 review the dynamics analysis and feedback-control strategy for the proposed system that was first introduced in Chapter 2. Section 4.6 details the power-optimization algorithm, and Section 4.7 presents a numerical study comparing simulations with varying amounts of null motion to a simulation in which the algorithm is not used. Reference [7] provides preliminary numerical results for this study. This chapter includes additional analysis for deriving the system power and results that use the updated power cost.

4.2 System Concept

This study investigates the three-link, CMG-actuated robot arm described in Chapter 2 modified with a camera mounted on the outer arm segment. Each arm segment contains mirrors that reflect light from the camera through a Coudé path onto the focal plane. Again, since minimizing vibration induced by base reactions is an important design goal for an imaging payload, we consider a special case where the base is stationary, thanks to an on-board ACS, and where the system inertia dyadic is constant in an inertial frame. Section 2.2 contains the full description of the system, along with illustrations in Figs. 2.1 - 2.2 for the system concept and the arrangement of the CMG scissored pairs on the arm segments. The mass center of each mass-balanced link is located on the inner link's joint

axis. Each link's mass center is stationary during body rotations, implying that the system mass center is also stationary during body rotations. These conditions eliminate reaction forces and force-induced torques on the spacecraft bus.

4.3 Direct and Inverse Kinematics

The reference configuration illustrated in Fig. 2.3 is revisited for this study. The camera fixed to the outer link has a boresight unit vector, $\mathbf{b}$, indicating its pointing direction, which is shown in Fig. 4.1.

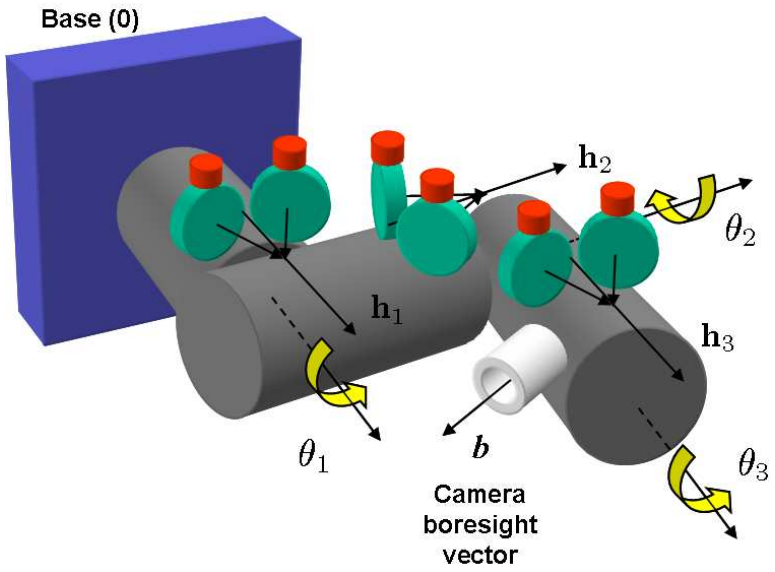

Figure 4.1: Scissored-pair implementation on a three-degree-of-freedom robotic payload.

The boresight vector is fixed in the outer arm segment so that it is not always parallel to one of the joint axes in a singular configuration. The general transformation from the body j-fixed coordinate system to the body-i-fixed coordinate system is given by Eq. (2.5). With the defined reference configuration, the direction-

cosine matrices described by Eq. (2.5) are used to transform all defined vectors and dyadics to inertial coordinates. In body-3-fixed coordinates, the boresight direction is ${}^3b = [\frac{\sqrt{2}}{2}, \frac{\sqrt{2}}{2}, 0]^{\mathrm{T}}$. In inertial coordinates, the boresight direction is

$$ {}^0b = \frac{\sqrt{2}}{2} \begin{bmatrix} \sin\theta_1 \sin\theta_2 - \cos\theta_1 \cos\theta_3 - \sin\theta_1 \cos\theta_2 \sin\theta_3 \\ \cos\theta_2 + \sin\theta_2 \sin\theta_3 \\ \cos\theta_1 \cos\theta_2 \sin\theta_3 - \cos\theta_1 \sin\theta_2 - \sin\theta_1 \cos\theta_3 \end{bmatrix}. \tag{4.1} $$

The boresight attitude is also expressed in terms of coordinates $\alpha_1 \in [0, \pi]$ and $\alpha_2 \in [0, 2\pi]$, which are measured from $\hat{\mathbf{e}}_{03}$ and $\hat{\mathbf{e}}_{01}$, respectively. These coordinates are shown in Fig. 4.2. Since $\mathbf{b} \in \mathbb{R}^2$, there are many joint configurations for the proposed three-degree-of-freedom system that correspond to a given boresight attitude command. The goal of this study is to find the solution to the tracking problem that minimizes the power due to torquing the gimbals. According to Fig. 4.2, the boresight attitude in inertial coordinates in terms of α_1 and α_2 is

$$ \begin{bmatrix} {}^0b_1 \\ {}^0b_2 \\ {}^0b_3 \end{bmatrix} = \begin{bmatrix} \sin\alpha_1 \cos\alpha_2 \\ \sin\alpha_1 \sin\alpha_2 \\ \cos\alpha_1 \end{bmatrix}. \tag{4.2} $$

From Eq. (4.2), an unambiguous solution α_j is found via the four-quadrant arctangent:

$$ \alpha_1 = \tan^{-1}\left(\frac{\sqrt{{}^0b_1^2 + {}^0b_2^2}}{{}^0b_3} \right) \tag{4.3} $$

$$ \alpha_2 = \tan^{-1}\left(\frac{{}^0b_2}{{}^0b_1} \right). \tag{4.4} $$

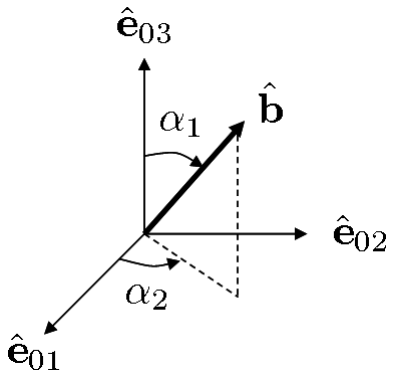

Figure 4.2: Boresight attitude coordinate system.

For tracking a boresight attitude command in closed loop, the controlled degrees of freedom are the relative joint angles, θ_i. A general N-degree-of-freedom system consisting of N linked bodies requires inverse-kinematic solutions to the nonlinear equations

$$\alpha_j = f(\theta_i), \tag{4.5}$$

where $i = \{1, ..., N\}$ and $j = \{1, ..., M\}, M < N$. The positional inverse kinematics are ideally performed with a linear transformation from the joint angles, θ_i, to attitude coordinates, α_j. In this case, an analytical representation of this Jacobian is not possible because the relationship between these quantities is nonlinear. An alternative approach is to numerically solve the system of nonlinear equations formed by equating Eqs. (4.1) and (4.2). However, searching for the roots of this system involves the use of nonlinear optimization algorithms that are not only computationally expensive for a real-time application, but are also likely to yield infeasible joint-angle solutions. A more direct approach involves using the differential relationship between the joint angles and boresight coordinates:

$$\delta\alpha_j = \sum_{i=1}^{N} \frac{\partial \alpha_j}{\partial \theta_i} \delta\theta_i, \tag{4.6}$$

or more compactly,

$$\delta\alpha = K(\theta_i)\delta\Theta, \tag{4.7}$$

where $\delta\alpha \in \mathbb{R}^{M\times 1}$ contains the differential boresight coordinates, and $\delta\Theta \in \mathbb{R}^{N\times 1}$ contains the differential joint angles. The differential position Jacobian $K \in \mathbb{R}^{M\times N}$ relates the boresight coordinate error, $\delta\alpha$, to joint-angle error, $\delta\theta$, which is eventually included in a feedback loop. The elements of K are computed numerically by first subjecting nominal joint angles $\theta_{i,\text{nom}}$ to small perturbations $\delta\theta_i$, and substituting these perturbed joint angles $\theta_i = \theta_{i,\text{nom}} + \delta\theta_i$ into Eq. (4.1). The resulting ${}^0b_i$ are used to find the perturbed coordinates, α_j, with Eqs. (4.3)-(4.4). The elements of K, k_{ji}, are therefore approximated with

$$k_{ji} = \frac{\partial \alpha_j}{\partial \theta_i} \approx \frac{\alpha_j - \alpha_{j,\text{nom}}}{\delta\theta_i}, \tag{4.8}$$

where $\alpha_{j,\text{nom}}$ are the nominal boresight coordinates. This approximation remains valid for steps in α_j that are sufficiently small.

Unlike the positional inverse-kinematics problem, the velocity inverse-kinematics problem has an analytical solution. The relation is given by

$$\dot{\alpha}_j = \sum_{i=1}^{N} \frac{\partial \dot{\alpha}_j}{\partial \dot{\theta}_i} \dot{\theta}_i, \tag{4.9}$$

more compactly expressed as

$$\dot{\alpha} = H(\theta_i)\dot{\Theta}, \tag{4.10}$$

where $\dot{\alpha} \in \mathbb{R}^{M\times 1}$ contains the boresight attitude rates, $\dot{\Theta} \in \mathbb{R}^{N\times 1}$ contains the joint rates, and $H(\theta_i) \in \mathbb{R}^{M\times N}$ is the Jacobian relating these quantities. This transformation is analytically derived using the chain rule, where the elements of H are

$$h_{ji} = \frac{\partial \dot{\alpha}_j}{\partial \dot{\theta}_i} = \frac{\partial \dot{\alpha}_j}{\partial {}^0\dot{b}_k} \cdot \frac{\partial {}^0\dot{b}_k}{\partial \dot{\theta}_i} = g_{ji} \cdot p_{ji}. \tag{4.11}$$

Therefore, H is

$$H(\theta_i) = G({}^0b_i) \cdot P(\theta_i), \tag{4.12}$$

where g_{ji} are elements of $G({}^0b_i) \in \mathbb{R}^{M\times N}$ that relate the components of ${}^0\dot{b}$ to the boresight attitude rates, $\dot{\alpha}_j$, and p_{ji} are elements of $P(\theta_i) \in \mathbb{R}^{N\times N}$ that relate the joint rates to the components of ${}^0\dot{b}$. Since $\mathbf{b}$ is a constant-length unit vector, its time rate of change is

$$\dot{\mathbf{b}} = \boldsymbol{\omega}^{3/0} \times \mathbf{b}, \tag{4.13}$$

where $\boldsymbol{\omega}^{i/j}$ is the angular velocity of frame i relative to frame j. After expressing $\dot{\mathbf{b}}$ in inertial coordinates, the elements of $G({}^0b_i)$ and $P(\theta_i)$ can be determined. The elements of $G({}^0b_i)$ and $P(\theta_i)$ are provided in Appendix B. The unit-length constraint on the boresight attitude vector ensures that $P(\theta_i)$ is always singular in the

boresight direction. Equivalently, $\mathbf{b}$ can change only in a direction perpendicular to its orientation, as stated in Eq. (4.13).

4.4 System Dynamics

This study optimizes power for the proposed agile imaging payload in Chapter 2. It was shown in Section 2.3 that the total torque for a system consisting of N linked bodies about the system mass center is the time derivative of the total angular momentum in an inertial frame, 0:

$$\begin{aligned}\frac{^0d}{dt}\mathbf{H} \;=\; \sum_{i=1}^{N}\frac{^0d}{dt}\mathbf{H}_i = \sum_{i=1}^{N}\Big[&\mathbf{I}_{i\mathrm{C}}\cdot\frac{^id}{dt}\boldsymbol{\omega}^{i/0}+\boldsymbol{\omega}^{i/0}\times\big(\mathbf{I}_{i\mathrm{C}}\cdot\boldsymbol{\omega}^{i/0}\big)+\mathbf{R}_i\times m_{i\mathrm{C}}\mathbf{A}_i\\ &+2h_i\big(-\dot{\phi}_i\sin\phi_i\hat{\mathbf{e}}_{i1}+\boldsymbol{\omega}^{i/0}\times\cos\phi_i\hat{\mathbf{e}}_{i1}\big)\Big].\end{aligned} \tag{2.15}$$

In Eq. (2.15), $\mathbf{H}_i$ is the angular momentum of body i about the system mass center, $\mathbf{I}_{i\mathrm{C}}$ is the composite inertia dyadic about the mass center for the ith arm segment-CMG scissored pair combination, and h_i is the rotor angular-momentum magnitude of either CMG in the scissored pair fixed to body i.

A reactionless system is of interest for this study because 1) minimizing base reactions is a reasonable design goal for a precision optical payload, and 2) the assumption allows analysis of the optimization effects without the burden of additional complications in the dynamics. For a reactionless system, the total inertia dyadic is constant in an inertial frame and there is a frictionless contact between the payload and the base. In the case of a fixed base, a mass-balanced payload's

mass center does not translate during robotic maneuvers. Finally, there are constraint torques acting between each joint, but they do no work on the system. Therefore, with purely internal torques, the total angular momentum is conserved about the mass center and Kane's method yields the equations of motion

$$\sum_{i=1}^{N}\left(\frac{^0d}{dt}\mathbf{H}_i\cdot\frac{\partial\boldsymbol{\omega}_i}{\partial\dot{q}_j}\right)=0, \tag{2.21}$$

where the generalized coordinates, q_j, and generalized speeds, $\dot{q}_j$, are the relative angular positions and rates of the bodies, respectively. $\boldsymbol{\omega}_i$ is the angular velocity of body i in an inertial frame. The matrix representation of the system equations of motion is given by Eq. (2.24).

In order to determine the effects of the optimization algorithm on power efficiency, an expression is derived for the total system energy and power. As stated in Chapter 2, the total energy is

$$\begin{aligned} E &= \frac{1}{2}\sum_{i=1}^{N}\Bigg\{(\boldsymbol{\omega}^{i/0}\cdot\mathbf{I}_i\cdot\boldsymbol{\omega}^{i/0})+\sum_{j=1}^{S}\Big[(\boldsymbol{\omega}^{\mathrm{G}_{ij}/0}\cdot\mathbf{I}_{\mathrm{G}_{ij}}\cdot\boldsymbol{\omega}^{\mathrm{G}_{ij}/0}) \\ &\quad +(\boldsymbol{\omega}^{\mathrm{R}_{ij}/0}\cdot\mathbf{I}_{\mathrm{R}_{ij}}\cdot\boldsymbol{\omega}^{\mathrm{R}_{ij}/0})\Big]\Bigg\}, \end{aligned} \tag{2.22}$$

where N is the number of arm segments in the system and S is the number of CMGs on each body. For the proposed system, $N=3$ and $S=2$. $\mathbf{I}_i$ is the central inertia dyadic of the ith arm segment without the CMGs. $\mathbf{I}_{\mathrm{G}_{ij}}$ is the central inertia dyadic of the jth CMG gimbal on body i and $\mathbf{I}_{\mathrm{R}_{ij}}$ is the central inertia dyadic of the jth CMG rotor on body i. G_{ij} and R_{ij} also represent the jth gimbal-fixed frame

on body i and the jth rotor-fixed frame on body i, respectively. Since the CMGs in a scissored pair are identical, Eq. (2.22) can be further simplified by letting $\mathbf{I}_{\mathrm{R}_{i1}} = \mathbf{I}_{\mathrm{R}_{i2}} = \mathbf{I}_{\mathrm{R}}$ and $\mathbf{I}_{\mathrm{G}_{i1}} = \mathbf{I}_{\mathrm{G}_{i2}} = \mathbf{I}_{\mathrm{G}}$. The system mass center is stationary during slews, so there are no translational terms in Eq. (2.22). The total energy depends on the pure rotation of each system component.

The system power, or rate of change of kinetic energy, is found by differentiating Eq. (2.22), or by applying the Work-Energy Rate principle [96]. The power supplied to the system by each CMG gimbal is

$$P_{\mathrm{G}_{ij}} = \boldsymbol{\tau}_{\mathrm{G}_{ij}} \cdot \boldsymbol{\omega}^{\mathrm{G}_{ij}/i}, \tag{4.14}$$

where the jth CMG on body i applies the torque, $\boldsymbol{\tau}_{\mathrm{G}_{ij}}$, to body i:

$$\boldsymbol{\tau}_{\mathrm{G}_{ij}} = \left(\left[(\mathbf{I}_{\mathrm{R}} + \mathbf{I}_{\mathrm{G}}) \cdot \frac{^{\mathrm{G}_{ij}}d}{dt} \boldsymbol{\omega}^{\mathrm{G}_{ij}/0} \right] \cdot \hat{\mathbf{e}}_{i3} \right) \hat{\mathbf{e}}_{i3}. \tag{4.15}$$

In Eq. (4.15), $^{\mathrm{G}_{ij}}d/dt$ is the time derivative in the G_{ij} frame. The total instantaneous system power is therefore the sum of the $P_{\mathrm{G}_{ij}}$ in Eq. (4.14). However, as described in Chapters 2 and 3, negative values of power indicate energy recovered from the motion of the connected system components. The system of interest here is not designed to regeneratively recover energy, and the total power consumption is approximated by the sum of absolute values of kinetic-energy change for each gimbal. This non-recoverable power, P, is

$$P = \sum_{i=1}^{N} \sum_{j=1}^{S} \left| P_{\mathrm{G}_{ij}} \right| = \sum_{i=1}^{N} \sum_{j=1}^{S} \left| \boldsymbol{\tau}_{\mathrm{G}_{ij}} \cdot \boldsymbol{\omega}^{\mathrm{G}_{ij}/i} \right|. \tag{4.16}$$

Considering only the torque on each gimbal to determine the system power is an alternative approach to differentiating the system energy. This approach is chosen for this study because it is straightforward to develop a related cost function. The cost function is further discussed in Section 4.5.

4.5 Power-Optimization Algorithm and Implementation

To perform the optimization in real time throughout the maneuver, null motion is incorporated into the PD feedback-control law Eq. (3.19) for the gimbal rates. More capable control may be possible through the use of nonlinear control methods and the algorithm described in this section can be incorporated into alternative control architectures. In this chapter, the simple law in Eq. (3.19) is used for expediency in demonstrating the power-minimization approach.

Steering of a robotic linkage is considered optimal in terms of some cost function. While minimization of the total gimbal power in Eq. (4.16) is the objective of this study, a gradient-descent approach is presented in this section that requires the cost function to be continuous and differentiable everywhere with respect to each joint angle. We therefore define a quadratic cost, J, which is the sum of the squares of power for each gimbal in the system:

$$J = \sum_{i=1}^{N} \sum_{j=1}^{S} \left(P_{\mathrm{G}_{ij}} \right)^2 = \sum_{i=1}^{N} \sum_{j=1}^{S} \left(\boldsymbol{\tau}_{\mathrm{G}_{ij}} \cdot \boldsymbol{\omega}^{\mathrm{G}_{ij}/i} \right)^2 . \tag{4.17}$$

Section 2.3 discussed the significant amount of power required to enforce a constant-speed rotor constraint in a control loop when power is calculated with Eq. (2.23). The rotor speed in an inertial frame is not exactly constant because

the rates of the underlying system components have nonzero projections onto the rotor spin axis. However, since the joint rates are on the order of a radian per second and the rotor speed, Ω_{R}, is 200 rad/s for the numerical simulations in this dissertation, the inertial rotor speeds in Chapters 2 and 3 are accurate to within 1%. The same numerical results in Section 4.6 for non-recoverable power using Eq. (2.23) are obtained by implementing low-bandwidth control of the rotor motors. However, if the terms in Eq. (2.23) are squared in the same manner as Eq. (4.17) to define a quadratic cost function, the majority of that cost value would represent the power required to maintain constant rotor speeds. Since this study considers the case where no torque is required to enforce this constraint, it does not factor into the system power nor the cost function.

In the first step of the optimization algorithm, the gradient of the cost with respect to θ_i is calculated to determine the cost's sensitivity to each joint angle. The joint angles are continually adjusted by a small amount in the direction that yields the greatest decrease in cost, and this motion is projected onto the null space of K so that the boresight tracking is unaffected when including these adjustments in the joint-angle command. However, J is independent of the relative angular position of the innermost body, θ_1, since the innermost joint axis is stationary. In Section 3.3, it was shown that the generalized coordinate associated with a stationary joint axis is cyclic. Since the system Lagrangian is independent of the cyclic coordinate θ_1, the time derivative of this Lagrangian, i.e., the system power, is also independent of θ_1.

The joint-angle change required to reduce the cost to zero is

$$\delta\Theta_J = \Delta^{\dagger} J, \tag{4.18}$$

where $\Delta \in \mathbb{R}^{1\times N}$ contains the partial derivatives of J with respect to each joint angle, and $\Delta^{\dagger} \in \mathbb{R}^{N\times 1}$ is the pseudoinverse of Δ. Since $\text{rank}(\Delta) = 1$ with a single linearly independent row, the pseudoinverse of Δ is

$$\Delta^{\dagger} = \Delta^{\mathrm{T}}(||\Delta||^2 + \epsilon)^{-1}, \tag{4.19}$$

where $\epsilon \in \mathbb{R}$ is a small positive scalar that makes the pseudoinverse singularity robust. While the addition of ϵ in Eq. (4.19) yields only approximate pseudoinverse solutions, feasible solutions are possible in the neighborhood of singular points. The magnitude of $\Delta^{\dagger}$ decreases with larger values of ϵ. This decrease leads to smaller null projections of $\delta\Theta_J$, which implies reduced null motion for power optimization; however, larger values of ϵ can provide greater robustness near singularities in $\Delta^{\dagger}$. This approach is the singularity-robust (SR) inverse method that was discussed in Section 1.2.3. A more complicated version of Eq. (4.19) was originally investigated, in which ϵ is a function of the distance to a singularity. A manipulability measure, w, indicates this distance:

$$w = \sqrt{det(||\Delta||^2)}. \tag{4.20}$$

ϵ is adjusted according to

$$\epsilon \quad = \quad \begin{cases} k_0(1 - w/w_0)^2 & w < w_0 \\ 0 & w \geq w_0 \end{cases}$$

where w_0 is a defined neighborhood boundary of singular points and k_0 is a defined scale factor at these points [47]. Since using this algorithm does not generate a

noticeable difference in the simulation results, ϵ is defined to be simply a small constant to save computational effort.

Changing the joint-angle command does not introduce additional tracking error because the power-optimizing joint-angle change is projected onto a unit vector in $\mathbb{R}^{N\times 1}$ that spans the null space of K, $n_K \in \mathcal{N}(K)$. The null component of the joint-angle error is

$$\delta\Theta_{\mathrm{n}} = \big(\delta\Theta_J \cdot n_K\big) n_K. \tag{4.21}$$

The total joint-angle error when tracking the prescribed boresight attitude is therefore the sum of two parts, one given by the pseudoinverse solution of Eq. (4.7) and the other by the null component in Eq. (4.21), which is scaled by a gain, $q \in \mathbb{R}$:

$$\delta\Theta_{\mathrm{tot}} = K^{\dagger}\delta\alpha + q(\delta\Theta_{\mathrm{n}}). \tag{4.22}$$

$\delta\Theta_{\mathrm{tot}} \in \mathbb{R}^{N\times 1}$ in Eq. (4.22) is equal to $\Theta_{\mathrm{e}} = \Theta_{\mathrm{d}} - \Theta$ in Eq. (3.19). Although it is not possible to uniquely determine desired joint angles, $\Theta_{\mathrm{d}} \in \mathbb{R}^{N\times 1}$, from the boresight attitude command, $\alpha_{\mathrm{d}} \in \mathbb{R}^{M\times 1}$, the computation in Eq. (4.22) is equivalent to adding null motion to the joint-angle command, since

$$\begin{aligned} \delta\Theta_{\mathrm{tot}} &= \big[\Theta_{\mathrm{d}} + q(\delta\theta_{\mathrm{n}})\big] - \Theta \\ &= K^{\dagger}\delta\alpha + q(\delta\Theta_{\mathrm{n}}). \end{aligned} \tag{4.23}$$

Unlike the joint-angle error, the joint-rate error involves only the solution to Eq. (4.10) with no added null motion. Also, since there is a linear transformation

between the velocity coordinates, differential relationships do not need to be directly computed. The prescribed rate of change of boresight attitude, $\dot{\alpha}_{\mathrm{d}} \in \mathbb{R}^{M\times 1}$, is transformed to the desired joint rates contained in $\dot{\Theta}_{\mathrm{d}} \in \mathbb{R}^{N\times 1}$:

$$\dot{\Theta}_{\mathrm{d}} = H^{\dagger}\dot{\alpha}_{\mathrm{d}}, \tag{4.24}$$

which is then used to calculated the joint-rate error in Eq. (3.19), $\dot{\Theta}_{\mathrm{e}} = \dot{\Theta}_{\mathrm{d}} - \dot{\Theta}$.

To obtain the numerical results in Section 4.6, the gimbal jerks are numerically integrated strictly for the sake of implementation. According to Eq. (4.17), the cost function $J = J(\theta_i, \dot{\theta}_i, \ddot{\theta}_i, \phi_i, \dot{\phi}_i, \ddot{\phi}_i)$. Since the optimization algorithm minimizes the local power consumption (i.e., the cost function is evaluated at every simulation time step), joint and gimbal accelerations are needed to compute the cost function prior to the integration of the state derivative augmented with the null motion. The body jerks can be found analytically by differentiating the equations of motion in Eq. (2.24), but there are no analytical expressions for neither gimbal accelerations nor gimbal jerks. Finite differencing is therefore investigated for computing these variables. Backward differencing is specifically used, since central- and forward-differencing methods are not possible when approximating time derivatives. However, large oscillations appear in the gimbal accelerations when null motion is included in the control. The gimbal jerks are found by finite differencing the gimbal accelerations, which are themselves finite differences of the gimbal rates calculated in Eq. (3.19). Integrating gimbal jerks obtained in this manner leads to the undesirable oscillatory behavior of the gimbal accelerations.

Ultimately, the gimbal jerks are calculated with proportional control of the gimbal accelerations

$$\dddot{\Phi} = K_{\mathrm{p1}}(\ddot{\Phi}_{\mathrm{d}} - \ddot{\Phi}), \tag{4.25}$$

where $K_{\mathrm{p1}} \in \mathbb{R}^{N\times 1}$ is the proportional gain matrix for the gimbal-acceleration loop, $\dddot{\Phi} \in \mathbb{R}^{N\times 1}$ contains the gimbal jerks, $\ddot{\Phi}_{\mathrm{d}} \in \mathbb{R}^{N\times 1}$ contains the desired gimbal accelerations, and $\ddot{\Phi} \in \mathbb{R}^{N\times 1}$ contains the gimbal acceleration response. However, $\ddot{\Phi}_{\mathrm{d}}$ are in turn calculated by proportional control of the gimbal rates

$$\ddot{\Phi}_{\mathrm{d}} = K_{\mathrm{p2}}(\dot{\Phi}_{\mathrm{d}} - \dot{\Phi}), \tag{4.26}$$

where $K_{\mathrm{p2}} \in \mathbb{R}^{N\times 1}$ is the proportional gain matrix for the gimbal-rate loop, $\dot{\Phi}_{\mathrm{d}} \in \mathbb{R}^{N\times 1}$ contains the desired gimbal rates given by Eq. (3.19), and $\dot{\Phi} \in \mathbb{R}^{N\times 1}$ contains the gimbal-rate response. Substituting Eq. (4.26) into Eq. (4.25) yields an inner control loop for the gimbal jerks:

$$\dddot{\Phi} = K_1(\dot{\Phi}_{\mathrm{d}} - \dot{\Phi}) - K_2\ddot{\Phi}, \tag{4.27}$$

where $K_1 = K_{\mathrm{p1}}K_{\mathrm{p2}}$ and $K_2 = K_{\mathrm{p1}}$. The control gain K_2 corresponds to gimbal damping. While not commonly used in real-world systems, gimbal-jerk actuation can be physically realized by accelerating current through the gimbal motors. In this control design, the feedback for the gimbal jerks occurs at a frequency much higher than ω_{n} to ensure tracking accuracy for nonzero values of q. For the numerical example shown in Section 4.6, the gains for the inner gimbal-jerk control loop in Eq. (4.27) and for the gimbal-rate control loop in Eq. (3.19) are listed in Table 4.1.

The performance of the optimization algorithm is demonstrated for a demand-

Table 4.1: Gains for the Gimbal-Rate Control Loop and the Inner Gimbal-Jerk Control Loop.

Parameter	Value
Damping ratio, ζ	1
Natural frequency, ω_{n}	π rad/s
Gain for gimbal-rate loop, K_1	9.0e4
Gain for gimbal-acceleration damping, K_2	2.5e4

ing large-angle maneuver. The angular position, rate, and acceleration of each joint and gimbal are included in the state vector because they are required to compute J. A quintic polynomial is therefore defined with constraints on $\alpha_{j\mathrm{d}}$, $\dot{\alpha}_{j\mathrm{d}}$, and $\ddot{\alpha}_{j\mathrm{d}}$ to establish corresponding constraints on the initial and final state variables. The six constraint equations on the boresight attitude kinematics are

$$\begin{aligned}
\alpha_{j\mathrm{d}}(t_0) &= \alpha_{j0} \\
\alpha_{j\mathrm{d}}(t_\mathrm{f}) &= \alpha_{j\mathrm{f}} \\
\dot{\alpha}_{j\mathrm{d}}(t_0) &= \dot{\alpha}_{j0} \\
\dot{\alpha}_{j\mathrm{d}}(t_\mathrm{f}) &= \dot{\alpha}_{j\mathrm{f}} \\
\ddot{\alpha}_{j\mathrm{d}}(t_0) &= \ddot{\alpha}_{j0} \\
\ddot{\alpha}_{j\mathrm{d}}(t_\mathrm{f}) &= \ddot{\alpha}_{j\mathrm{f}}
\end{aligned} \tag{4.28}$$

These constraints uniquely specify a quintic polynomial. Each boresight attitude coordinate follows a trajectory of the form

$$\alpha_{j\mathrm{d}}(t) = a_0 + a_1 t + a_2 t^2 + a_3 t^3 + a_4 t^4 + a_5 t^5, \tag{4.29}$$

so that the rate and acceleration of each coordinate are

$$\begin{aligned} \dot{\alpha}_{j\mathrm{d}}(t) &= a_1 + 2a_2 t + 3a_3 t^2 + 4a_4 t^3 + 5a_5 t^4 & (4.30) \\ \ddot{\alpha}_{j\mathrm{d}}(t) &= 2a_2 + 6a_3 t + 12a_4 t^2 + 20a_5 t^3. & (4.31) \end{aligned}$$

Solving the following matrix equation yields the coefficients of the quintic polynomial, $\{a_0, a_1, a_2, a_3, a_4, a_5\}$:

$$\begin{bmatrix} \alpha_{j0} \\ \alpha_{j\mathrm{f}} \\ \dot{\alpha}_{j0} \\ \dot{\alpha}_{j\mathrm{f}} \\ \ddot{\alpha}_{j0} \\ \ddot{\alpha}_{j\mathrm{f}} \end{bmatrix} = \begin{bmatrix} 1 & t_0 & t_0^2 & t_0^3 & t_0^4 & t_0^5 \\ 1 & t_\mathrm{f} & t_\mathrm{f}^2 & t_\mathrm{f}^3 & t_\mathrm{f}^4 & t_\mathrm{f}^5 \\ 0 & 1 & 2t_0 & 3t_0^2 & 4t_0^3 & 5t_0^4 \\ 0 & 1 & 2t_\mathrm{f} & 3t_\mathrm{f}^2 & 4t_\mathrm{f}^3 & 5t_\mathrm{f}^4 \\ 0 & 0 & 2 & 6t_0 & 12t_0^2 & 20t_0^3 \\ 0 & 0 & 2 & 6t_\mathrm{f} & 12t_\mathrm{f}^2 & 20t_\mathrm{f}^3 \end{bmatrix} \begin{bmatrix} a_0 \\ a_1 \\ a_2 \\ a_3 \\ a_4 \\ a_5 \end{bmatrix}. \tag{4.32}$$

If the initial conditions are nonzero, then the initial body rates and accelerations are dependent on the initial gimbal angles and rates. The initial body accelerations can be calculated from the gimbal kinematics using the equations of motion. While the initial and final states yield a nonsingular initial and final pseudoinverse of Δ, simulation trials demonstrate that arbitrary constraints on the boresight attitude rates and accelerations do not guarantee a path free of joint-kinematic singularities. These joint-kinematic singularities, which are relevant to workspace performance, are distinct from CMG singularities, which are relevant to actuator performance.

To address the joint-kinematic singularity issue in this study, a nonsingular path is generated by holding the joint rates fixed in an open-loop simulation. The MATLAB® function **ode45.m** is used to integrate the equations of motion in Eq. (2.24) from $t_0 = 0$ s to $t_f = 100$ s. The periodic body kinematics from this open-loop maneuver are transformed to attitude coordinates and rates, α_j and $\dot{\alpha}_j$, and are used as the reference attitude trajectory for the closed-loop simulation. Figure 4.3 shows the desired boresight attitude coordinates and rates, $\alpha_{j\mathrm{d}}$ and $\dot{\alpha}_{j\mathrm{d}}$. The initial gimbal rates are computed with the control law in Eq. (3.19), where the initial errors in joint angles and rates are zero. The initial body accelerations are calculated from the gimbal angles and rates with Eq. (2.24). To find the initial gimbal accelerations, the control law in Eq. (3.19) is differentiated and the initial errors are assumed to be zero.

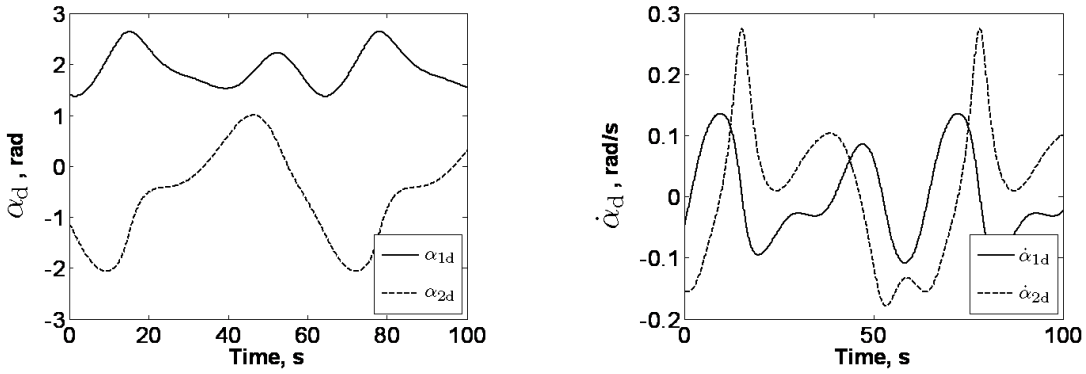

(a) Desired boresight attitude coordinates.

(b) Desired boresight attitude rates.

Figure 4.3: Nonsingular reference boresight trajectory.

Since the goal of this study is to indirectly optimize power through the controlled motion of the joints, the body kinematics are altered by adding a null component to the joint-angle command in the control. The cost function in Eq.

(4.17) is also influenced by the joint rates and accelerations, but the effect on the optimization of adding null components to other kinematic variables is unknown. In an earlier version of the optimization algorithm, null-rate components were also added to the joint-rate command in Eq. (3.19). However, preliminary simulation results indicated greater power improvements with null-angle components only. This outcome may be due to the choice of control strategy or to possible coupling effects between the null angles and null rates.

4.6 Simulation Results

For the large-angle slew in these simulations, Table 4.2 lists the key parameters. The rotor angular momentum of each CMG is based on that of the Honeywell M50 CMG [17]. The power model in the simulation does not account for rotor drag or losses in the gimbal motor, gear train, or drive electronics. The results reflect these omissions. In this demonstration, the proportional and derivative gains are the same for each body. It is assumed that the gimbals begin in a configuration for which the net angular momentum of each scissored pair is zero. This condition is satisfied when the rotor angular-momentum vectors are π radians apart from each other and perpendicular to the joint axis. Since the gimbal angles in this study are measured from the joint axis (see Fig. 2.2), the initial gimbal angles are $\pm\pi/2$ radians for each scissored pair. For fixed mass properties and initial conditions of the simulated system, the damping ratio and natural frequency in Table 4.2 are chosen such that the gimbal angles avoid saturation at 0 rad. In other words, the system does not perform slews that are too large or too fast for its CMGs. The initial relative body angles are arbitrary and nonsingular.

Table 4.2: Open-Loop Simulation Parameters for Generating a Nonsingular Reference Boresight Attitude Trajectory.

Parameter	Value
Initial relative body angles, $\theta_i(t_0)$	$(\pi, \frac{5\pi}{4}, \frac{23\pi}{12})$ rad
Initial relative body rates, $\dot{\theta}_i(t_0)$	(0.1, 0.02, 0.02) rad/s
CMG rotor angular momentum, h_i	50 N-m-s
Rotor spin speed, Ω_{R}	200 rad/s
Rotor inertia, I_{R}	0.25 kg-m^2
Gimbal inertia, I_{G}	0.125 kg-m^2
Body inertia, I_i	20 kg-m^2
Pseudoinverse constant, ϵ	0.01

With the parameters in Tables 4.1 and 4.2, the system is simulated for the case with no added null motion and for three different values of the null-motion gain, q. The tracking errors for α_1 and α_2 in Fig. 4.4 converge to zero as the system approaches open-loop behavior, while the body and gimbal kinematics that achieve this response are shown in Figs. 4.5 - 4.10. Although motion in null(K) theoretically results in no additional tracking error, unavoidable small deviations in the transient period, shown in Fig. 4.4, result from the added null motion. Nevertheless, the tracking error remains within reasonable bounds. Figure 4.11 shows the null components added to the joint-angle commands that minimize the cost.

The gimbal rates in Fig. 4.9 indicate that the same input can be tracked with reduced gimbal manipulation as more null motion is added. Since decreased gimbal rates directly result in less torque being imparted to the arm segments,

this result implies that the optimization may allow the system to achieve agile maneuvers that may not otherwise be possible. However, the gimbal-rate behavior in Fig. 4.9 implies a limit on the amount of added null motion before the gimbal accelerations exhibit undesirable behavior. In this numerical study, Fig. 4.10 shows potentially undesirable gimbal-acceleration behavior that occurs for $q > 0.1$. Cases for $q = 0.1, 0.15$ are shown to simply demonstrate the continued decrease in cost with increasing q.

A formal stability analysis is not performed in this study because a PD control law is used to control a nonlinear multi-body system. For a nonlinear system, asymptotic stability of the closed-loop system is guaranteed if a Lyapunov control law is implemented. However, with the control strategy in Eq. (3.19), the tools for linear-system stability analysis cannot be performed unless the nonlinear system is linearized about a nominal operating point.

Figure 4.12 shows the power usage during the maneuver, illustrating the quadratic cost, J, from Eq. (4.17), and non-recoverable power, P, from Eq. (4.16). The quantitative results from this comparison are summarized in Table 4.3. The time integral of non-recoverable power ($\int P dt$), time integral of the cost ($\int J dt$), power percentage improvement (PPI) and cost percentage improvement (CPI) are included. For the chosen values of q, this comparison shows a best-case 65.9% reduction in the time integral of the cost when null motion is incorporated. The time integral of non-recoverable power is reduced by up to 38.3% with the optimization. Each of these closed-loop maneuvers uses an arbitrary, nonsingular set of initial conditions. Arbitrary initial conditions allowed the system to experience an oscillatory transient at the beginning of the maneuver before settling into the periodic motion that the open-loop system would follow. The simulation results show that

the optimization algorithm is most effective during this initial transient motion, due to the fact that large control inputs during the transient period contain more null motion. When the system settles at around $t = 3$ s and the control inputs become increasingly small, the optimization effects become negligible. Figures 4.4 - 4.12 show only the first 4 s to emphasize the substantial effect of the optimization during the transient motion.

This maneuver can be performed with the gimbal-rate and gimbal-jerk control gains tuned for a faster transient response. For example, when the control gains are set to $\zeta = 0.707$, $\omega_{\mathrm{n}} = 6$ rad/s, $K_1 = 2000$, and $K_2 = 100$, the system responds with a settling time under 2 s without added null motion ($q = 0$), as exhibited in Fig. 4.13. However, since the power optimization is most pronounced with large control inputs, a longer settling time better showcases the benefits of optimization. The control gains in Table 4.1 intentionally yield a system response with extended transient motion and, consequently, a significant percentage improvement in power consumption.

4.7 Chapter Conclusions

This study demonstrates that the kinematics of a CMG-driven multi-body robotic system can be optimized so that power is reduced without path planning. In the case of a reactionless three-link imaging system, three joint degrees of freedom are simultaneously controlled to track a two-coordinate boresight attitude command while the bodies steer toward a power-optimal path. The optimization method includes the calculation of a cost function relating to the total gimbal power as a function of body and gimbal kinematics. The joint-angle change in the direction

of greatest decrease in cost is projected onto the null vector of the differential position Jacobian. This null projection is scaled and added to the joint-angle command for power minimization. Simulation results demonstrate that the null-motion algorithm yields the greatest improvements in cost and power for fast transient motions. Such a maneuver may be physically realized in the response of a CMG robotic system to instantaneous attitude commands. For a prescribed nonsingular maneuver, the best-case simulation results demonstrate a significant reduction of 38.3% in the integrated non-recoverable gimbal power when null motion is included in the control. Although potentially undesirable gimbal-acceleration behavior occurs for $q > 0.1$, the integrated non-recoverable power is still substantially reduced by 20.5% in the $q = 0.05$ case. For several values of the null-motion gain q, there is a clear trend toward improvement in power consumption with higher q. In addition, a decrease in gimbal rates with added null motion is shown, implying that this optimization may enable otherwise impossible motions given the capabilities of the CMGs.

Table 4.3: Summary of Optimization Results.

q	$\int Pdt$, J	$\int Jdt$, W^2-s	PPI	CPI
0	29.8	244.0	-	-
0.05	23.7	147.4	20.5%	39.6%
0.10	20.3	104.9	31.9%	57.0%
0.15	18.4	83.2	38.3%	65.9%

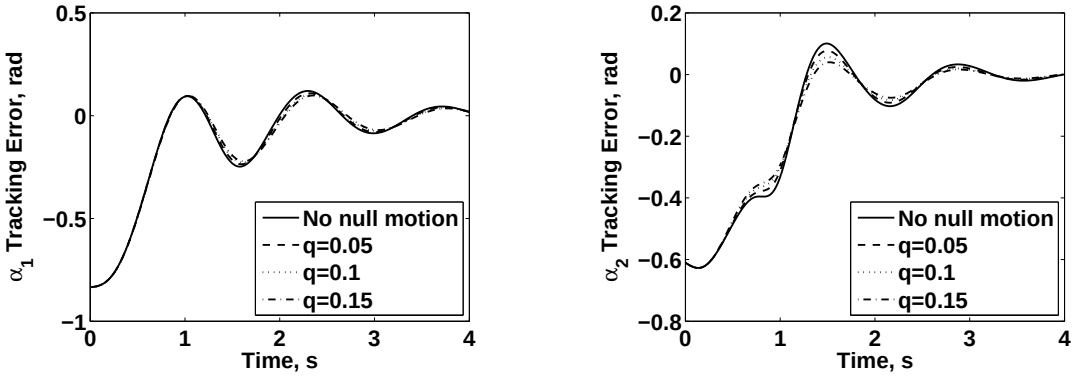

(a) α_1 error.

(b) α_2 error.

Figure 4.4: Boresight coordinate tracking errors with varying q.

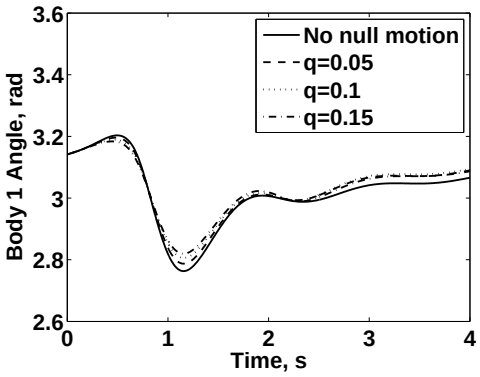

(a) Relative body 1 angle.

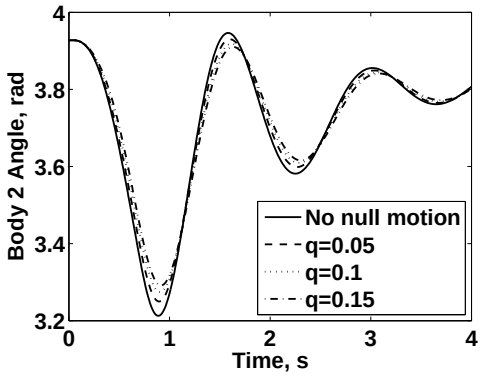

(b) Relative body 2 angle.

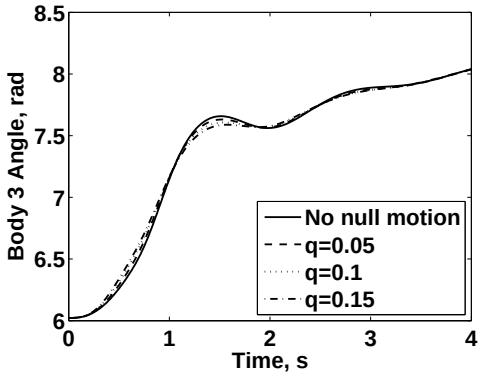

(c) Relative body 3 angle.

Figure 4.5: Relative body angles with varying q.

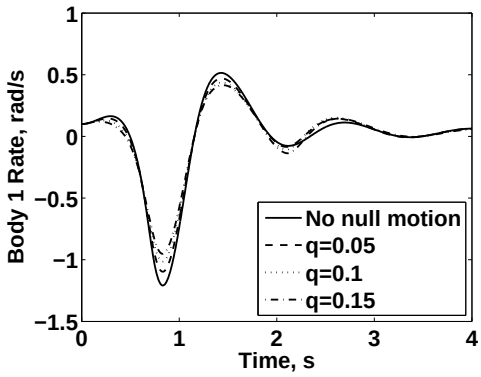

(a) Relative body 1 rate.

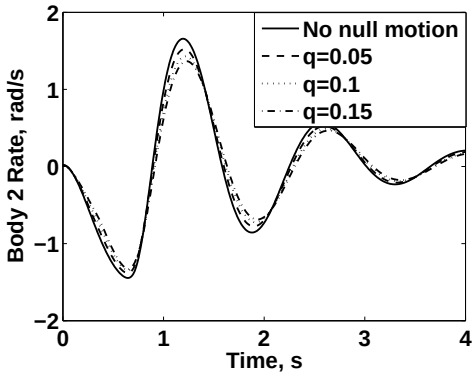

(b) Relative body 2 rate.

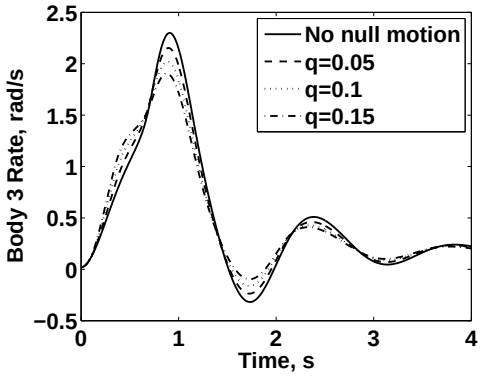

(c) Relative body 3 rate.

Figure 4.6: Relative body rates with varying q.

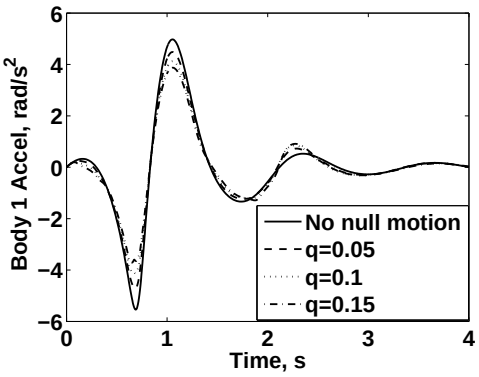

(a) Relative body 1 acceleration.

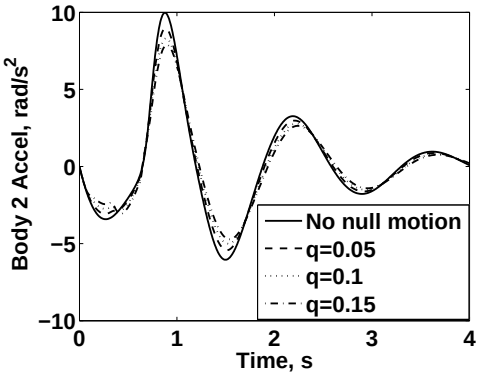

(b) Relative body 2 acceleration.

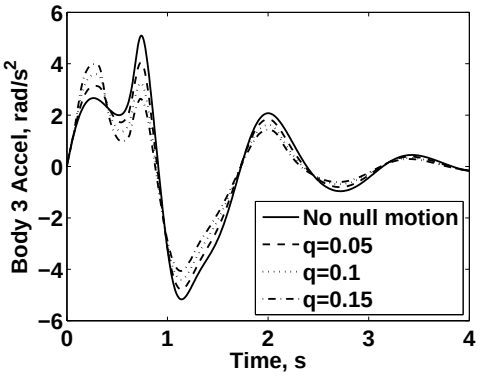

(c) Relative body 3 acceleration.

Figure 4.7: Relative body accelerations with varying q.

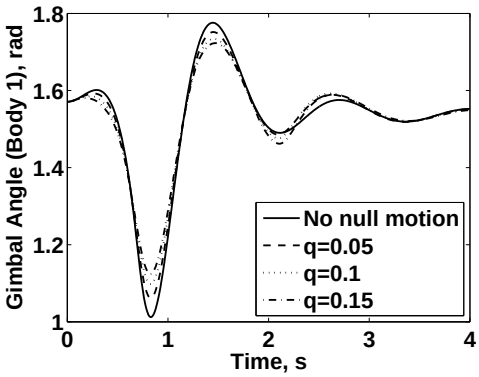

(a) Relative gimbal angle of CMGs on body 1.

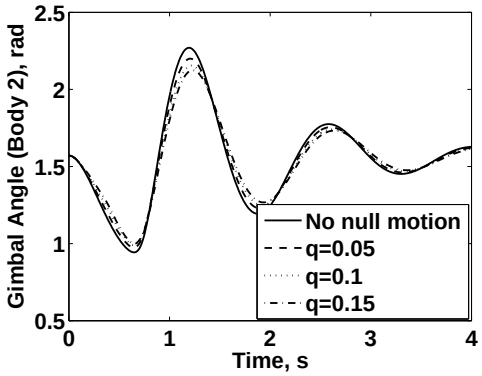

(b) Relative gimbal angle of CMGs on body 2.

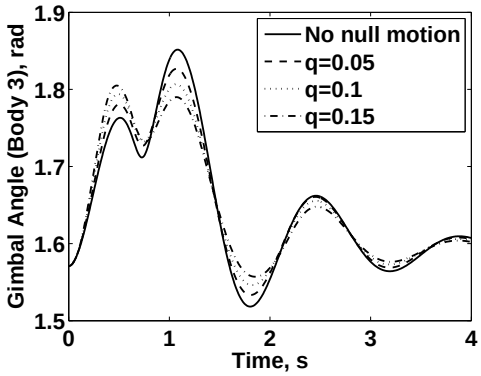

(c) Relative gimbal angle of CMGs on body 3.

Figure 4.8: Relative gimbal angles with varying q.

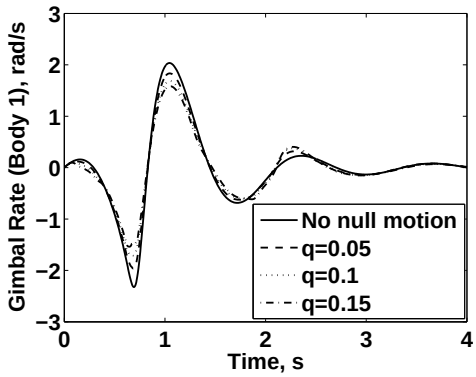

(a) Relative gimbal rate of CMGs on body 1.

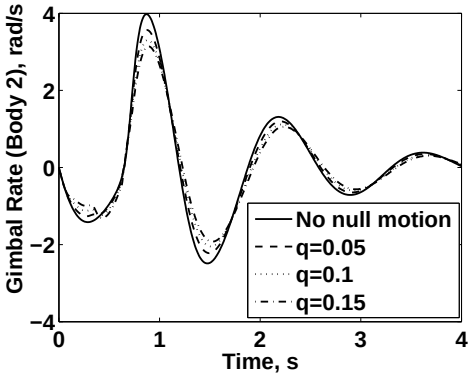

(b) Relative gimbal rate of CMGs on body 2.

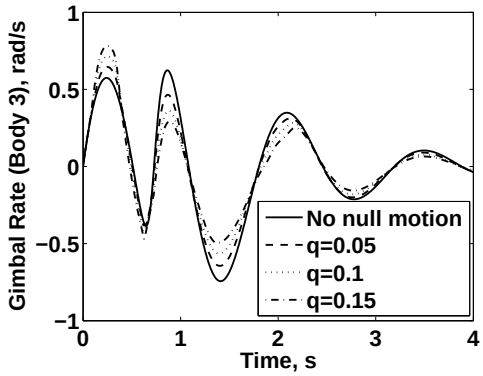

(c) Relative gimbal rate of CMGs on body 3.

Figure 4.9: Relative gimbal rates with varying q.

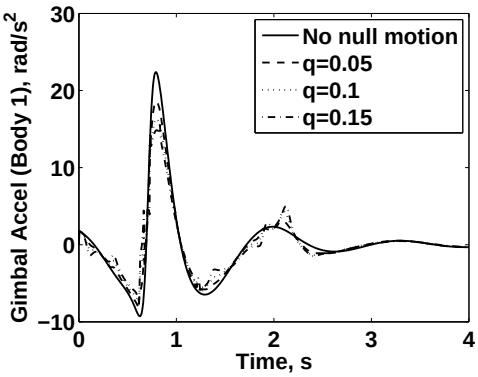

(a) Relative gimbal acceleration of CMGs on body 1.

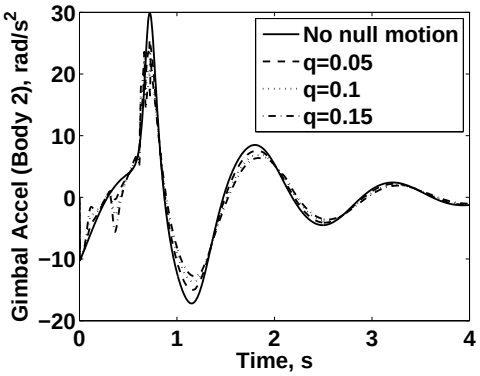

(b) Relative gimbal acceleration of CMGs on body 2.

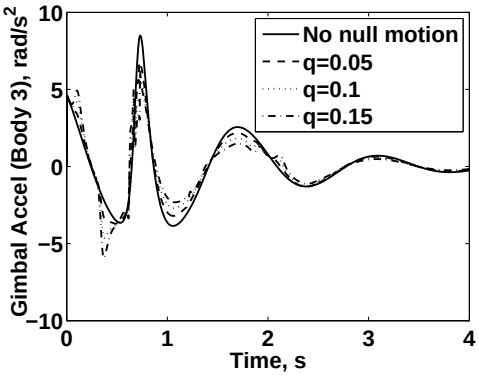

(c) Relative gimbal acceleration of CMGs on body 3.

Figure 4.10: Relative gimbal accelerations with varying q.

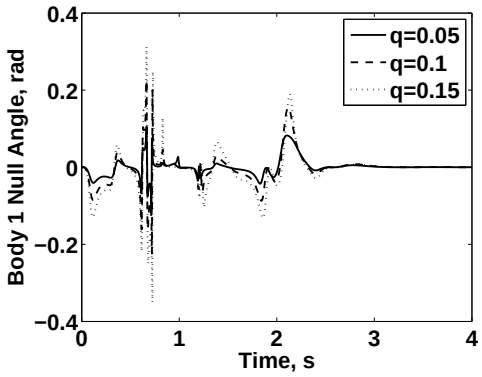

(a) Body 1 null-angle component.

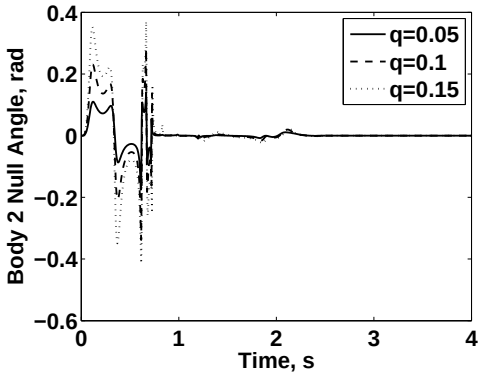

(b) Body 2 null-angle component.

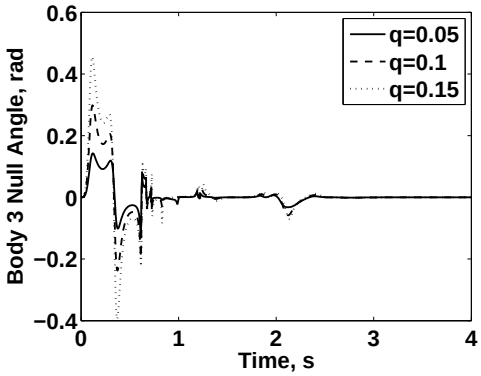

(c) Body 3 null-angle component.

Figure 4.11: Added null motion for power optimization.

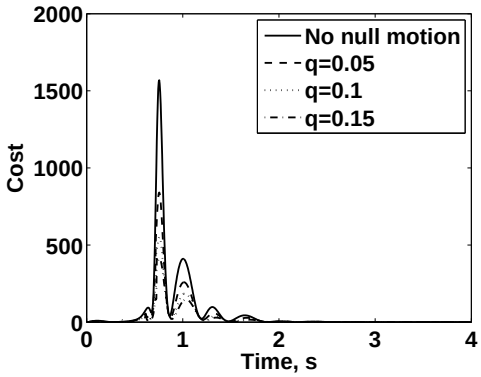

(a) Cost value.

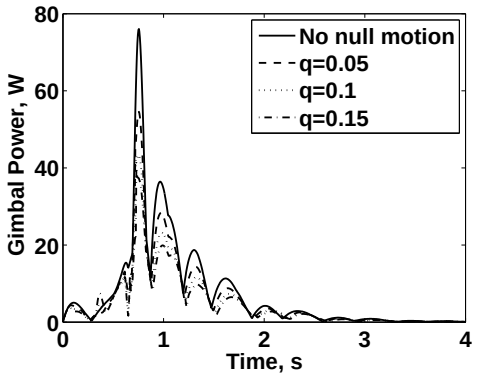

(b) System power.

Figure 4.12: Comparison of power usage with varying q as demonstrated by (a) the value of the cost function, and (b) the value of non-recoverable gimbal power.

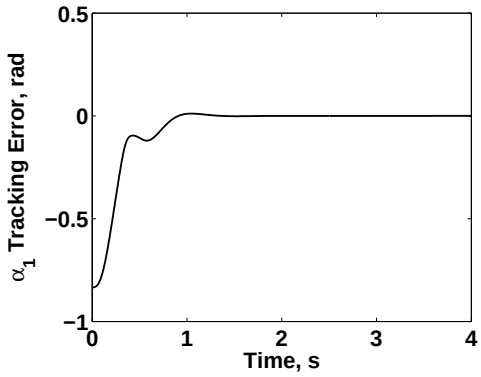

(a) α_1 error.

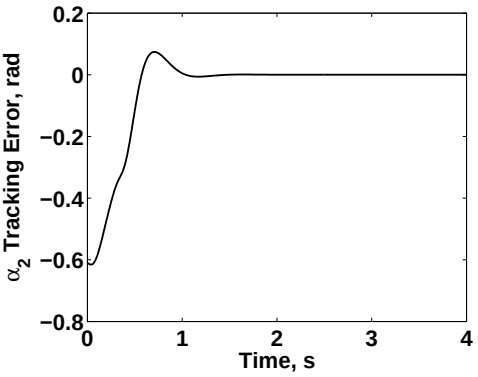

(b) α_2 error.

Figure 4.13: Boresight coordinate tracking error using example control gains for fast transient response.

CHAPTER 5

CONCLUSION

Control-moment gyroscopes (CMGs) have been examined as actuators for space-robotic systems. This dissertation develops the fundamental kinematics and dynamics for a general CMG robotic system with N arm segments, N degrees of freedom, arbitrary mass properties, and arbitrary joint axes. The equations of motion for a three-link system with orthogonal joint axes are incorporated into both open- and closed-loop control strategies for numerical studies. These numerical studies highlight the advantages of certain actuation methods and operations concepts, and demonstrate a strategy for power-optimal steering of a CMG-driven robot arm. This chapter summarizes the previous chapters with general conclusions and offers possible directions for future work in CMG space robotics.

5.1 Summary and Concluding Remarks

Combining the areas of CMG rigid-body control and multi-body dynamics enables new solutions for major issues in the field of space robotics. Key conclusions from the analytical and numerical studies of these systems include:

- In comparison to RWAs as actuators for reactionless payloads with high agility requirements, CMGs are far more power- efficient. In fact, the CMG system uses less than 1% of the power required to slew the RWA system in the same maneuver. Statistically, CMGs maximally outperform the RWA system when the arm-segment inertias are high and the torque imparted to the gimbal motors by the rotating arm segments is minimized. However, only

CMGs can generate the output torque necessary to perform the prescribed maneuver.

- Base reactions on a spacecraft due to robotic slewing are reduced or eliminated with internal momentum actuation. Since CMGs are the most power-efficient momentum-based actuators, and therefore the best option for actuating agile robotic systems, the base reactions of a CMG system are compared to those for a conventionally actuated system with identical mass properties. Numerical comparison studies of different operations concepts for the CMG system show that peak values for power, reaction-force magnitude, and reaction-torque magnitude can be reduced if the arm segments are sequentially rotated. However, the integrated values of these parameters are lower when the arm segments are simultaneously rotated.
- Power consumption is significantly reduced for a redundant robotic system tracking an end-effector attitude command by adding a null component to the joint-angle command in feedback. Even small amounts of added null motion can considerably reduce the total energy expended by lowering the peak gimbal rates.

CMG actuation provides many significant benefits for space robotics, including increased agility, substantially reduced power consumption and base reactions, and increased mission lifetime. In NASA's Vision for Space Exploration, there are crucial needs for technologies that enable in-orbit construction and repair. It is hoped that the studies presented here encourage the consideration of CMGs as a favorable architecture for high-agility space-robotics applications.

5.2 Recommendations for Future Work

Many directions for future work are possible in this area of research. First, this dissertation's approach in establishing the kinematics and dynamics of a CMG robotic system with an open-chain kinematic structure can be applied to robots with closed-chain topologies. Closed-chain robotic systems may prove useful in certain space-robotics applications, since they are claimed to have higher structural stiffness, lower positioning errors, and lower power requirements than open-chain systems [93]. This extension, along with the analysis presented here, may be used to develop an improved prototype CMG robotic arm useful for experimental comparisons of CMGs to other robotic actuators.

Experimental validation of the presented theoretical analysis for CMG robotic systems would be a highly useful extension of this dissertation. During the last several years, several student team projects have focused on designing and constructing a prototype CMG robotic arm for experimental data collection [97, 98]. Further discussion and a few images are included in Appendix A. The results in Chapter 2 provided a theoretical foundation in the development of these prototypes. The first arm, constructed in 2005-2006, was intended to provide a proof-of-concept for application in rehabilitation robotics. The second arm, developed during 2006-2007, was designed to mimic a space-robotic arm and tested aboard NASA's C-9 microgravity aircraft in 2007. Although this testbed was originally intended to experimentally compare CMGs to RWAs as actuators on a space-robotic arm, power readings from the electrical motors were ultimately collected for several slews with a planar joint configuration. However, the data quality did not facilitate proper data reduction and analysis. An improved prototype requires the prior development of a small-scale CMG with improvements in rotor stiffness and

bearing quality. Well-balanced CMG rotors on a new prototype will enable data collection that can validate the theoretical predictions for the low-jitter precision imaging applications discussed in Chapters 2 and 4.

Livingston *et al.* [99] are currently developing a two-segment, two-degree-of-freedom planar robotic linkage with both CMGs and conventional joint motors to experimentally determine which actuators are the most power-efficient for certain classes of maneuvers. Development of this testbed is based on parallel work by Brown [95], but it may also be used to verify the reduced base reactions and power expected for a CMG-actuated system, as demonstrated in Chapter 3, or the effectiveness of the power-optimization algorithm presented in Chapter 4.

Work in the area of on-line power optimization for a CMG system can be extended to include nonlinear control algorithms, including Lyapunov approaches, that may further improve the system's power efficiency. Additional extensions may involve modifying the optimization algorithm to include added null motion in the joint-rate and/or joint-acceleration commands, since power is also influenced by these quantities. Such a study may also be accompanied by an investigation of possible coupling effects between null-angle, null-rate, and null-acceleration components in the optimization results.

APPENDIX A

STUDENT DESIGN PROJECTS IN CMG ROBOTICS

Student design teams at Cornell have been involved in concurrent projects relevant to this dissertation. These projects include two prototype CMG robotic arms and the experimental demonstration of a new CMG control algorithm. Further details, images, and videos concerning the prototype robotic arms in this appendix can be found in [97].

The first prototype is a three-link, three-degree-of-freedom CMG-actuated robotic arm with application to low-power, upper-limb prosthetics [98]. This work proposes CMG actuation to meet reduced power requirements in rehabilitation robotics without sacrificing agility. Although originally intended to mimic a conventional prosthetic arm with hinged and rotational joints connecting human-arm sized links, design difficulties constrain the links to accommodate a feasible CMG design. The final design comprises three segments, each actuated by a single CMG scissored pair. Figure A.1 shows the completed prototype and its corresponding CAD model. Control inputs are generated by modeling an electromyogram (EMG) signal as a gimbal-angle versine path. Demonstration slews involve manipulating the CMGs via wireless radio control.

The second prototype is a two-link, two-degree-of-freedom CMG robot arm with parallel joint axes that is designed for application to space robotics. Figure A.2 shows the prototype along with its corresponding CAD model. Part (a) of Fig. A.2 shows the arm onboard NASA's C-9 aircraft for experimental testing in a microgravity environment. The objective of this study is to design a robotic arm with agility and power-consumption characteristics that improve those of current space robots using direct-drive actuation. Position control of the gimbals is achieved in

real time via a GUI interface on a connected laptop.

The last relevant student project is the Direct-Torque Actuator Control System (DTACS) experiment, which involves an experimental demonstration of a new CMG control algorithm. Historically, CMG steering laws command gimbal rates that cause the output torque applied to the base body to reproduce the commanded torque as accurately as possible. However, small-scale CMGs require small, precise angle and rate sensors that may be difficult to realize. Rather than using the gimbal-rate control inputs to indirectly control torque, the vector components of output torque are instead used as the control inputs. For the experimental setup illustrated in Fig. A.3, a CMG is connected to an enclosure for the gimbal motor/optical encoder and wiring harness. This enclosure is mounted directly onto a force/torque sensor that measures the vector components of force and torque. A function of the torque error is fed back to the controller, which manipulates the gimbal. The CMG gimbal motor is controlled via the dSPACE® real-time control environment.

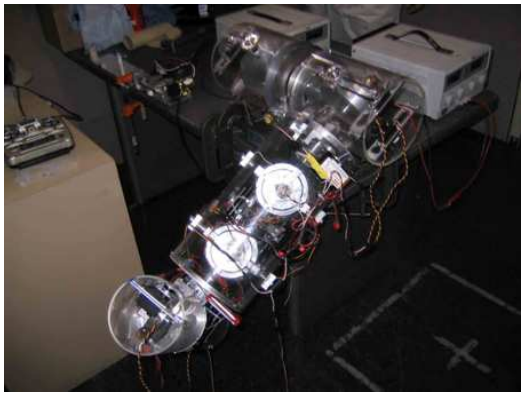

(a) Prototype.

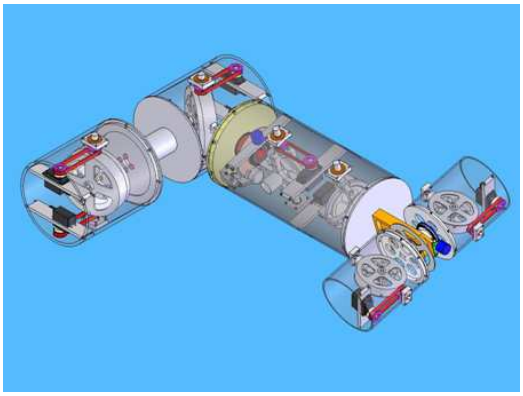

(b) CAD model.

Figure A.1: Three-link, three-degree-of-freedom CMG robotic arm with application to upper-limb prosthetics.

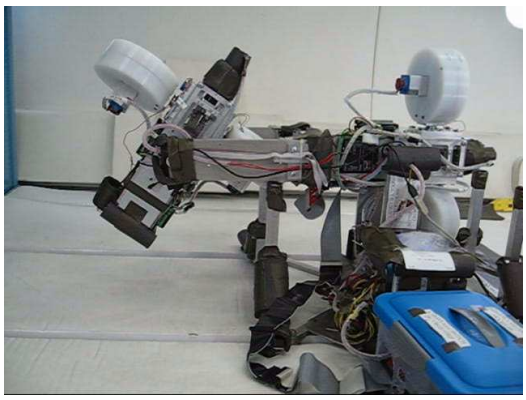

(a) Prototype.

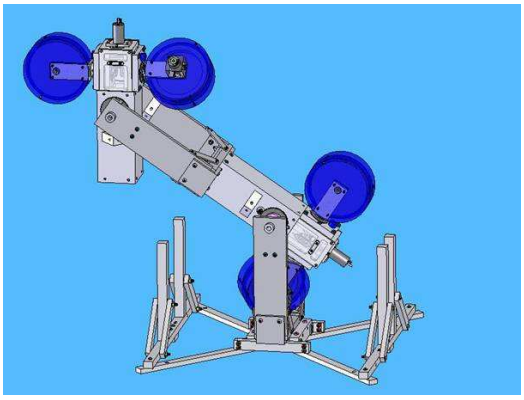

(b) CAD model.

Figure A.2: Two-link, two-degree-of-freedom CMG robotic arm with application to space robotics.

(a) Small-scale CMG and enclosure for gimbal motor/optical encoder and wiring harness.

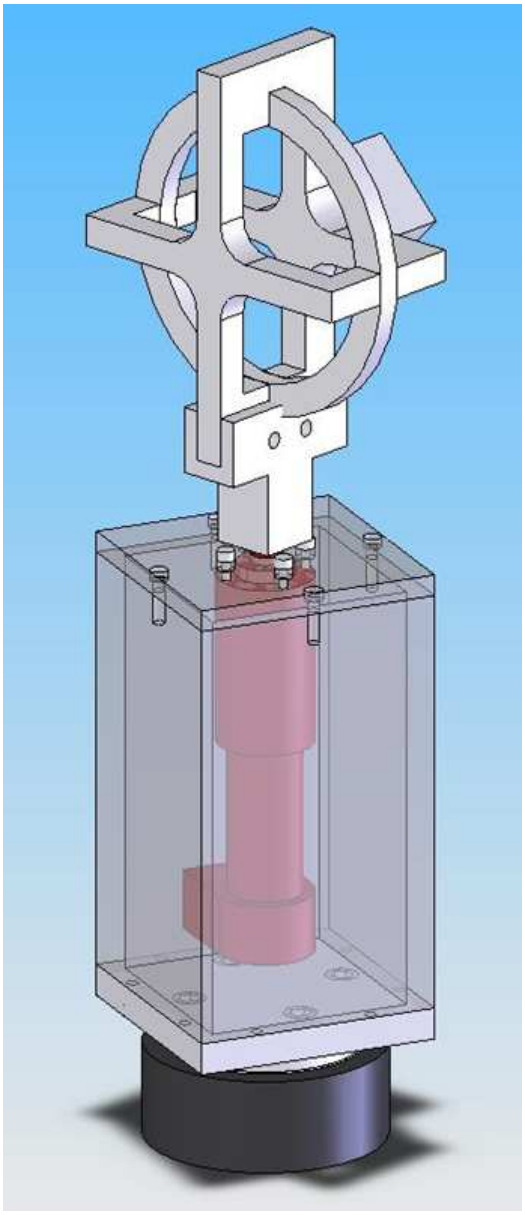

(b) CAD model for preliminary experimental setup.

Figure A.3: Preliminary DTACS experimental setup.

APPENDIX B

JACOBIAN ELEMENTS FOR KINEMATIC TRANSFORMATIONS

The linear transformation, $H(\theta_i)$, that relates the boresight attitude rates to the relative joint rates for the system described in Chapter 4 involves the analytical derivation of two velocity Jacobians, $G({}^0b_i)$ and $P(\theta_i)$. The Jacobian $G({}^0b_i)$ relates the components of $\dot{\mathbf{b}}$ in inertial coordinates to the boresight attitude rates, $\dot{\alpha}_j$. The boresight attitude rates are found by evaluating the time derivative of Eqs. (4.3)-(4.4):

$$\dot{\alpha}_1 = \frac{{}^0b_3\left({}^0b_1{}^0\dot{b}_1 + {}^0b_2{}^0\dot{b}_2\right) - {}^0\dot{b}_3\left({}^0b_1^2 + {}^0b_2^2\right)}{\sqrt{{}^0b_1^2 + {}^0b_2^2}} \tag{B.1}$$

$$\dot{\alpha}_2 = \frac{{}^0b_1{}^0\dot{b}_2 - {}^0\dot{b}_1{}^0b_2}{{}^0b_1^2 + {}^0b_2^2} \tag{B.2}$$

Equations (B.1)-(B.2) are then partially differentiated with respect to ${}^0\dot{b}_k$ to determine the elements, g_{ji}, of $G({}^0b_i)$:

$$\begin{aligned} g_{11} &= \frac{{}^0b_1{}^0b_3}{\sqrt{{}^0b_1^2 + {}^0b_2^2}} \\ g_{12} &= \frac{{}^0b_2{}^0b_3}{\sqrt{{}^0b_1^2 + {}^0b_2^2}} \\ g_{13} &= -\sqrt{{}^0b_1^2 + {}^0b_2^2} \\ g_{21} &= \frac{-{}^0b_2}{{}^0b_1^2 + {}^0b_2^2} \\ g_{22} &= \frac{{}^0b_1}{{}^0b_1^2 + {}^0b_2^2} \\ g_{23} &= 0 \end{aligned} \tag{B.3}$$

The Jacobian $P(\theta_i)$ relates the joint rates, $\dot{\theta}_j$, to the components of $\dot{\mathbf{b}}$ in inertial coordinates. These components, ${}^0\dot{b}_i$, are

$$
\begin{aligned}
{}^0\dot{b}_1 &= \frac{\sqrt{2}}{2}\Bigg\{\Bigg[\Big(\dot{\theta}_1 - \dot{\theta}_3\cos\theta_2\Big)\Big(\cos\theta_1\sin\theta_2 + \sin\theta_1\cos\theta_3 - \cos\theta_1\cos\theta_2\sin\theta_3\Big)\Bigg] \\
&\quad + \Bigg[\Big(\dot{\theta}_3\cos\theta_1\sin\theta_2 - \dot{\theta}_2\sin\theta_1\Big)\Big(\cos\theta_2 + \sin\theta_2\sin\theta_3\Big)\Bigg]\Bigg\} \qquad \text{(B.4)} \\
{}^0\dot{b}_2 &= \frac{\sqrt{2}}{2}\Bigg\{\Bigg[\Big(\dot{\theta}_3\cos\theta_1\sin\theta_2 - \dot{\theta}_2\sin\theta_1\Big)\Big(-\sin\theta_1\sin\theta_2 + \cos\theta_1\cos\theta_3 \\
&\quad + \sin\theta_1\cos\theta_2\sin\theta_3\Big)\Bigg] + \Bigg[\Big(\dot{\theta}_3\sin\theta_1\sin\theta_2 - \dot{\theta}_2\cos\theta_1\Big) \\
&\quad \Big(\cos\theta_1\sin\theta_2 + \sin\theta_1\cos\theta_3 - \cos\theta_1\cos\theta_2\sin\theta_3\Big)\Bigg]\Bigg\} \qquad \text{(B.5)} \\
{}^0\dot{b}_3 &= \frac{\sqrt{2}}{2}\Bigg\{\Bigg[\Big(\dot{\theta}_3\sin\theta_1\sin\theta_2 - \dot{\theta}_2\cos\theta_1\Big)\Big(\cos\theta_2 + \sin\theta_2\sin\theta_3\Big)\Bigg] \\
&\quad + \Bigg[\Big(\dot{\theta}_3\cos\theta_2 - \dot{\theta}_1\Big)\Big(-\sin\theta_1\sin\theta_2 + \cos\theta_1\cos\theta_3 + \sin\theta_1\cos\theta_2\sin\theta_3\Big)\Bigg]\Bigg\} \\
&\qquad \text{(B.6)}
\end{aligned}
$$

Equations (B.4)-(B.6) are partially differentiated with respect to the joint rates, $\dot{\theta}_j$, to find the elements, p_{ji}, of $P(\theta_i)$:

$$
\begin{aligned}
p_{11} &= \frac{\sqrt{2}}{2}(\cos\theta_1 \sin\theta_2 + \sin\theta_1 \cos\theta_3 - \cos\theta_1 \cos\theta_2 \sin\theta_3) \\
p_{12} &= \frac{\sqrt{2}}{2}\sin\theta_1(\cos\theta_2 + \sin\theta_2 \sin\theta_3) \\
p_{13} &= \frac{\sqrt{2}}{2}(\cos\theta_1 \sin\theta_3 - \sin\theta_1 \cos\theta_2 \cos\theta_3) \\
p_{21} &= 0 \\
p_{22} &= \frac{\sqrt{2}}{2}(\cos\theta_2 \sin\theta_3 - \sin\theta_2) \\
p_{23} &= \frac{\sqrt{2}}{2}\sin\theta_2 \cos\theta_3 \\
p_{31} &= \frac{\sqrt{2}}{2}(\sin\theta_1 \sin\theta_2 - \cos\theta_1 \cos\theta_3 - \sin\theta_1 \cos\theta_2 \sin\theta_3) \\
p_{32} &= -\frac{\sqrt{2}}{2}\cos\theta_1(\cos\theta_2 + \sin\theta_2 \sin\theta_3) \\
p_{33} &= \frac{\sqrt{2}}{2}(\sin\theta_1 \sin\theta_3 + \cos\theta_1 \cos\theta_2 \cos\theta_3)
\end{aligned} \tag{B.7}
$$

BIBLIOGRAPHY

[1] Billing-Ross, J. A. and Wilson, J. F., "Pointing System Design for Low-Disturbance Performance," *Proceedings of the AIAA Guidance, Navigation, and Control Conference*, No. 1988-4106, Minneapolis, Minnesota, Aug. 1988, pp. 444–451.

[2] Peck, M. A., Paluszek, M. A., Thomas, S. J., and Mueller, J. B., "Control-Moment Gyroscopes for Joint Actuation: A New Paradigm in Space Robotics," *Proceedings of the AIAA 1st Space Exploraton Conference: Continuing the Voyage of Discovery*, No. 2005-2522, Orlando, Florida, Jan. 2005.

[3] Peck, M. A., "Low-Power, High-Agility Space Robotics," *Proceedings of the AIAA Guidance, Navigation, and Control Conference*, No. 2005-6243, San Francisco, California, Aug. 2005.

[4] Carpenter, M. D. and Peck, M. A., "Dynamics of a High-Agility, Low-Power Imaging Payload," *IEEE Transactions on Robotics*, Vol. 24, No. 3, June 2008, pp. 666–675.

[5] Carpenter, M. D. and Peck, M. A., "Minimum-Power Robotic Maneuvering Using Control-Moment Gyroscopes," *Proceedings of the AIAA Guidance, Navigation, and Control Conference*, No. 2007-6324, Hilton Head, South Carolina, Aug. 2007.

[6] Carpenter, M. D. and Peck, M. A., "Reducing Base Reactions with Gyroscopic Actuation of Robotic Systems," *IEEE Transactions on Robotics*, Submitted.

[7] Carpenter, M. D., "Power-Optimal Steering of a Space Robotic System Driven by Control-Moment Gyroscopes," *Proceedings of the AIAA Guidance, Navigation, and Control Conference*, No. 2008-7270, Honolulu, Hawaii, Aug. 2008.

[8] Carpenter, M. D. and Peck, M. A., "Power-Optimal Steering of a Space-Robotic System Driven by Control-Moment Gyroscopes," *IEEE Transactions on Robotics*, Submitted.

[9] Laskin, R. A. and Sirlin, S. W., "Future Payload Isolation and Pointing System Technology," *Journal of Guidance, Control, and Dynamics*, Vol. 9, No. 4, 1986, pp. 469–477.

[10] Dubowsky, S. and Papadopoulos, E., "The Kinematics, Dynamics, and Con-

trol of Free-Flying and Free-Floating Space Robotic Systems," *IEEE Transactions on Robotics and Automation*, Vol. 9, No. 5, Oct. 1993, pp. 531–543.

[11] Wu, Y. and Gosselin, C. M., "Synthesis of Reactionless Spatial 3-DOF and 6-DOF Mechanisms Without Separate Counter-Rotations," *The International Journal of Robotics Research*, Vol. 23, No. 6, June 2004, pp. 625–642.

[12] Wu, Y. and Gosselin, C. M., "Design of Reactionless 3-DOF and 6-DOF Parallel Manipulators Using Parallelepiped Mechanisms," *IEEE Transactions on Robotics*, Vol. 21, No. 5, Oct. 2005, pp. 821–833.

[13] Longman, R. W., Lindberg, R. E., and Zedd, M. F., "Satellite-Mounted Robot Manipulators - New Kinematics and Reaction Moment Compensation," *International Journal of Robotics Research*, Vol. 6, No. 3, 1987, pp. 87–103.

[14] Oda, M. and Ohkami, Y., "Coordinated Control of Spacecraft Attitude and Space Manipulators," *Control Engineering Practice*, Vol. 5, No. 1, Jan. 1997, pp. 11–21.

[15] Quinn, R. D., Chen, J. L., and Lawrence, C., "Base Reaction Control for Space-Based Robots Operating in Microgravity Environment," *Journal of Guidance, Control, and Dynamics*, Vol. 17, No. 2, March 1994, pp. 263–270.

[16] Bialke, B. and Stromswold, E., "Reaction Wheel Actuator With Two Newton-Meter Torque Capability For Increased Spacecraft Agility," *Proceedings of the 6th International ESA Conference on Guidance, Navigation and Control Systems*, Loutraki, Greece, Oct. 2005.

[17] Honeywell Aerospace, "Pointing and Momentum Control," http://www.honeywell.com/sites/aero/Pointing-Momentum-Control.htm, Accessed Nov. 6, 2008.

[18] Pathak, P. M., Mukherjee, A., and Dasgupta, A., "Attitude Control of a Free-Flying Space Robot Using a Novel Torque Generation Device," *Simulation*, Vol. 82, No. 10, Oct. 2006, pp. 661–677.

[19] Osuka, K., Yoshida, K., and Ono, T., "New Design Concept of Space Manipulator: A Proposal of Torque-Unit Manipulator," *Proceedings of the 33rd IEEE Conference on Decision and Control*, Lake Buena Vista, Florida, Dec. 1994, pp. 1823–1825.

[20] Osuka, K., Yoshida, K., and Ono, T., "Adaptive Control of Torque-Unit Ma-

nipulator," *Proceedings of the American Control Conference*, Albuquerque, New Mexico, June 1997, pp. 957–958.

[21] Yoshida, K., Osuka, K., Nakano, T., and Ono, T., "Experimental Research of a Torque-Unit Manipulator," *Proceedings of the 1997 IEEE/RSJ International Conference on Intelligent Robots and Systems*, Grenoble, France, Sept. 1997, pp. 76–83.

[22] Hall, C. D., "High Speed Flywheels for Integrated Energy Storage and Attitude Control," *Proceedings of the American Control Conference*, Albuquerque, New Mexico, June 1997, pp. 1894–1898.

[23] Roes, J. B., "An Electro-Mechanical Energy Storage System for Space Application," *Progress in Astronautics and Rocketry*, Vol. 3, 1961, pp. 613–622.

[24] Adams, L. R., "Application of Isotensoid Flywheels to Spacecraft Energy and Angular Momentum Storage," NASA CR-1971, Feb. 1972.

[25] Notti, J. E., Cormack, A., and Schmill, W. C., "Integrated Power/Attitude Control System (IPACS) Study: Volume I - Feasibility Studies," NASA CR-2383, April 1974.

[26] Notti, J. E., Cormack, A., Schmill, W. C., and Klein, W. J., "Integrated Power/Attitude Control System (IPACS) Study: Volume II - Conceptual Designs," NASA CR-2384, April 1974.

[27] Notti, J. E., Cormack, A., and Klein, W. J., "Integrated Power/Attitude Control System (IPACS)," *Journal of Spacecraft and Rockets*, Vol. 12, No. 8, Aug. 1975, pp. 485–491.

[28] Hughes, P. C., *Spacecraft Attitude Dynamics*, Dover Publications, Inc., Mineola, New York, 1986.

[29] Tsiotras, P., Shen, H., and Hall, C., "Satellite Attitude Control and Power Tracking with Energy/Momentum Wheels," *Journal of Guidance, Control, and Dynamics*, Vol. 24, No. 1, Jan. 2001, pp. 23–34.

[30] Richie, D. J., Tsiotras, P., and Fausz, J. L., "Simultaneous Attitude Control and Energy Storage using VSCMGs: Theory and Simulation," *Proceedings of the American Control Conference*, Arlington, Virginia, June 2001, pp. 3973–3979.

[31] Richie, D. J., Lappas, V. J., and Palmer, P. L., "Sizing/Optimization of a Small Satellite Energy Storage and Attitude Control System," *Journal of Spacecraft and Rockets*, Vol. 44, No. 4, July 2007, pp. 940–952.

[32] Richie, D. J., Lappas, V. J., and Wie, B., "A Practical Variable-Speed Control Moment Gyroscope Steering Law for Small Satellite Energy Storage and Attitude Control," *Proceedings of the AIAA/AAS Astrodynamics Specialist Conference*, No. 2008-7501, Honolulu, Hawaii, Aug. 2008.

[33] Richie, D. J., Lappas, V. J., and Prassinos, G., "A Practical Small Satellite Variable-Speed Control Moment Gyroscope for Combined Energy Storage and Attitude Control," *Proceedings of the AIAA/AAS Astrodynamics Specialist Conference*, No. 2008-7503, Honolulu, Hawaii, Aug. 2008.

[34] Zhang, Y., Postrekhin, Y., Ma, K. B., and Chu, W.-K., "Reaction wheel with HTS bearings for mini-satellite attitude control," *Superconductor Science and Technology*, Vol. 15, April 2002, pp. 823–825.

[35] Ma, K. B., Zhang, Y., Postrekhin, Y., and Chu, W.-K., "HTS Bearings for Space Applications: Reaction Wheel With Low Power Consumption for Mini-Satellites," *IEEE Transactions on Applied Superconductivity*, Vol. 13, No. 2, June 2003, pp. 2275–2278.

[36] Lappas, V., Steyn, W. H., and Underwood, C., "Design and Testing of a Control Moment Gyroscope Cluster for Small Satellites," *Journal of Spacecraft and Rockets*, Vol. 42, No. 4, July 2005, pp. 729–739.

[37] Omagari, K., Usuda, T., and Matunaga, S., "Research of Control Momentum Gyros for Micro-Satellites and 3-DOF Attitude Dynamics Simulator Experiments," *Proceedings of the 8th International Symposium on Artificial Intelligence, Robotics, and Automation in Space*, Munich, Germany, Sept. 2005.

[38] Defendini, A., Faucheux, P., Guay, P., Bangert, K., Heimel, H., Privat, M., and Seiler, R., "Control Moment Gyro CMG 15-45 S: A compact CMG product for agile satellites in the one ton class," *Proceedings of the 10th European Space Mechanisms and Tribology Symposium*, Noordwijk, Netherlands, Sept. 2003, pp. 27–31.

[39] Bayard, D. S., "An Optimization Approach to Orienting Three Spacecraft Reaction Wheel Actuators with Application to the Europa Orbiter," JPL D-19562, Jet Propulsion Laboratory, Internal Document, Sept. 2000.

[40] Bayard, D. S., "An Optimization Result With Application to Optimal Spacecraft Reaction Wheel Orientation Design," *Proceedings of the American Control Conference*, Arlington, Virginia, June 2001, pp. 1473–1478.

[41] Skaar, S. B. and Kraige, L. G., "Single-Axis Spacecraft Maneuvers Using an Optimal Reaction Wheel Power Criterion," *Journal of Guidance, Control, and Dynamics*, Vol. 5, No. 5, Sept. 1982, pp. 543–544.

[42] Skaar, S. B. and Kraige, L. G., "Large-Angle Spacecraft Attitude Maneuvers Using an Optimal Reaction Wheel Power Criterion," *The Journal of the Astronautical Sciences*, Vol. 32, No. 1, Jan. 1984, pp. 47–61.

[43] Vadali, S. R. and Junkins, J. L., "Spacecraft Large Angle Rotational Maneuvers with Optimal Momentum Transfer," *The Journal of the Astronautical Sciences*, Vol. 31, No. 2, April 1983, pp. 217–235.

[44] Yang, C.-C. and Wu, C.-J., "Optimal large-angle attitude control of rigid spacecraft by momentum transfer," *IET Control Theory and Applications*, Vol. 1, No. 3, May 2007, pp. 657–664.

[45] Schaub, H., "Locally Power-Optimal Spacecraft Attitude Control for Redundant Reaction Wheel Cluster," *Proceedings of the AIAA Guidance, Navigation, and Control Conference*, No. 2008-6259, Honolulu, Hawaii, Aug. 2008.

[46] Kurokawa, H., "Survey of Theory and Steering Laws of Single-Gimbal Control Moment Gyros," *Journal of Guidance, Control, and Dynamics*, Vol. 30, No. 5, Sept. 2007, pp. 1331–1340.

[47] Nakamura, Y. and Hanafusa, H., "Inverse Kinematic Solutions with Singularity Robustness for Robot Manipulator Control," *Journal of Dynamic Systems, Measurement, and Control*, Vol. 108, Sept. 1986, pp. 163–171.

[48] Oh, H. S. and Vadali, S. R., "Feedback Control and Steering Laws for Spacecraft Using Single Gimbal Control Moment Gyros," *The Journal of the Astronautical Sciences*, Vol. 39, No. 2, April 1991, pp. 183–203.

[49] Kalman, R. E. and Bertram, J. E., "Control System Analysis and Design by the Second Method of Lyapunov," *Journal of Basic Engineering*, Vol. 82, No. 2, June 1960, pp. 371–400.

[50] Ford, K. A. and Hall, C. D., "Singularity Direction Avoidance Steering

for Control-Moment Gyros," *Journal of Guidance, Control, and Dynamics*, Vol. 23, No. 4, July 2000, pp. 648–656.

[51] Cornick, D. E., "Singularity Avoidance Control Laws for Single Gimbal Control Moment Gyros," *Proceedings of the AIAA Guidance and Control Conference*, No. 79-1698, Boulder, Colorado, Aug. 1979, pp. 20–33.

[52] Bedrossian, N. S., Paradiso, J., Bergmann, E. V., and Rowell, D., "Steering Law Design for Redundant Single-Gimbal Control Moment Gyroscopes," *Journal of Guidance, Control, and Dynamics*, Vol. 13, No. 6, 1990, pp. 1083–1089.

[53] Vadali, S. R., Oh, H. S., and Walker, S. R., "Preferred Gimbal Angles for Single Gimbal Control Moment Gyros," *Journal of Guidance, Control, and Dynamics*, Vol. 13, No. 6, 1990, pp. 1090–1095.

[54] Paradiso, J. A., "Global Steering of Single Gimballed Control Moment Gyroscopes Using a Directed Search," *Journal of Guidance, Control, and Dynamics*, Vol. 15, No. 5, Sept. 1992, pp. 1236–1244.

[55] Schaub, H. and Junkins, J. L., "Singularity Avoidance Using Null Motion and Variable-Speed Control Moment Gyros," *Journal of Guidance, Control, and Dynamics*, Vol. 23, No. 1, Jan. 2000, pp. 11–16.

[56] Wie, B., Bailey, D., and Heiberg, C., "Singularity Robust Steering Logic for Redundant Single-Gimbal Control Moment Gyros," *Journal of Guidance, Control, and Dynamics*, Vol. 24, No. 5, Sept. 2001, pp. 865–872.

[57] Wie, B., "New Singularity Escape/Avoidance Steering Logic for Control Moment Gyro Systems," *Proceedings of the AIAA Guidance, Navigation, and Control Conference*, No. 2003-5659, Austin, Texas, Aug. 2003.

[58] Wie, B., "Singularity escape/avoidance steering logic for control moment gyro systems," U. S. Patent 6917862, July 12, 2005.

[59] Peck, M. A., Hamilton, B. J., and Underhill, B., "Method and system for optimizing torque in a CMG array," U. S. Patent 7014150, March 21, 2006.

[60] Wie, B., "Singularity Escape/Avoidance Steering Logic for Control Moment Gyro Systems," *Journal of Guidance, Control, and Dynamics*, Vol. 28, No. 5, Sept. 2005, pp. 948–956.

[61] Jung, D. and Tsiotras, P., "An Experimental Comparison of CMG Steering Control Laws," *Proceedings of the AIAA/AAS Astrodynamics Specialist Conference*, No. 2004-5294, Providence, Rhode Island, Aug. 2004.

[62] Lee, S. M. and Rhee, S.-W., "Experiments of Singularity Avoidance Steering Control Laws for Redundant Single-Gimbal Control Moment Gyros," *Proceedings of the International Conference on Control, Automation, and Systems*, Seoul, Korea, Oct. 2007, pp. 175–178.

[63] Cook, L., Golley, P., Krome, H., Blondin, J., Gurrisi, C., and Kolvek, J., "Design, Fabrication, and Test of a 4750 Newton-Meter-Second Double Gimbal Control Moment Gyroscope," *Proceedings of the 23rd Aerospace Mechanisms Symposium*, Huntsville, Alabama, May 1989, pp. 59–76.

[64] Schaub, H., Vadali, S. R., and Junkins, J. L., "Feedback Control Law for Variable Speed Control Moment Gyros," *The Journal of the Astronautical Sciences*, Vol. 46, No. 3, July 1998, pp. 307–328.

[65] Schaub, H. and Junkins, J. L., *Analytical Mechanics of Space Systems*, American Institute of Aeronautics and Astronautics, Inc., Reston, Virginia, 2003.

[66] Margulies, G. and Aubrun, J. N., "Geometric Theory of Single-Gimbal Control Moment Gyro Systems," *The Journal of the Astronautical Sciences*, Vol. 26, No. 2, April 1978, pp. 159–191.

[67] Kurokawa, H., "A Geometric Study of Single Gimbal Control Moment Gyros: Singularity Problems and Steering Law," Ph.D. Dissertation, Aeronautics and Astronautics, University of Tokyo, Japan, 1997, http://staff.aist.go.jp/kurokawa-h/CMGpaper97.pdf.

[68] Havill, J. R. and Ratcliff, J. W., "A Twin-Gyro Attitude Control System for Space Vehicles," NASA TN D-2419, Aug. 1964.

[69] Crenshaw, J. W., "2-SPEED, A Single-Gimbal Control Moment Gyro Attitude Control System," *Proceedings of the AIAA Guidance and Control Conference*, No. 73-895, Key Biscayne, Florida, Aug. 1973.

[70] Liska, D. J., "A Two-Degree-of-Freedom Control Moment Gyro for High Accuracy Attitude Control," *Journal of Spacecraft and Rockets*, Vol. 5, No. 1, Jan. 1968, pp. 74–83.

[71] Aubrun, J. N. and Margulies, G., "Gyrodampers for Large Space Structures," NASA CR-159171, Feb. 1979.

[72] Cunningham, D. C. and Driskill, G. W., "A Torque Balance Control Moment Gyroscope Assembly for Astronaut Maneuvering," *Proceedings of the 6th Aerospace Mechanisms Symposium*, Moffett Field, California, Sept. 1971.

[73] Haeussermann, W., "Comparison of Some Actuation Methods for Attitude Control of Space Vehicles," Army Ballistic Missile Agency, ABMA-DG-TN-63-59, Nov. 1959.

[74] Riper, R. V. and Liden, S. P., "A New Fail Operational Control Moment Gyro Configuration," *Proceedings of the AIAA Guidance, Control, and Flight Mechanics Conference*, No. 71-936, Aug. 1971.

[75] Brown, D. and Peck, M. A., "Scissored-Pair Control Moment Gyros: A Mechanical Constraint Saves Power," *Journal of Guidance, Control, and Dynamics*, Vol. 31, No. 6, Nov. 2008, pp. 1823–1826.

[76] Davis, P., "Momentum System Concepts and Trades for the New Class of Smaller Lower Cost Satellites," *Proceedings of the 29th Annual AAS Guidance and Control Conference*, No. 06-023, Breckenridge, Colorado, Feb. 2006.

[77] Hamilton, B. and Underhill, B., "Modern Momentum Systems for Spacecraft Attitude Control," *Proceedings of the 29th Annual AAS Guidance and Control Conference*, No. 06-028, Breckenridge, Colorado, Feb. 2006.

[78] Lappas, V. J., Steyn, W. H., and Underwood, C. I., "Torque Amplification of Control Moment Gyros," *Electronics Letters*, Vol. 38, No. 15, 2002, pp. 837–839.

[79] Wie, B., Bailey, D., and Heiberg, C., "Singularity Robust Steering Logic for Redundant Single-Gimbal Control Moment Gyros," *Proceedings of the AIAA Guidance, Navigation, and Control Conference*, No. 2000-4453, Denver, Colorado, Aug. 2000.

[80] Vadali, S. R. and Krishnan, S., "Suboptimal Command Generation for Control Moment Gyroscopes and Feedback Control of Spacecraft," *Journal of Guidance, Control, and Dynamics*, Vol. 18, No. 6, 1995, pp. 1350–1354.

[81] Elgersma, M. R., Johnson, D. P., Peck, M. A., Underhill, B. K., Stein, G., Morton, B. G., and Hamilton, B. J., "Method and system for controlling sets of

collinear control moment gyroscopes," U. S. Patent Application 20070124032, Nov. 30, 2005.

[82] Kane, T. R. and Levinson, D. A., "The Use of Kane's Dynamical Equations in Robotics," *The International Journal of Robotics Research*, Vol. 2, No. 3, 1983, pp. 3–21.

[83] Kane, T. R. and Levinson, D. A., *Dynamics: Theory and Applications*, McGraw-Hill, Inc., New York, 1985.

[84] Hollerbach, J. M., "A Recursive Lagrangian Formulation of Manipulator Dynamics and a Comparative Study of Dynamics Formulation Complexity," *IEEE Transactions on Systems, Man, and Cybernetics*, Vol. SMC-10, No. 11, Nov. 1980, pp. 730–736.

[85] Luh, J. Y. S., Walker, M. W., and Paul, R. P. C., "On-Line Computational Scheme for Mechanical Manipulators," *Journal of Dynamic Systems, Measurement, and Control*, Vol. 102, No. 2, June 1980, pp. 69–76.

[86] Moon, F. C., *Applied Dynamics: With Applications to Multibody and Mechatronic Systems*, John Wiley and Sons, Inc., New York, 1998.

[87] Roithmayr, C. M., Karlgaard, C. D., Kumar, R. R., and Bose, D. M., "Integrated Power and Attitude Control with Spacecraft Flywheels and Control Moment Gyroscopes," *Journal of Guidance, Control, and Dynamics*, Vol. 27, No. 5, Sept. 2004, pp. 859–873.

[88] Peck, M. A., Brown, D., and Carpenter, M. D., "Representation of Cyclic Coordinates and Rotor Energy in Dynamic Models of Control-Moment Gyroscopes," In preparation.

[89] Harrell, J. P., "Control motion gyro with vibration isolation," U. S. Patent 5820078, Oct. 13, 1998.

[90] Wie, B., Bailey, D., and Heiberg, C., "Rapid Multitarget Acquisition and Pointing Control of Agile Spacecraft," *Journal of Guidance, Control, and Dynamics*, Vol. 25, No. 1, Jan. 2002, pp. 96–104.

[91] Nakanishi, T., Ando, Y., Sakakibara, K., and Mitsukane, A., "Control moment gyro having spherical rotor with permanent magnets," U. S. Patent 5476018, Dec. 19, 1995.

[92] Mooney, C. Z., "Monte Carlo Simulation," Sage University Papers Series, No. 07-116, Sage Publications, Thousand Oaks, California, 1997.

[93] Koser, K., "Closed Kinematic Chain Robot Arm," International Patent WO/2000/010776, The World Intellectual Property Organization, Feb. 3, 2000.

[94] Goldstein, H., Poole, C., and Safko, J., *Classical Mechanics*, Addison Wesley, San Francisco, California, 3rd ed., 2002.

[95] Brown, D., "Control-Moment Gyros as Space-Robotics Actuators," *Proceedings of the AIAA Guidance, Navigation, and Control Conference*, No. 2008-7271, Honolulu, Hawaii, Aug. 2008.

[96] Oh, H. S., Vadali, S. R., and Junkins, J. L., "Use of the Work-Energy Rate Principle for Designing Feedback Control Laws," *Journal of Guidance, Control, and Dynamics*, Vol. 15, No. 1, Jan. 1992, pp. 275–277.

[97] Stocke, M., "Cornell University Microgravity Research Team," http://mae.cornell.edu/cmg/nasa.html, May 2007.

[98] Jarc, A. M., Kimes, A. B., Pearson, M. E., and Peck, M. A., "The Design and Control of a Low-Power, Upper Limb Prosthesis," *Proceedings of the IEEE 32nd Annual Northeast Bioengineering Conference*, April 2006, pp. 165–166.

[99] Livingston, I., Brown, D., and Peck, M., "A Method of Robotic Actuation Using Control Moment Gyros," *Presented at the AIAA Region I Young Professional, Student, and Education Conference 2008*, Laurel, Maryland, Nov. 2008.